SELECTED-ION VELOCITY MAP IMAGING OF GAS PHASE CLUSTERS AND COMPLEXES

by

BRANDON MICHAEL RITTGERS

(Under the Direction of Michael A. Duncan)

ABSTRACT

Velocity map imaging is a vital tool in the study of the photodissociation dynamics of cold gas phase molecules. Imaging studies have been carried out over a wide variety of neutral systems, however its application to the study of ions has been limited to cases where photoionization is efficient. A recently constructed velocity map imaging apparatus has been used to study the photodissociation of mass-selected ions in which efficient cluster sources are implemented. This instrument offers new insights into the photodissociation dynamics of ions, as well as their binding energies, which are difficult to obtain experimentally and very few have been well defined. Upper limits on the dissociation energies for a variety of Ag^{+}–π complexes and $Zn^{+}(CH_3OH)$ have been determined along with their angular distributions. The use of velocity map imaging in the qualitative study of the photodissociation dynamics of carbon cluster cations has also been demonstrated.

INDEX WORDS: Velocity Map Imaging, Photofragment Imaging, Photodissociation, Ions, Transition Metal Ion Complexes, Carbon Cluster Cations

SELECTED-ION VELOCITY MAP IMAGING OF GAS PHASE CLUSTERS AND COMPLEXES

by

BRANDON MICHAEL RITTGERS

B.S., University of West Georgia, 2015

A Dissertation Submitted to the Graduate Faculty of The University of Georgia in Partial Fulfillment of the Requirements for the Degree

DOCTOR OF PHILOSOPHY

ATHENS, GEORGIA

2022

SELECTED-ION VELOCITY MAP IMAGING OF GAS PHASE CLUSTERS AND COMPLEXES

by

BRANDON MICHAEL RITTGERS

Major Professor:	Michael A. Duncan
Committee:	Gary E. Douberly
	Melanie A. R. Reber

Electronic Version Approved:

Ron Walcott
Vice Provost for Graduate Education and Dean of the Graduate School
The University of Georgia
May 2022

DEDICATION

To Gregory Dean Rittgers, Gregory Dean Rittgers, Jr., and Ryne Stephen Rittgers.

Without you, I wouldn't be where I am today. I hope I've made you proud.

ACKNOWLEDGEMENTS

First and foremost, I would like to thank God for giving me the strength to endure when I thought I no longer had it in me and allowing me uncover some of His tiniest little mysteries.

I must also thank Mike Duncan for giving me the opportunity to work in his lab. Thank you for trusting me with hundreds of thousands of dollars of equipment and for your patience every time I had to fix it. Your knowledge and passion for chemistry are unmistakable, and your analogies are unmatched. I hope that one day I can explain such difficult and complex topics as succinctly as you. Thank you for your understanding during difficult times and for pushing me when I needed it. I am proud to graduate from your lab.

To my mother, Kathy, thank you for all you have done for me in my 30 trips around the sun. I know we had some difficult years, and I will forever be sorry for them. I know it was hard, but thank you for letting me make the decision to take a different path than you had planned for me. For without that, I doubt I would be where I am today. Thank you is not enough for the love and support you and dad gave me. You are undoubtedly THE strongest person I know. Your light shines brighter than the sun, even after everything. I love you and hope I can be just half as good of a person as you are.

To my sister, Jenny, thank you for being a second mother. I may talk like I didn't like it, but I would not be getting my PhD if you had been the "cool" older sister I wish you were when I was younger… and I cannot thank you enough for that. I am grateful for the relationship we have today. Thank you for all of your love and support over the years and for the army of people

you had praying for me. Tell Joy she gets a shoutout too! Because Lord knows she's supported us both. As you used to tell dad way back when, Go Dawgs!

To all of the friends I made at UGA, thank you for all of the great memories made in my time here. First, I must thank Nick and Joe for their friendship. You both have been great friends, and I couldn't imagine being a throuple with anyone else. Nick, thank you for letting me crash at you and Sydney's place for so long. And Joe, I'm sorry I won't be coming to bug you in Oregon. To Mike, thanks for letting me take you camping and sorry for almost killing us both on our first trip, but I had fun regardless. Paulie and Lauren, thanks for listening to my rants when lasers and the instrument broke and for making sure I made it home on more than one occasion.

In the Duncan lab, thanks to Tim, Josh, and Melissa for always shooting the bull during a warm-up or cool-down when I was trying to kill some time, and for letting me bounce ideas off you and telling me when they weren't up to snuff. I never did find that YAG grease. I also have to thank DJ for being a great undergraduate, you did pretty well, but mostly for getting me back into golf. And thanks to all the Duncan lab members past and present that I have not already mentioned: JP, Daniel, David, Natalie, Ian, Jason, Dylan, Nathan, Anna, Connor, and Jack.

Last, but most certainly not least, I have to thank my wife, Whitney. You're the love of my life; I could not have done this without you. You picked me up and told me to keep going when I didn't think I could any longer. Thank you for putting up with all of my nerdiness. And thank you for giving me Ryne. I cannot wait to be home for good and spending the rest of my life with you and raising all of the little ones we might be blessed with. I love you, forever and always!

TABLE OF CONTENTS

Page

CHAPTER 1

INTRODUCTION

Experiments on the photodissociation dynamic of cold gas phase molecules shed light on the very fundamental nature of chemical bond breaking and bond formation. Within a collisionless environment, laser photodissociation studies can provide knowledge on energy and angular momentum partitioning, as well as electronic relaxation and rearrangement without the added complexities of thermal distribution or bimolecular interferences.[1,2] To understand the laser induced-photodissociation processes, or so-called "half-collisions," requires the ability to measure the internal energy, velocity, and angular distribution of all of the products.[3-7] To this end, a variety of techniques have been developed. Early examples of experiments that can observe these properties are time-of-flight measurements and translational energy spectroscopies.[8,9] However, the ability for angle-resolved detection is required in time-of-flight experiments in order to recover the full angular distribution of products, while an electrostatic analyzer is typically used in translational energy spectroscopies which must be scanned over a range of kinetic energies to build up the full distribution.[10-28] The Doppler effect may also be taken advantage of to obtain velocity and angular distributions of light photofragments.[29-31] Laser induced fluorescence can be used to measure the Doppler shifted frequency profiles of translationally excited fragments. This technique also requires the ability to record at multiple detection angles in order to build up a full velocity distribution. The development of photofragment imaging overcame the shortcoming of these other techniques by being able to simultaneously measure both the product velocity and the angular distribution.[32] Photofragment

imaging techniques are now standard methods for studying the photodissociation and collisions of gas phase molecules.[1,2,33-37] Measurement of the velocity and angular distributions of fragments helps determine the nature of the electronic transitions involved in photodissociation and how energy is partitioned into the products during decomposition of the parent molecule, i.e. translational (kinetic), rotational, and vibrational energy. Thus, photofragment imaging techniques are a powerful tool in the study of photodissociation dynamics, and a continued effort has been devoted to its development. In this work, a new velocity map imaging (VMI) spectrometer is described and used for photodissociation studies on silver cation-π complexes, $Zn^+(CH_3OH)$, and C_n^+ clusters.

The first ion imaging experiment, performed by Chandler and Houston, used a simple two-electrode set up to study the photodissociation of CH_3I.[32] In it, the fourth harmonic of a Nd:YAG laser (266 nm) was used to dissociate jet-cooled CH_3I in front of the repeller electrode, while a second tunable laser was used to ionize the CH_3 fragments via 2+1 resonance-enhanced multiphoton ionization (REMPI). The ions were then accelerated toward a position-sensitive reticon array detector. In this experiment, they saw that >95% of CH_3 ($v = 0$) fragments were formed in coincidence with $I(^2P_{1/2})$, but most importantly, that it was possible to record both the angular and velocity distribution of the selected photofragment at the same time. The two-electrode design was later improved upon by Eppink and Parker[38] by adding a third, extraction, electrode which resembled a Wiley-McLaren configuration[39] and replacing gridded electrodes with open electrostatic lenses.[38-39] The power of this new method was demonstrated with the photodissociation of O_2, where both of the O_2 atoms and their corresponding photoelectrons were imaged. Their modifications increased ion transmission, eliminated grid aberrations, improved the focusing power with the tunable voltage of the extraction electrode and achieved "velocity

mapping" where all ions with the same initial velocity vector are mapped onto the same point on the detector. VMI resolution has also been improved with the use of centroiding methods that employ a computer program to reduce the spot size of each ion impact event at the detector to a single pixel in the recorded image.

The ion imaging experiment of Chandler and Houston[32] and the VMI method of Eppink and Parker[38] only record the two-dimensional projection of a three-dimensional distribution of ions or electrons. The three-dimensional distribution must be recovered by a mathematical reconstruction from the two-dimensional image.[35,40-41] Inversion methods and forward convolution methods are two general approaches used for image reconstruction. Inversion methods, such as the inverse Abel transform, can be used when the three-dimensional velocity distribution has an axis of cylindrical symmetry about an axis that is parallel to the face of the detector, which includes most photodissociation and bimolecular scattering experiments. All of the necessary information for the reconstruction is contained within the two-dimensional projection. Forward convolution methods are used when experiments do not have an axis of cylindrical symmetry. Here, the two-dimensional image is simulated while iteratively optimizing the parameters of the simulation to achieve the most accurate reproduction of the experimental data. This includes angular momentum polarization studies where the electric vector of the photolysis and photoionization lasers are perpendicular to one another. However, these mathematical reconstruction techniques introduce unwanted artificial noise in the resulting reconstructed image.

The need for mathematical reconstruction was reduced with the introduction of sliced imaging techniques. These techniques were designed so that only the central "slice" of the expanding photofragment ion cloud would be imaged. This central portion of the Newton's

sphere contains all of the angular and kinetic energy information, and thus eliminates the need to reconstruct the fragment angular and velocity distribution from the two-dimensional projection. There are two methods generally employed for sliced imaging techniques: laser slicing techniques and time slicing techniques. In laser slicing, the ionizing laser is manipulated in some way so that slices of the photofragment distribution are ionized and detected. Kinugawa and Arikawa demonstrated laser slicing by combining Doppler spectroscopy with ion imaging by aligning a laser parallel to the time-of-flight axis and tuning it to the center of the photofragment Doppler profile.[42] In this setup, only photofragments with a zero-velocity component parallel to the direction of the beam, or fragments with velocities perpendicular to the laser, were selectively ionized and detected. These fragments constitute the central slice of the photofragment distribution. Tonokura and Suzuki used a different approach to laser slicing in which they used a cylindrical lens to focus an ionizing laser to a sheet like profile that ionized only a thin slice of the photofragment distribution.[43] One disadvantage of laser slicing techniques is that the flux of the laser beam is not uniform, so fragments in different regions of the expanding sphere will not be detected with uniform efficiency. For time slicing techniques, a pulsed detection method is required. Kitsopoulos and coworkers took a different approach to laser slicing where a temporal delay between the dissociation/ionization laser pulses and a pulsed extraction field was introduced.[44] After photodissociation, the ions were allowed to drift in a field free region in front of a grounded repeller electrode, which is then switched to high voltage. This allowed for tuning the temporal spread of ions at the detector, which is somewhat analogous to Wiley and McLaren's pulse delay extraction technique in time-of-flight mass spectrometry.[42] This technique was first used to increase spatial resolution in time-of-flight mass spectrometers, but it may also be used to spoil resolution at the detector. The result is a broad arrival time

distribution of ions at the detector on the order of 100s of nanoseconds. A pulsed MCP can then be turned on (< 90 ns) to produce an image of only the central slice of the expanding photofragments. A disadvantage of the pulse delay extraction method is that it requires fine mesh grids to create the field free region. These grids can introduce aberrations in the image and reduce resolution and ion transmission. The Suits group introduced DC-slice imaging which replaced the grids and pulsed fields with electrostatic lenses and static voltages.[45] The addition of extra lenses with the typical three electrodes of VMI experiments allows for the field between adjacent electrodes to be reduced, which stretches the ion cloud along the time-of-flight axis similar to that seen by Kitsopoulos.

These techniques are not limited to the study of simple photodissociation processes and have been used to study a variety of other dynamic processes. For example, Suits and coworkers studied the vector correlations of the fragments in the photodissociation of O_3 at 248 nm.[46] In this two laser experiment, a KrF excimer laser (248 nm) was used to dissociate O_3 while a second doubled dye laser (303 – 315 nm) ionizes the O_2 photofragment which is accelerated toward an imaging detector under VMI conditions. The polarization of the ionization laser was then rotated relative to the polarization of the dissociation laser to observe the correlation between the velocity vector and the angular momentum vector of the fragments. This is because the efficiency of detecting the photofragments is dependent upon the alignment of the electric vector of the ionizing laser with the angular momentum vector of the photofragment. Dissociation of ozone at 248 nm leads to the $^1B_2 \leftarrow ^1A_2$ transition with prompt dissociation along the $O–O_2$ producing O_2 with little change to the equilibrium geometry prior to dissociation. There is little change in the equilibrium geometry prior to dissociation. They observed O_2 fragments recoil with large amounts of rotational excitation with the total angular momentum vector, *J*,

perpendicular to the velocity vector, *v*. This confirmed an impulsive model for dissociation of ozone, which may be expected for nonlinear molecules where prompt dissociation produces a torque on one or both fragments, but more importantly that ion-imaging could be used to quantify angular momentum polarization. However, using lasers with perpendicular polarizations violates the cylindrical symmetry condition for inverse Abel transformations, which is one reason for the inception of DC-slice imaging that skirts the need for image reconstruction.

Imaging has also been taken advantage of in the study of scattering in crossed molecular beams. Houston and coworkers were able to obtain differential cross sections with both product state resolution and simultaneous detection of all scattering angles in crossed molecular beams of NO and Ar.[47] Cline and coworkers were able to determine the sense of rotation (clockwise or counterclockwise) in the same collision system with the use of a circularly polarized ionization laser to detect scattered NO.[48] Imaging may also be used to look at reactive scattering, which helps to improve our fundamental understanding of chemical reactivity. Chandler and coworkers looked at the prototypical scattering reaction $H + D_2$ in a crossed molecular beam experiment.[49] Work from the Wester group and the Farrar group have demonstrated the power of imaging in ion-molecule reactions as well.[50-52] A big advantage of imaging in crossed beam experiments is that it does not require a rotatable mass spectrometer to observe different scattering angles and greatly reduces the time it takes to collect data.[49]

It is also possible to use VMI to image electrons, which has greatly enhanced the efficiency and sensitivity of photoelectron spectroscopy with the development of slow electron velocity map imaging (SEVI).[53-55] SEVI provides a method of measuring photoelectron spectra that combines the best of photoelectron spectroscopy (PES) and zero electron kinetic energy (ZEKE) spectroscopy. It is relatively simple, like PES, in that a spectrum may be obtained using

only a few detachment wavelengths while still maintaining a higher energy resolution similar to ZEKE.[54] In SEVI, anions are produced either by electron attachment with electron impact or laser vaporization. Electrons are then detached at fixed frequencies and extracted at low voltages resulting in high resolution spectra that represent the electronic and vibrational levels of the neutral molecule. Neumark and coworkers have used this technique to look at the photodetachment spectra of CCO^- and CCS^- and determined precise electron affinities as well as energies of the $X\ ^3\Sigma^-$, $a\ ^1\Delta$, $b\ ^1\Sigma^+$, and $A\ ^3\Pi$ electronic states of the neutral species as well as the spin-orbit coupling splitting in the ground state.[56] They also observed several vibronic transitions that were previously unobserved and saw evidence for a small amount of vibronic coupling of electronic states in CCS. Mass-selected anion photoelectron imaging experiments have also been developed in the Johnson, Wang, and Jarrold groups, demonstrating the amount of interest in this method.[57-59] However, SEVI does not come without its own challenges. It is able to resolve low-frequency structures that represent anharmonic, large amplitude motions that are difficult to analyze. The resolution of the detection method is also sufficiently high enough that the observed spectral resolution is limited by the temperature of the ion beam, so it is important to design a source to cool the ions as low as possible.[54]

Imaging techniques have also been extended to coincidence spectroscopy with the development of photoelectron-photoion coincidence spectroscopy (PEPICO).[60] This technique typically employs a VUV source to ionize a neutral molecule, and the resulting electron is imaged and its arrival time marks the start of the flight time of the ion. Typically, the pulse of a photoionization laser marks the start of the flight time, but PEPICO allows for the use of a continuous wave laser.[61] Recently, Continetti and coworkers used this method to study the transition state dynamics of the $OH + CH_3OH \rightarrow H_2O + CH_3O$ reaction by photodetachment of

$CH_3O^-(H_2O)$.[62] Their results indicate that the products $H_2O + CH_3O + e^-$ are produced vibrationally excited along with a significant portion in the vibrational ground state and that the water bending mode promoted the dissociation of the long-lived neutral complex. They also indicate that vibrational Feshbach resonances could play a role in bimolecular reactions of methoxy radicals mediated by water adducts.

Much work has been done in the development and use of photofragment imaging, but most studies have focused on neutral systems, with the exception of the crossed molecular beam experiments on ion-molecule reactions. And while SEVI involves measurements on anionic systems, the purpose is to reveal the electronic structure and vibrational levels of neutrals. Imaging studies on the photodissociation of ions are far more limited and essentially restricted to systems in which photoionization is efficient enough to produce an adequate density of ions.[63-68] This is surprising, considering the diversity of imaging techniques that have been developed. An imaging experiment that incorporated an efficient ion source would be a more general approach to study the photodissociation dynamics of ionic systems, but this goal has only been pursued by just a few labs. Lepère and coworkers developed a mass-selected ion imaging apparatus with an electron impact ionization source for studying the photodissociation of ions that simultaneously detects both the neutral and ionic fragments.[69] There are no optics for focusing the ions though, instead the ionic fragments are bent out of the initial time-of-flight axis with an electrostatic analyzer towards the detector while the neutral fragments continue their path to another detector. However, the images of the ions and the neutrals are comparable because the ionic fragments are not accelerated like they are in typical imaging experiments, so the instrument is low resolution by design. The Misaizu group has developed two apparatuses for studying the photofragment imaging of ions with higher resolution than the one previously described, even though they are

not velocity map imaging.[70-73] Both instruments are fitted with laser vaporization sources for generating metal-containing ions. The first design is based on a reflectron time-of-flight mass spectrometer except typical reflectron grids are replaced with static open rings. Photodissociation takes place before the ions enter the reflectron, and the fragments are focused as they exit because the electric field is not confined by a grid. The second instrument incorporates a second reflectron for increased mass resolution. The face of their detectors is not grounded, so ions feel an electric field right before the detector. This has the effect of focusing the ion cloud at the detector which must be accounted for. The Mackenzie group has also constructed an instrument for VMI fitted with a laser vaporization source.[74-77] Although it is used for the study of small metal-containing neutral clusters, it demonstrates the coupling of a laser vaporization source with a VMI spectrometer. Our lab has designed and built a new VMI spectrometer that incorporates laser vaporization and pulsed electrical discharge sources for the study of the photodissociation dynamics of mass-selected ions. The Metz group has also recently demonstrated their new VMI instrument which is similar to ours and also incorporates laser vaporization and discharge sources.[78-84] These instruments expand the field of photofragment imaging to the study of ionic systems that cannot be generate using photoionization methods. The following chapter describe our new apparatus for selected ion velocity map imaging and its application to the photodissociation of Ag^+–π complexes, $Zn^+(CH_3OH)$, and carbon cluster cations.

References

1. Butler, L. J.; Neumark, D. M. Photodissociation Dynamics. *J. Phys. Chem.* **1996**, *100*, 12801-12816.
2. Suits; A. G. Invited Review Article: Photofragment Imaging. *Rev. Sci. Instrum.* **2018**, *89*, 111101.
3. Bowers, M. T. *Gas Phase Ion Chemistry*; Academic Press, Inc., Orlando, FL, USA 1984
4. Schinke, R. Photodissociation Dynamics; Cambridge University Press, Cambridge, UK 1993.
5. Ashfold, M. N. R.; Baggott, J. E. *Molecular Photodissociation Dynamics*; Royal Society of Chemistry, London, UK.
6. Baer, T.; Hase, W. L. *Unimolecular Reaction Dynamics*; Oxford University Press, New York, USA 1996.
7. Lee, Y. P. State-Resolved Dynamics of Photofragmentation. *Annu. Rev. Phys. Chem.* **2003**, *54*, 215-244.
8. Ervin, K. M. Experimental Techniques in Gas-Phase Ion Thermochemistry *Chem. Rev.* **2001**, *101*, 391-444.
9. Laskin, J.; Lifshitz, C. Kinetic Energy Release Distributions in Mass Spectrometry *J. Mass Spectrom.* **2001**, *36*, 459-478.
10. Lee, Y. T.; McDonald, J. D.; LeBreton, P. R.; Herschbach, D. R. Molecular Beam Reactive Scattering Apparatus with Electron Bombardment Detector. *Rev. Sci. Instrum.* **1969**, *40*, 1402-1408.
11. Busch, G. E.; Cornelius, J. F.; Mahoney, R. T.; Morse, R. I.; Schlosser, D. W.; Wilson, K. R. Photofragment Spectrometer. *Rev. Sci. Instrum.* **1970**, *41*, 1066-1073.

12. Busch, G. E.; Wilson, K. R. Triatomic Photofragment Spectra. I. Energy Partitioning in NO_2 Photodissociation. *J. Chem. Phys.* **1972**, *56*, 3626-3628.

13. Busch, G. E.; Wilson, K. R. Triatomic Photofragment Spectra. II. Angular Distribution from NO_2 Photodissociation. *J. Chem. Phys.* **1972**, *56*, 3628-3654.

14. Cooks, R. G.; Beynon, J. H.; Caprioli, R. M.; Lester, G. R. *Metastable Ions*; Elsevier, Amsterdam, NL 1973.

15. Huber, B. A.; Miller, T. M.; Cosby, P. C.; Zeman, H. O.; Leon, R. L.; Moseley, J. T.; Peterson, J. R. Laser–Ion Coaxial Beams Spectrometer. *Rev. Sci. Instrum.* **1977**, *48*, 1306-1313.

16. Lifshitz, C.; Tzidony, E. Kinetic Energy Release Distributions for $C_3H_6O^{+\bullet}$ Ion Dissociations: A Further Test of the Applicability of the Energy-Randomization Hypothesis to Unimolecular Fragmentations. *Int. J. Mass Spectrom. Ion Phys.* **1981**, *39*, 181-195.

17. Van Deen, G. N. A.; Mohamed, K. A.; Baller, T.; de Vries, A. E. Photofragmentation of HI in the First Continuum. *Chem. Phys.* **1983**, *80*, 113-120.

18. Illies, A. J.; Jarrold, M. F.; Wagner-Redeker, W.; Bowers, M. T. Photoinduced Intramolecular Charge Transfer: Photodissociation of $CO_2^+ \cdot$Ar Cluster Ions. *J. Am. Chem. Soc.* **1985**, *107*, 2842-2849.

19. Hall, G. E.; Sivakumar, N.; Ogorzalek, R.; Chawla, G.; Haerri, H.-P.; Houston, P. L.; Burak, I.; Hepburn, J. W. Product Correlations in Photofragment Dynamics. *Disc. Farad. Soc.* **1986**, *82*, 13-24.

20. Kim, H.-S.; Kuo, C.-H.; Bowers, M. T. Photon Driven Charge Transfer Half-Collisions: The Photodissociation of $CO_2 \cdot O_2^+$ Cluster Ions with Resolution of the O_2 Product Vibrational States. *J. Chem. Phys.* **1987**, *87*, 2667-2676.

21. Lee, Y. T. Molecular beam studies of elementary chemical processes. *Science* **1987**, *236*, 793-798.

22. Ogorzalek, R.; Hall, G. E.; Härri, H.-P.; Houston, P. L. State-Resolved Photofragment Velocity Distributions by Pulsed Extraction Time-of-Flight Mass Spectrometry," *J. Phys. Chem.* **1988**, *92*, 5-8.

23. Snodgrass, J. T.; Dunbar, R. C.; Bowers, M. T. Photodissociation of the Benzene Dimer Cation in the Gas Phase. *J. Phys. Chem.* **1990**, *94*, 3648-3651.

24. Graul, S. T.; Kim, H.-S.; Bowers, M. T. The Dynamics of Photodissociation of the Gas Phase $(N_2O{\cdot}H_2O)^+$ Cluster Ion. *Int. J. Mass. Spectrom.* **1992**, *117*, 507-536.

25. Brenton, A. G. Translational Energy Spectroscopy. *J. Mass Spectrom.* **1995**, *30*, 657-665.

26. Yang, X.; Lin, J.; Lee, Y. T.; Blank, D. A.; Suits, A. G.; Wodtke, A. M. Universal Crossed Molecular Beams Apparatus with Synchrotron Photoionization Mass Spectrometric Product Detection. *Rev. Sci. Instrum.* **1997**, *68*, 3317-3326.

27. Lin, J. J.; Hwang, D. W.; Harich, S.; Lee, Y. T.; Yang, X. New Low Background Crossed Molecular Beam Apparatus: Low Background Detection of H_2. *Rev. Sci. Instrum.* **1998**, *69*, 1642-1646.

28. Brenton, A. G. Translational-Energy Spectroscopy: A Personal Perspective of its Development. *Int. J. Mass Spectrom.* **2000**, *200*, 403-422.

29. Schmiedl, R.; Dugan, H.; Meier, W.; Welge, K. H. Laser Doppler Spectroscopy of Atomic Hydrogen in the Photodissociation of HI. *Z. Phys.* **1982**, *A304*, 137-142.

30. Nadler, I.; Mahgerefteh, D.; Reisler, H.; Wittig, C. The 266 nm Photolysis of ICN: Recoil Velocity Anisotropies and Nascent E,V,R,T Excitations for the CN + I($^2P_{3/2}$) and CN + I($^2P_{1/2}$) Channels. *J. Chem. Phys.* **1985**, *82*, 3885-3893.

31. Houston, P. L. Vector Correlations in Photodissociation Dynamics. *J. Phys. Chem.* **1987**, *91*, 5388-5397.

32. Chandler, D. W.; Houston, P. L. Two-Dimensional Imaging of State-Selected Photodissociation Products Detected by Multiphoton Ionization. *J. Chem. Phys.* **1987**, *82*, 1445-1447.

33. Heck, A. J. R.; Chandler, D. W. Imaging Techniques for the Study of Chemical Reaction Dynamics. *Annu. Rev. Phys. Chem.* **1995**, *46*, 335-372.

34. Suits, A. G.; Continetti, R. E. *Imaging in Chemical Dynamics*; American Chemical Society, Washington D. C., USA 2001.

35. Whitaker, B. *Imaging in Molecular Dynamics: Technology and Applications*, Cambridge University Press, Cambridge, UK, 2003.

36. Ashfold, M. N. R.; Nahler, N. H.; Orr-Ewing, A. J.; Vieuxmaire, O. P. J.; Toomes, R. L.; Kitsopoulos, T. N.; Garcia, I. A.; Chestakov, D. A.; Wu, S.-M.; Parker, D. H. Imaging the Dynamics of Gas Phase Reactions. *Phys. Chem. Chem. Phys.* **2006**, *8*, 26-53.

37. Chandler, D. W.; Houston, P. L.; Parker, D. H. Perspective: Advanced Particle Imaging. *J. Chem. Phys.* **2017**, *147*, 013601.

38. Eppink, A. T. J. B.; Parker, D. H. Velocity Map Imaging of Ions and Electrons Using Electrostatic Lenses: Application in Photoelectron and Photofragment Ion Imaging of Molecular Oxygen. *Rev. Sci. Instrum.* **1997**, *68*, 3477-3484.

39. Wiley, W. C.; McLaren, I. H. Time-of-Flight Mass Spectrometer with Improved Resolution. *Rev. Sci. Instrum.* **1955**, *26*, 1150-1157.

40. Castleman, K. R. *Digital Image Processing*; Prentice-Hall, Englewood Cliffs, NJ, USA 1979.

41. Renth, F.; Riedel, J.; Temps, F. Inversion of Velocity Map Ion Images Using Iterative Regularization and Cross Validation. *Rev. Sci. Instrum.* **2006**, *77*, 033103.

42. Kinugawa, T.; Arikawa, T. Three-Dimensional Velocity Analysis Combining Ion Imaging with Doppler Spectroscopy: Application to Photodissociation of HBr at 243 nm. *J. Chem. Phys.* **1992**, *96*, 4801-4804.

43. Tonokura, K.; Suzuki, T. Slicing Photofragment Spatial Distribution by Laser Sheet Ionization. *Chem. Phys. Lett.* **1994**, *224*, 1-6.

44. Gebhardt, C. R.; Rakitzis, T. P.; Samartzis, P. C.; Ladopoulos, V.; Kitsopoulos, T. N. Slice Imaging: A New Approach to Ion Imaging and Velocity Mapping. *Rev. Sci. Instrum.* **2001**, *72*, 3848-3853.

45. Neumark, D. M. Slow Electron Velocity-Map Imaging of Negative Ions: Application to Spectroscopy and Dynamics. *J. Phys. Chem. A* **2008**, *112*, 13287-13301.

46. Suits, A. G.; Miller, R. L.; Bontuyan, L. S.; Houston, P. L. Photofragment Vector Correlations by Ion Imaging: O_2 [a $^1\Delta_g(v,J)$] from 248 nm Dissociation of Ozone. *J. Chem. Soc., Faraday Trans.* **1993**, *89*, 1443-1447.

47. Suits, A. G.; Bontuyan, L. S.; Houston, P. L.; Whitaker, B. J. Differential Cross Sections for State-Selected Products by Direct Imaging: Ar+NO. *J. Chem. Phys.* **1992**, *96*, 8618-8620.

48. Lorenz, K. T.; Chandler, D. W.; Barr, J. W.; Chen, W.; Barnes, G. L.; Cline, J. I. Direct Measurement of the Preferred Sense of NO Rotation After Collision with Argon. *Science* **2001**, *293*, 2063-2066.

49. Kitsopoulos, T. N.; Buntine, M. A.; Baldwin, D. P.; Zare, R. N.; Chandler, D. W. Reaction Product Imaging: The H + D_2 Reaction. *Science* **1993**, *260*, 1605-1610.

50. Wester, R. Velocity Map Imaging of Ion–Molecule Reactions. *Phys. Chem. Chem. Phys.* **2014**, *16*, 396-405.

51. Meyer, J.; Wester, R. Ion–Molecule Reaction Dynamics. *Annu. Rev. Phys. Chem.* **2017**, *68*, 333-353.

52. Pei, L; Farrar, J. M. Imaging Ion–Molecule Reactions: Charge Transfer and Halide Transfer Reactions of O^+ with CH_3Cl, CH_3Br, and CH_3I. *Int. J. Mass Spectrom.* **2015**, *377*, 93-100.

53. Osterwalder, A.; Nee, M. J.; Zhou, J.; Neumark, D. M. High Resolution Photodetachment Spectroscopy of Negative Ions via Slow Photoelectron Imaging. *J. Chem. Phys.* **2004**, *121*, 6317-6322.

54. Neumark, D. M. Slow Electron Velocity-Map Imaging of Negative Ions: Application to Spectroscopy and Dynamics. *J. Phys. Chem. A* **2008**, *112*, 13287-13301.

55. Hock, C.; Kim, J. B.; Weichmann, M. L.; Yacovitch, T. I.; Neumark, D. M. Slow Photoelectron Velocity-Map Imaging Spectroscopy of Cold Negative Ions. *J. Chem. Phys.* **2012**, *137*, 244201(1-6).

56. Garand, E.; Yacovitch, T. I.; Neumark, D. M. Slow Photoelectron Imaging Spectroscopy of CCO^- and CCS^-. *J. Chem. Phys.* **2008**, *129*, 074312.

57. Gerardi, H. K.; DeBlase, A. F.; Leavitt, C. M.; Su, X.; Jordan, K. D.; McCoy, A. B.; Johnson, M. A. Structural Characterization of Electron-Induced Proton Transfer in the Formic Acid Dimer Anion, $(HCOOH)_2^-$, with Vibrational and Photoelectron Spectroscopies. *J. Chem. Phys.* **2012**, *136*, 134318.

58. León, I.; Yang, Z.; Liu, H.-T.; Wang, L.-S. The Design and Construction of a High-Resolution Velocity-Map Imaging Apparatus for Photoelectron Spectroscopy Studies of Size-Selected Clusters. *Rev. Sci. Instrum.* **2014**, *85*, 083106.

59. Patros, K. M.; Mann, J. E.; Jarrold, C. C. Photoelectron Imaging Spectra of O_2^-·VOC and O_4^-·VOC Complexes. *J. Phys. Chem. A* **2016**, *120*, 7828-7838.

60. Continetti, R. E. Coincidence Spectroscopy. *Annu. Rev. Phys. Chem.* **2001**, *52*, 165-192.

61. Bodi, A.; Shuman, N. S.; Baer, T. On the Ionization and Dissociative Photoionization of Iodomethane: A Definitive Experimental Enthalpy of Formation of CH_3I. *Phys. Chem. Chem. Phys.* **2009**, *11*, 11013-11021.

62. Benitez, Y.; Nguyen, T. L.; Parsons, A. J.; Stanton, J. F.; Continetti, R. E. Probing the Exit Channel of the OH + $CH_3OH \rightarrow H_2O + CH_3O$ Reaction by Photodetachment of $CH_3O^-(H_2O)$. *J. Phys. Chem. Lett.* **2022**, *13*, 142-148.

63. Beckert, M.; Greaves, S. J.; Ashfold, M. N. R. High Resolution Ion Imaging Studies of the Photodissociation of the Br_2^+ Cation. *Phys. Chem. Chem. Phys.* **2003**, *5*, 308-315.

64. Vieuxmaire, O. P. J.; Nix, M. G. D.; Fitzpatrick, J. A. J.; Beckert, M.; Dixon, R. N.; Ashfold, M. N. R. Predissociation of State Selected Br_2^+ Cations. *Phys. Chem. Chem. Phys.* **2004**, *6*, 543-554.

65. Sage, A. G.; Oliver, T. A. A.; Dixon, R. N.; Ashfold, M. N. R. Velocity Map Imaging Studies of the Photodissociation of H_2O^+ Cations. *Mol. Phys.* **2010**, *108*, 945-955.

66. Kim, M. H.; Leskiw, B. D.; Suits, A. G. Vibrationally Mediated Photodissociation of Ethylene Cation by Reflectron Multimass Velocity Map Imaging. *J. Phys. Chem. A* **2005**, *109*, 7839-7842.

67. Kim, M. H.; Leskiw, B. D.; Suits, A. G. Vibrationally Mediated Photodissociation of $C_2H_4^+$. *J. Phys. Chem. A* **2007**, *111*, 7472-7480.

68. Gichuchi, W. K.; Mebel, A. M.; Suits, A. G. UV Photodissociation of Ethylamine Cation: A Combined Experimental and Theoretical Investigation. *J. Phys. Chem. A* **2010**, *114*, 13296-13302.

69. Lepère, V.; Picard, Y. J.; Barat, M.; Fayeton, J. A.; Lucas, B.; Bèroff, K. Photodissociation Dynamics of Ar_2^+ and Ar_3^+ Excited by 527 nm Photons. *J. Chem. Phys.* **2009**, *130*, 194301.

70. Hoshino, H.; Yamakita, Y.; Okutsu, K.; Suzuki, Y.; Saito, M.; Koyasu, K.; Ohshimo, K.; Misaizu, F. Photofragment Imaging of Mass-Selected Ions Using a Reflectron Mass Spectrometer I. Development of an Apparatus and Application to Mg^+-Ar Complex. *J. Chem. Phys.* **2015**, *630*, 111-115.

71. Okutsu, K.; Ohshimo, K.; Hoshino, H.; Koyasu, K.; Misaizu, F. Photofragment Imaging of Mass-Selected Ions Using a Reflectron Mass Spectrometer. II: Formation Mechanism of MgF^+ in the Photodissociation of Mg^+–FCH_3 Complex. *Chem. Phys. Lett.* **2015**, *630*, 57-61.

72. Okutsu, K.; Yamazaki, K.; Ohshimo, K.; Misaizu, F. Photofragment Ion Imaging from Mass-Selected Mg^+BrCH_3 Complex: Dissociation Mechanism Following Photoinduced Charge Transfer. *J. Chem. Phys*. **2017**, *146*, 024301.

73. Okutsu, K.; Nakashima, Y.; Yamazaki, K.; Fujimoto, K.; Nakano, M.; Ohshimo, K.; Misaizu, F. Development of a Linear-Type Double Reflectron for Focused Imaging of Photofragment Ions from Mass-Selected Complex Ions. *Rev. Sci. Instrum.* **2017**, *88*, 053105.

74. Hopkins, W. S.; Hamilton, S. M.; McNaughter, P. D.; Mackenzie, S. R. VUV Photodissociation Dynamics of Diatomic Gold, Au_2: A Velocity Map Imaging Study at 157 nm. *Chem. Phys. Lett.* **2009**, *483*, 10-15.

75. Parry, I. S.; Hermes, A. C.; Kartouzian, A.; Mackenzie, S. R. Imaging the Photodissociation of Neutral Metal Clusters: Copper Dimer, Cu_2, and Copper Oxide, CuO. *Phys. Chem. Chem. Phys.* **2014**, *16*, 458-466.

76. Cooper, G. A.; Kartouzian, A.; Gentleman, A. S.; Iskra, A.; van Wijk, R.; Mackenzie, S. R. Dissociation Energies of Ag-RG (RG = Ar, Kr, Xe) and AgO Molecules from Velocity Map Imaging Studies. *J. Chem. Phys*. **2015**, *143*, 124302.

77. Cooper, G. A.; Gentleman, A. S.; Iskra, A.; Mackenzie, S. R. Photofragmentation Dynamics and Dissociation Energies of MoO and CrO. *J. Chem. Phys.* **2017**, *147*, 013921.

78. Maner, J. A.; Mauney, D. T.; Duncan, M. A. Imaging Charge Transfer in a Cation-π System: Velocity-Map Imaging of Ag^+(benzene) Photodissociation. *J. Phys. Chem. Lett.* **2015**, *6*, 4493– 4498.

79. Maner, J. A.; Mauney, D. T.; Duncan, M. A. Velocity Map Ion Imaging Study of Ar2+ Photodissociation. *Chem. Phys. Lett.* **2017**, *671*, 182– 185.

80. Johnston, M. D.; Pearson, W. L.; Wang, G.; Metz, R. B. A Velocity Map Imaging Spectrometer for Photofragments of Fast Ion Beams. *Rev. Sci. Instrum.* **2018**, *89*, 014102.

81. Johnston, M. D.; Lockwood, S. P.; Metz, R. B. Photofragment Imaging and Electronic Spectroscopy of Al_2^+. *J. Chem. Phys.* **2018**, *148*, 216308.

82. Johnston, M. D.; Gentry, M. R.; Metz, R. B. Photofragment Imaging, Spectroscopy, and Theory of MnO^+. *J. Phys. Chem. A* **2018**, *122*, 8047.

83. Rittgers, B. R.; Leicht, D.; Duncan, M. A. Cation-π Complexes of Silver Studied with Photodissociation and Velocity-Map Imaging. *J. Phys. Chem. A.* **2020**, *124*, 9166-9176.

84. Lockwood, S. P.; Chunga, T.; Metz, R. B. Bonding, Thermodynamics, and Dissociation Dynamics of NiO^+ and NiS^+ Determined by Photofragment Imaging and Theory. *J. Phys. Chem.* **2021**, *125*, 7425-7436.

CHAPTER 2

EXPERIMENTAL SETUP

Ion Sources and Mass Spectrometer

Mass Spectrometer

Ion complexes are generated in a custom-made molecular beam machine via laser vaporization or electrical discharge and analyzed with a "home built" reflectron time-of-flight mass spectrometer. Complexes are then photodissociated in the turning region of the reflectron using the second, third, or fourth harmonic of a Nd:YAG laser to study ion fragmentation patterns. The ion sources and time-of-flight mass spectrometer have been described in detail in the literature previously,[1-4] but an overview will be described here.

Figure 2.1 shows the time-of-flight mass spectrometer used for ion photodissociation spectroscopy. Ions are generated in the first chamber, referred to as the source, during a pulsed supersonic expansion of gas into the vacuum chamber. A series 9 General Valve (Parker Hannifin Corp.) powered by an Iota One (Parker Hannifin) pulse driver is used to pulse gas into the source at 10 Hz. Gas pulse widths between 200 to 400 μs with backing pressures varying from 80 to 250 psi are common for experiments. The expansion is generally composed of a rare gas seeded with a small amount of the ligand of interest. Ligands are entrained in the gas by using the vapor pressure above a liquid or creating a mixture of different gases. The source is evacuated with a 10 inch diffusion pump (Varian VHS-10, 5000 L/s He) that is backed by a mechanical pump (Edwards E2M80). Complexes formed in the molecular beam travel through a skimmer (Beam Dynamics 3 mm dia. aperture) into the mass spectrometer chamber.

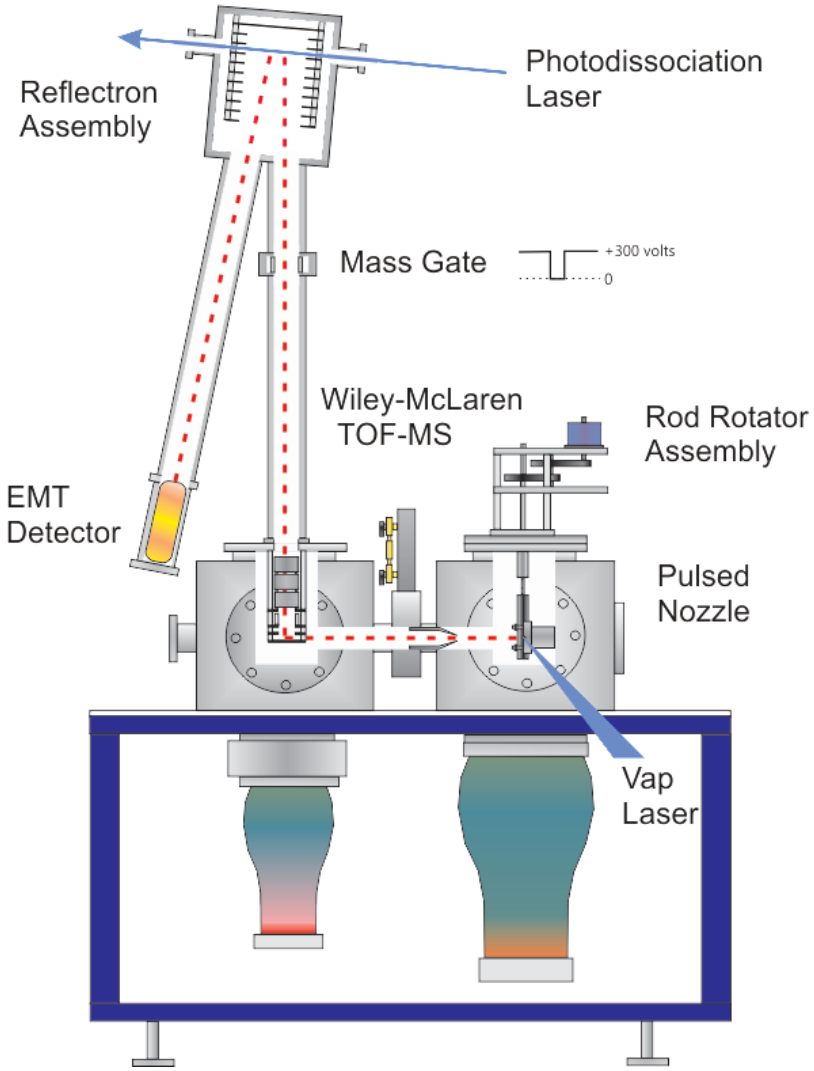

Figure 2.1. Instrumental apparatus depicting source chamber (right) and reflectron time-of-flight mass spectrometer.

The mass spectrometer is a Wiley-McLaren type time-of-flight (TOF) mass spectrometer fitted with a reflectron for increased mass resolution.[5] The chamber is kept at an idle pressure of ~9 X 10^{-8} torr with a 6 inch diffusion pump (Varian VHS-6, 2000 L/s He) attached to a water cooled baffle and backed by a mechanical pump (Edwards E2M40). Cations are pulse extracted orthogonal to the molecular beam axis through a two-field acceleration region composed of a repeller plate, draw-out-grid, and ground grid. The draw-out-grid voltage is adjusted to achieve maximum spatial focusing of the ions in the photodissociation region or at the detector. The electric field between the repeller and draw-out-grid is weak to provide the spatial focusing of ions. The higher electric field between the draw-out-grid and ground electrode is what produces most of the acceleration down the flight tube. A pair of deflection plates is used to compensate for the initial translational energy in the direction of the molecular beam which causes downstream drift of the ions. An einzel lens is also used for further focusing of the ions. After the einzel lens, ions enter a field free flight tube where their masses determine their flight time. Stanford DG535 and BNC 8010 pulse generators are used to synchronize all of the pulsed components and Stanford PS-350 or Bertan 205A-05R power supplies are used to supply all of the voltages.

The electric fields between the repeller, draw-out-grid, and ground electrode impart the same amount of kinetic energy into all of the ions. This means that the ions will travel through the flight tube at a rate which is inversely proportional to their mass which can be seen from the equation below:

$$KE = \frac{1}{2}mv^2 \quad (1)$$

where *m* is mass and *v* is velocity. Using the definition for velocity and rearranging Eq. 1, the following equation may be obtained.

$$m = \frac{2KEt^2}{d^2} \quad (2)$$

Because distance and kinetic energy are constant in our experiment, the ion masses can be determined by setting time zero to the firing of the extraction electrodes and tracking their flight time to an electron multiplier tube detector (Hamamatsu R595). When the ion of interest is determined, a pulsed deflection plate is used to mass select that ion before it enters the reflectron. A high voltage complement pulse maintains a voltage on the deflection plate that rejects all ions that pass through it other than the ion of interest. This allows for photodissociation studies of one cluster size at a time without interference from other ions.

The reflectron is composed of a stack of ring electrodes connected through a voltage divider, and high voltage is applied to the rear electrode. Ions immediately lose most of their kinetic energy due to the steep rise in the electric field at the entrance of the reflectron. As the ions travel deeper into the reflectron, their motion slows down further until they eventually stop before turning around and reaccelerate out of the reflectron. This is ideal for photodissociation studies, as a laser can be passed through the reflectron at the point where the ions turn around since this is where they spend most of the time relative to any other point in their flight path. Ions are dissociated using the second, third or fourth harmonic of a Nd:YAG laser (Spectra Physics GCR-170) or the doubled output of a dye laser (Spectra Physics PDL-2). After photodissociation, fragments are reaccelerated toward the detector along with any other parent ions.

A typical mass spectrum and photodissociation mass spectrum taken with this instrument can be seen in Figure 2.2. The photodissociation mass spectrum is obtained from taking an average with the laser off and subtracting that from an average with the photodissociation laser on. The amount of averaging is the same for both the laser on and laser off. This produces a mass

spectrum showing depletion of the parent ion intensity as a negative signal and formation of the fragment ions as positive signal. The mass spectrometer is optimized for fragment ion intensity, so the signal for parent ion depletion is not representative of its actual intensity. This method helps to ensure that the fragments we see are coming from the parent ion of interest.

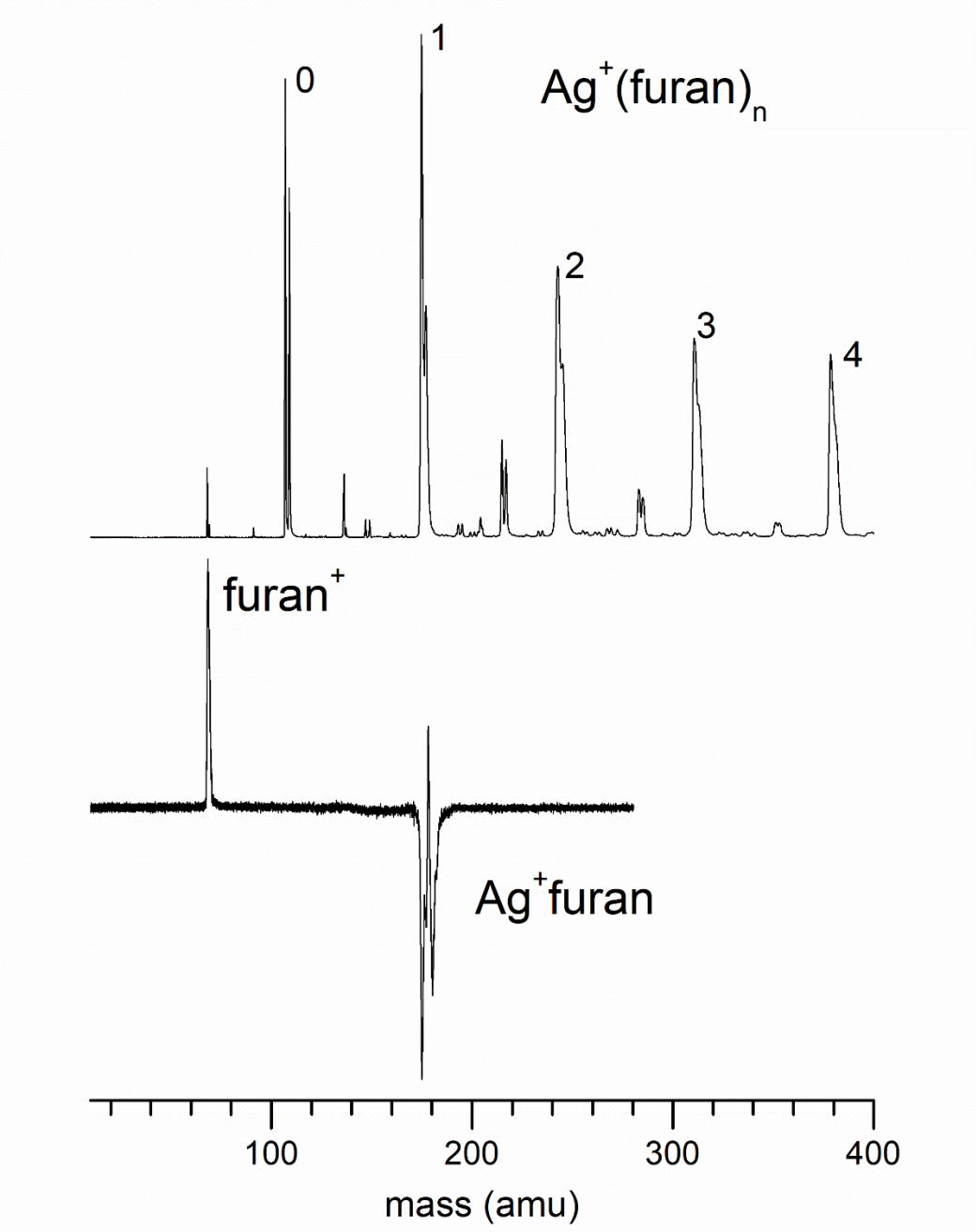

Figure 2.2. Example mass spectrum (top) and photodissociation mass spectrum of mass selected $Ag^+(C_7H_8)$ (bottom).

Laser Vaporization Source

The laser vaporization source has been reviewed previously.[4] This source is ideal for making atomic clusters and ion-molecule complexes in the gas phase of elements or substances that come in a solid form at room temperature. A schematic of two vaporization sources is shown in Figure 2.3. At the top is a depiction of the standard, or "block", source, which is designed to increase the number of atom-atom collisions in the confined flow region. This allows for an extended period of cluster growth which results in clusters containing multiple atoms of the element being vaporized. The bottom of Figure 2.3 depicts the "offset" source, which offers the advantage of a free expansion directly at the tip of the nozzle. This promotes the formation of ion-molecule complexes and also allows for a cooler expansion. For other versions of the laser vaporization source, the interested read is referred to reference 4. Laser light at 532 nm or 355 nm from a Nd:YAG (Continuum Surelite SL-10) is aligned and focused (1 mm beam diameter, quartz lens) to strike a rotating and translating rod in front of the nozzle. Laser power is regulated using beam splitters and irises (1 − 20 mJ/pulse), and is the most important variable for optimizing the laser vaporization source. The laser power should be iteratively optimized along with expansion pressure, pulse duration, and timing between the laser and expansion. As the beam strikes the rod, a plasma is generated that interacts with the expansion gas. Collisions within the expansion cool the plasma and promote condensation reactions between atoms, ions, electrons, ligands, and the buffer gas.

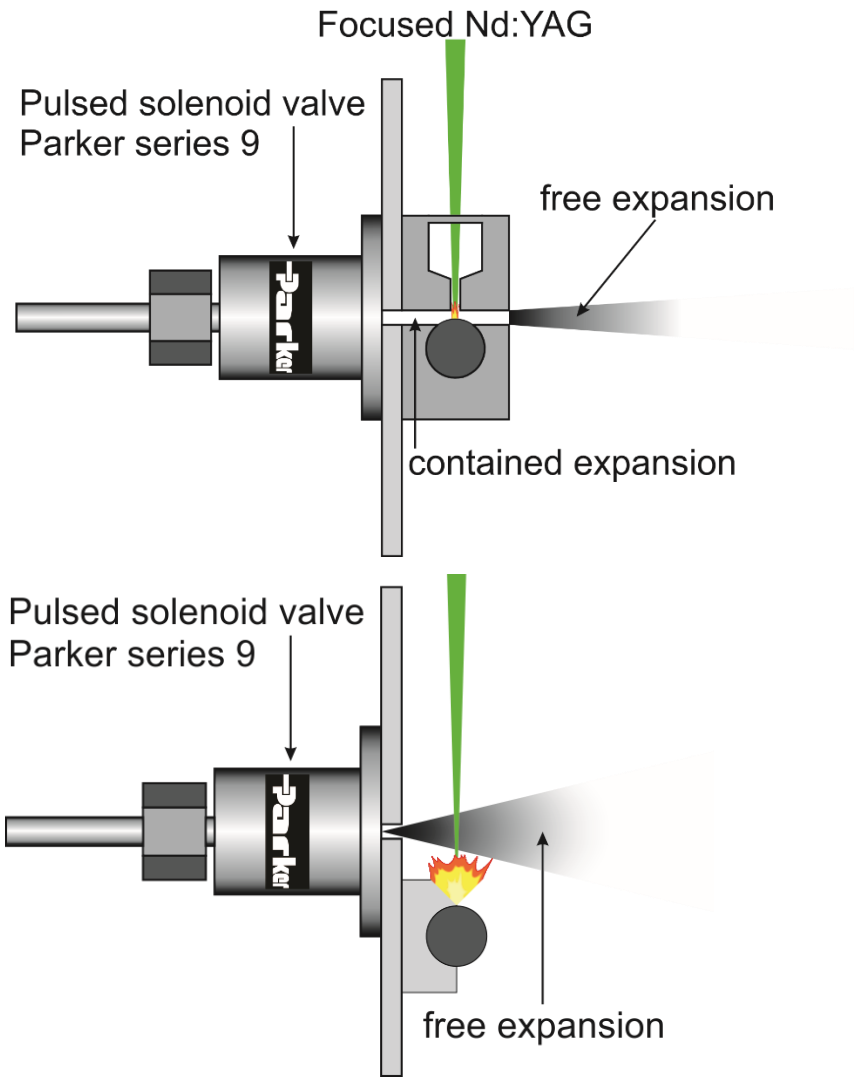

Figure 2.3. Diagram of two commonly used laser vaporization cluster sources. The standard source (top), or "block" source, can be extended with channels of varying lengths and diameters to change the cluster distribution. The "offset" source (bottom) allows for cooler expansions, but clusters generally contain only one metal atom.

Electrical Discharge Source

The pulsed discharge source is used to generate nonmetal ions in the gas phase. A diagram of the discharge source can be seen in Figure 2.4. Two sewing needles are placed through copper blocks and held in place with set screws. The needles are mounted ~1 mm apart. A razor blade can be used to determine the right distance, in front of the nozzle. A Teflon sheet with a hole in the position of the nozzle is placed between the blocks and the faceplate. One needle is connected to a high voltage pulser (DEI PVX-40) through the copper block. One copper block is connected to the HV pulser with a copper wire connected to a high vacuum feedthrough. This copper block is mounted onto the faceplate with nylon screws to isolate it from the chamber, while the other needle is grounded through the steel screws holding the copper block in place. A negative high voltage pulse is applied to the needle during the time of the gas expansion. The electrical pulse is generally 5 – 30 μs wide with voltages ranging from 500 – 1500 V. The discharge voltage and pulse width must be carefully monitored to ensure there is no overcurrent that can severely damage the electronics.

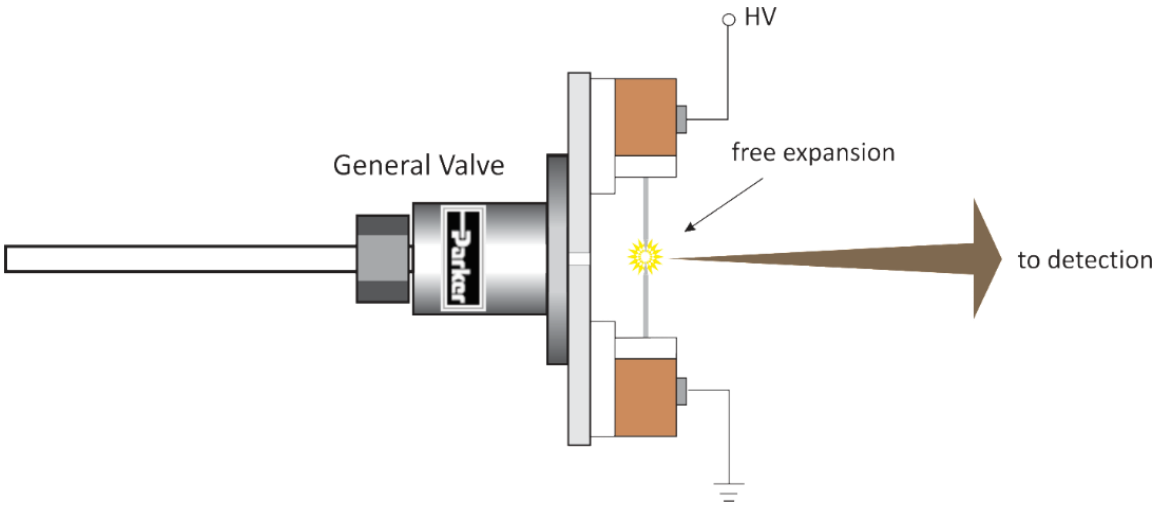

Figure 2.4. Diagram of pulsed electrical discharge source. A spark ignites the gap between two needles during the time of the gas expansion.

Selected-Ion Velocity Map Imaging Apparatus

The selected-ion velocity map imaging spectrometer was designed as a modification to the Wiley-McLaren TOF mass spectrometer in our lab (*vide supra*). The instrument can be seen in Figure 2.5. A hole was placed in the back plate of the reflectron and another section of flight tube containing the VMI components was connected to the back flange. The center of the additional flight tube is in line and centered with the first flight tube of the mass spectrometer. This chamber is evacuated with a turbomolecular pump (Pfeiffer HiPace 1200, 1200L/s N_2) backed by a mechanical pump (Pfeiffer DUO 20). The reflectron is grounded for imaging experiments, and ions are allowed to pass through it and into the VMI system. Once ions enter the VMI region, they are decelerated using a stack of ring electrodes and a voltage divider. The ions are then dissociated with the second, third, or fourth harmonic of a Nd:YAG laser (Spectra Physics GCR-170) or the doubled output of a dye laser (Spectra Physics PDL-2). The polarization of the dissociation lasers is set to vertical with either a half wave plate or a Fresnel double rhomb. After dissociation, fragment and parent ions are reaccelerated into a field free region with a set of electrostatic lenses configured for VMI.

A diagram of the VMI ion optics is shown in Figure 2.6. They were adapted from Suits' design for DC-slice imaging and incorporate electrodes for a deceleration field prior to the reacceleration field.[6] For ions accelerated at 2500 V by the repeller, the last decelerating electrode is set to 900 V, and a decelerating potential gradient is created by dividing that voltage over seven lenses. The first reacceleration lens, L1, is set to 805 V, L2 is 750 V, L3 is 700 V, and L4 is grounded. The last three lenses provide a ground shield against any stray voltages in this region.

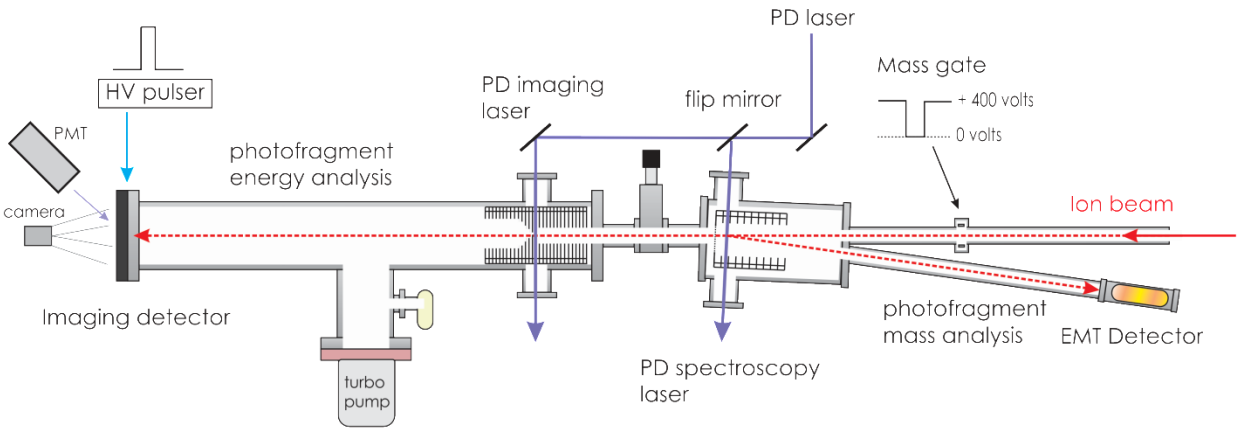

Figure 2.5. Schematic diagram for the selected-ion velocity map imaging apparatus.

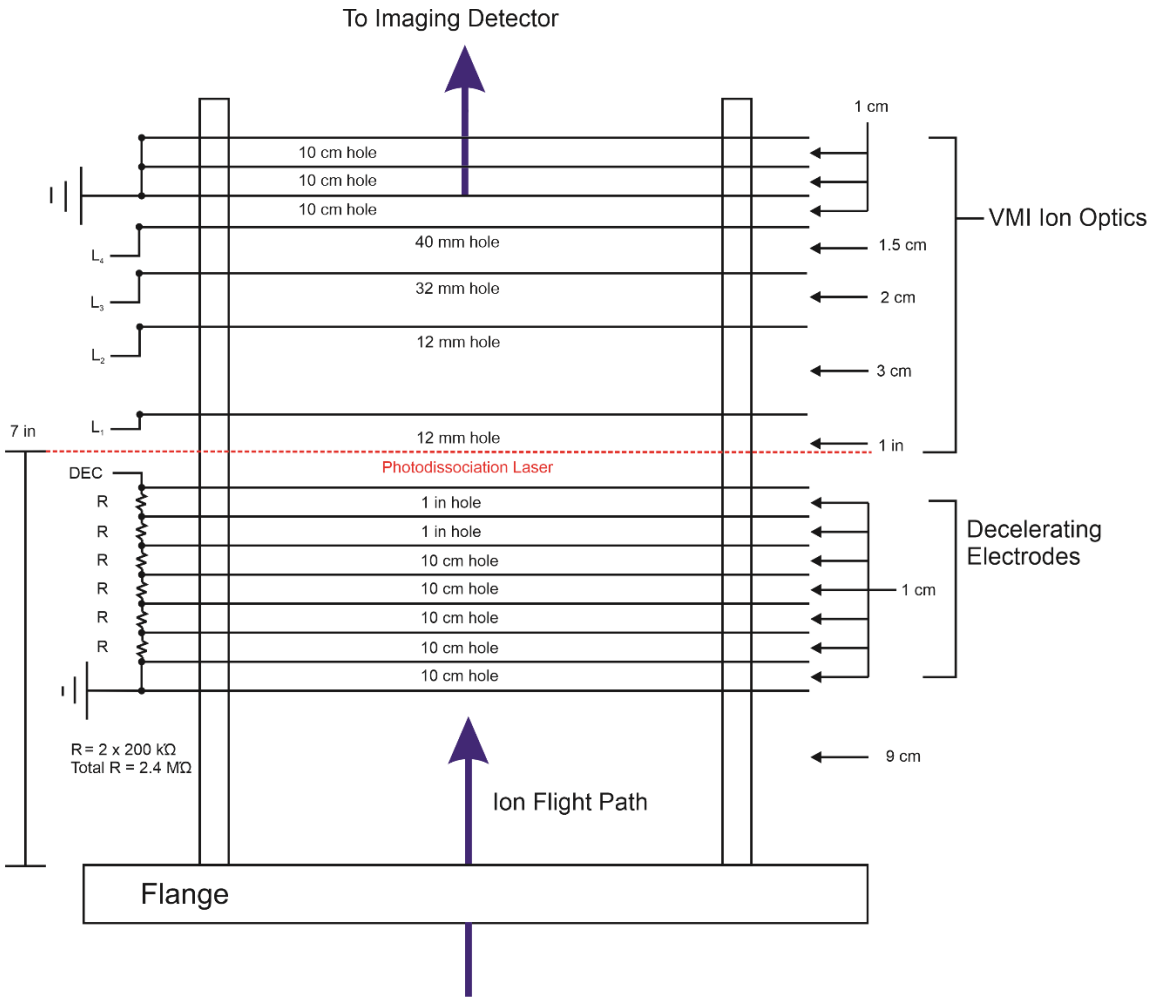

Figure 2.6. Ion optics for velocity map imaging.

Ions are focused onto a position sensitive dual MCP/phosphor screen detector (Beam Imaging Solutions BOS-75) that consists of two chevon microchannel plates coupled to a P47 phosphor screen. The front MCP is grounded to maintain the field free flight conditions in the tube. The back MCP has a gold coating that helps to improve electrical conduction for pulsed operation. The detector can be operated continuously, but must be pulsed for DC-slice imaging. For imaging in DC mode, the middle electrode of the MCPs is biased to 1000 V while the back is biased to 2000 V. For DC-slicing, the middle electrode is biased to 1000 V while the back floats at 1000 V. The back MCP is then pulsed from 1000 V to 2000 V using a high voltage pulser (DEI PVX-4140) for 140−200 ns to detect ions.[6] Because of the characteristic rise and fall times of the MCP, a gate of 140 ns results in an effective on time of 60 ns. Each time an ion hits the front of the first MCP, an electron cascade begins where the MCP was hit. The electrons then hit the phosphor screen in the same position where the MCP was originally impacted and it fluoresces. That fluorescence is monitored with a photomultiplier tube connected to a digital oscilloscope (Lecroy LT342) to measure flight time, and therefore mass, information. The P47 phosphor was chosen because of its very short fluorescence lifetime of 50 ns. Images are collected with a CCD camera (Edmund Optics) and the NuAcq acquisition software provided by the Suits' group, which includes a centroiding feature.[7] Images are collected over several hundred to over one million laser shots operating at a repetition rate of 10 Hz.

Image Analysis

Image processing like scaling, addition and subtraction, contrast, and "re-symmetrizing" is done with Fiji (NIH)[8] and a homemade Python script is used to add false color. It is possible to "re-symmetrize" images by summing over horizontal and vertical reflections of the original

image.[9] The Finite Slice Analysis program from the Suits' group is used for the image analysis.[10] Images can be reconstructed in Finite Slice Analysis or BASEX developed by the Reisler group.[10,11] These programs can generate the velocity and kinetic energy distributions and provide the integrated angular distributions, however, a velocity calibration factor must be given.

There are very few ions with well-known dissociation energies, so a good calibration factor is difficult to obtain. Alternatively, measuring the radius of the image and the ion flight time lets the ion velocity distribution be determined without needing a calibration factor, as long as the ions are reaccelerated close to their initial velocity. When the ions are accelerated to a much greater velocity than they originally had, there can be a magnification of the image that must be accounted for with the calibration. This does not make a geometrical approach tractable. The measured velocity can be used to determine the fragment kinetic energy with Equation 1. A typical photodissociation reaction can be described as:

$$AB^+ + h\nu \rightarrow A^+ + B + TKE$$

if AB^+ absorbs a photon with energy greater than the bond energy in the state being excited it will dissociate with excess energy TKE. Conservation of energy means that the extra energy above the dissociation threshold must be converted to translational, rotational, or vibrational energy. If A^+ and B are atomic fragments, that excess energy must go into translation and TKE must be the sum of the kinetic energy of A^+, $KE(A^+)$, and the kinetic energy of B, $KE(B)$, as seen in Equation 3.

$$TKE = KE(A^+) + KE(B) \quad (3)$$

The velocity and therefore kinetic energy of A^+ can be determined from the image of A^+ using the instrument describe above. Using the law of conservation of momentum, the following two equations can be obtained by substituting Equation 1 into Equation 3:

$$KE(A^+) = \left(\frac{m_B}{m_{AB}}\right) TKE \quad (4)$$

$$KE(B) = \left(\frac{m_A}{m_{AB}}\right) TKE \quad (5)$$

where m_A, m_B, and m_{AB} are the masses of A, B, and AB respectively. TKE could be determined by measuring the kinetic energy of either fragment, however only the image of the ion is typically obtained.

Photofragment imaging also measures the angular distribution of fragments after photodissociation, and the theory on this has already been studied extensively.[12-17] An experiment involving one excited electronic state accessed by one photon will have a photofragment distribution given by Equation 6:

$$I = \frac{1}{4\pi}[1 + \beta P_2(cos\ \theta)] \quad (6)$$

where I is the ion intensity, $P_2(cos\ \theta)$ is the second order Legendre polynomial, and θ is the angle between the electric field vector of the linearly polarized laser and the velocity vector of the ionic fragment. The anisotropy parameter, β, indicates what type of transition is being probed, i.e. parallel or perpendicular, and lies somewhere between -1 and 2. The electric field vector of the laser is aligned vertically in the lab frame and is parallel to the detector for a typical imaging experiment. This means that an ion dissociation via a parallel transition will have an angular distribution that is peaked at the top and bottom of the image, or 0° and 180°, and have a β value of ~2. A perpendicular transition will have a β value of -1 and be peaked left and right, or 90° and 270°.

When fitting the angular distribution with the programs mentioned above, two more parameters must be introduced into Equation 6 to give Equation 7:

$$I = \frac{A}{4\pi}[1 + \frac{\beta}{2}((3cos^2(\theta - C))] \quad (7)$$

where *A* allows for the amplitude to change in the equation and *C* corrects for small misalignments of the laser by taking into account the rotation of the image in the plane of the detector. $P_2(cos\ \theta)$ has been substituted into the equation to give the exact expression for the angular distribution. All data fitting is done in Origin 8.6.[18]

In order to calibrate and determine the energy resolution of the instrument, an ion with a well-known binding energy is used as a test. Ar_2^+ is one ion whose binding energy has been extensively studied and is known to a high degree of accuracy, so we use this system to calibrate We measure the velocity distribution of Ar^+ produced from the dissociation of Ar_2^+ at 355 nm at the same acceleration/deceleration voltages used in the study of new systems. An example image and kinetic energy release spectrum can be seen in Figure 2.7. This image was taken at an initial acceleration voltage of 2500 V, which is the "normal" operating acceleration voltage used in the experiment. If the voltages are raised or lowered, to account for more or less kinetic energy release, respectively, an image from the dissociation of Ar_2^+ or some other ion with a well-known binding energy must be recorded at these new operating voltages. From the image in Figure 2.7, we determine our energy resolution to be ± 0.14 eV. This is done by first finding the kinetic energy release value at the FWHM of the peak (2.06 eV) and at the point where signal starts to rise above the noise on the high energy side of the peak (2.34 eV). The difference between these two values is judged to be the full resolution of the instrument (0.28 eV). The high energy side of this resolution can then be placed at the threshold where signal starts to rise above the noise in an image from a different system (e.g., Ag^+(benzene)), and the center is used to determine the maximum kinetic energy release from that new system (e.g., Ag^+(benzene)).

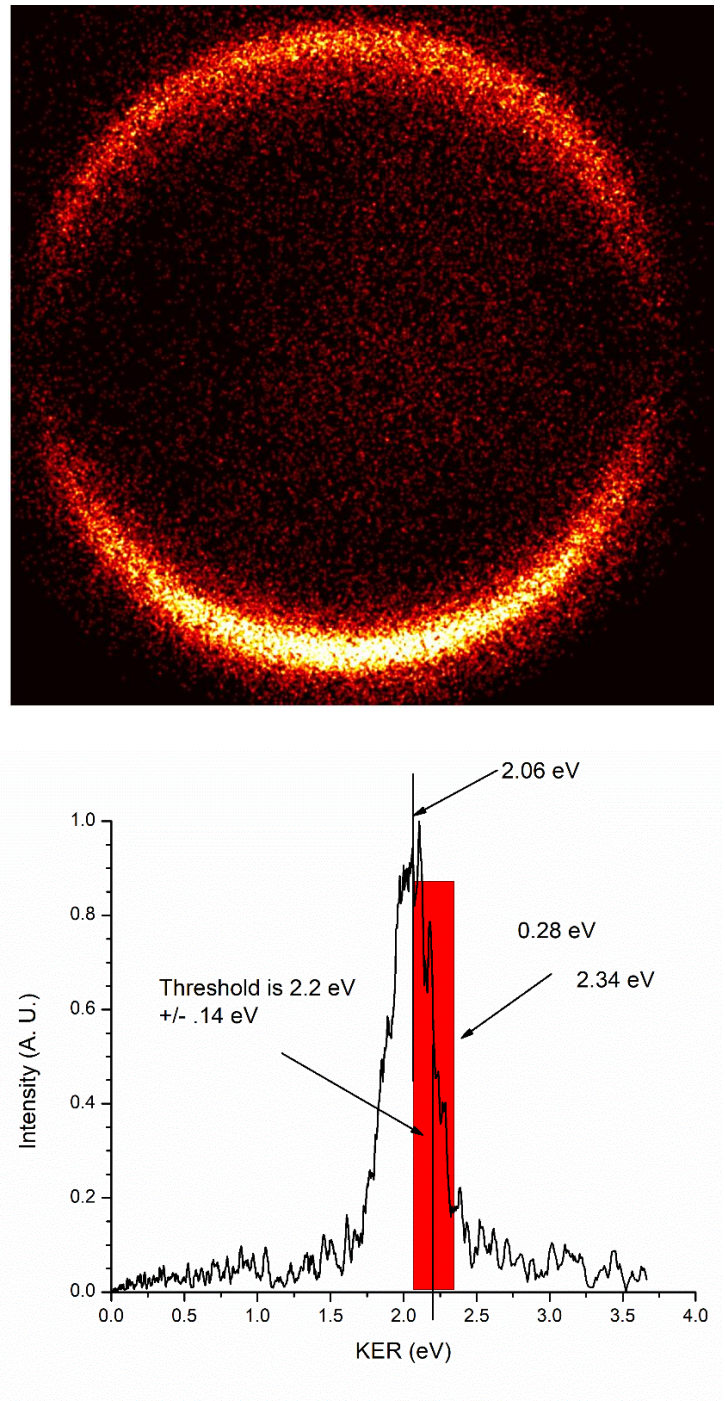

Figure 2.7. Image of Ar^+ (top) from 355 nm photodissociation of Ar_2^+ accelerated at 2.5 kV. The total kinetic energy release spectrum (bottom) determined from the image of Ar^+. The FWHM was determined to be 2.06 eV and the threshold for signal to be 2.34 eV. The difference between them determined the energy resolution in the experiment.

References

1. Dietz, T. G.; Duncan, M. A.; Powers, D. E.; Smalley, R. E. Laser Production of Supersonic Metal Cluster Beams. *J. Chem. Phys.* **1981**, *74*, 6511-6512.
2. LaiHing, K.; Cheng, P. Y.; Taylor, T. G.; Willey, K. F.; Peschke, M.; Duncan, M. A. Photodissociation in a Reflectron Time-of-Flight Mass Spectrometer: A Novel Mass Spectrometry/Mass Spectrometry Configuration for High-Mass Systems. *Anal. Chem.* **1989**, *61*, 1458-1460.
3. Cornett, D. S.; Peschke, M.; LaiHing, K.; Cheng, P. Y.; Willey, K. F.; Duncan, M. A. Reflectron Time-of-Flight Mass Spectrometer for Laser Photodissociation. *Rev. Sci. Instrum.* **1992**, *63*, 2177-2186.
4. Duncan, M. A. Laser Vaporization Cluster Sources. *Rev. Sci. Instrum.* **2012**, *83*, 041101/1-19.
5. Wiley, W. C.; McLaren, I. H. Time-of-Flight Mass Spectrometer with Improved Resolution. *Rev. Sci. Instrum.* **1955**, *26*, 1150-1157.
6. Townsend, D.; Minitti, M. P.; Suits, A. G. Direct Current Slice Imaging. *Rev. Sci. Instrum.* **2002**, *74*, 2530-2539.
7. Li, W.; Chambreau, S. D.; Lahankar, S. A.; Suits, A. G. Megapixel Ion Imaging with Standard Video. *Rev. Sci. Instrum.* **2005**, *76*, 063106. See also NuAcq 0.9 software, Suits, A. G., http://faculty.missouri.edu/suitsa/Technical_Resources.html.
8. Schindelin, J.; Arganda-Carreras, I.; Frise, E.; Kaynig, V.; Longair, M.; Pietzsch, T.; Preibisch, S.; Rueden, C.; Saalfeld, S.; Schmid, B.; Tinevez, J.-Y.; White, D. J.; Hartenstein, V.; Eliceri, K.; Tomancak, P.; Cardona, A. Fiji: An Open-Source Platform for Biological-Image Analysis. *Nature Methods*, **2012**, *9*, 676–682.

9. Suits, A. G.; Miller, R. L.; Bontuyan, L. S.; Houston, P. L. Photofragment Vector Correlations by Ion Imaging: O2 [a 1Δg(v,J)] from 248 nm Dissociation of Ozone. *J. Chem. Soc., Faraday Trans.* **1993**, *89*, 1443-1447.
10. Thompson, J. O. F.; Amarasinghe, C.; Foley, C. D.; Suits, A. G. Finite Slice Analysis (FINA) – A General Reconstruction Method for Velocity Mapped and Time-Sliced Ion Imaging. *J. Chem. Phys.* **2017**, *147*, 013913(1-14). See also Finite Slice Analysis Software, Suits, A. G., http://faculty.missouri.edu/suitsa/Technical_Resources.html.
11. Dribinski, V.; Ossadtchi, A.; Mandelshtam, V. A.; Reisler, H. "Reconstruction of Abel-Transformable Images: the Gaussian Basis-Set Expansion Abel Transform Method. *Rev. Sci. Instrum.* **2002**, *73*, 2634-2642.
12. Zare, R. N. Doppler Line Shape of Atomic Fluorescence Excited by Molecular Photodissociation. *Proc. IEEE* **1963**, *51*, 173-182.
13. Zare, R. N. Photoejection Dynamics. *Mol. Photochem.* **1972**, *4*, 1-37.
14. Zare, R. N. *Angular Momentum*; John Wiley & Sons, Inc., New York, NY, USA 1988.
15. Rakitzis, T. P.; Zare, R. N. Photofragment Angular Momentum Distributions in the Molecular Frame: Determination and Interpretation. *J. Chem. Phys.* **1999**, *110*, 3341-3350.
16. Yang, S.-C.; Bersohn, R. Theory of the Angular Distribution of Molecular Photofragments. *J. Chem. Phys.* **1974**, *61*, 4400-4407.
17. Siebbeles, L. D. A.; Glass-Maujean, M.; Vasyutinskii, O. S.; Beswick, J. A. Vector Properties in Photodissociation: Quantum Treatment of the Correlation Between the Spatial Anisotropy and the Angular Momentum Polarization of the Fragments. *J. Chem. Phys.* **1994**, *100*, 3610-3623.
18. Origin 8.6; OriginLab Corporation, Northampton, MA, USA, 2011.

CHAPTER 3

PHOTODISSOCIATION AND VELOCITY MAP IMAGING OF SILVER CATION-π COMPLEXES

Introduction

The study of photochemistry and light-driven charge transfer processes, which are ubiquitous in chemistry and biology, requires a knowledge of how light interacts with matter, separates charge, and transfers energy.[1-4] Photoinduced charge transfer is a central process in photosynthesis and light-harvesting materials, and has been well-documented in the spectroscopy and photochemistry of a variety of inorganic and organometallic complexes, including early work by Mulliken.[5-13] It has also been observed in mass spectrometry for gas phase molecular ions. The first group to observe dissociative charge transfer (DCT) was that of Bower's in the visible spectra of atmospherically relevant ion-molecule complexes.[14-16] Our group first observed DCT in metal ion-molecule complexes in the photodissociation of Ag^+(benzene) and Ag^+(acetone).[17-20] Several other studies presented by Kleiber and co-workers[21-24] and Yeh and co-workers[25-29] have demonstrated similar DCT processes in other metal ion-organic molecule species. Photodissociative charge transfer is possible when the ionization potentials of the fragments lie close enough in energy where the difference between them is readily accessible by common laser photon energies. UV photons can easily overcome the difference between ionization potentials of metal atoms (6-9 eV) and aromatic molecules (8-10 eV) plus the binding energy in the ground state, which will cause DCT plus some release of excess energy. Recently, we have applied photofragment imaging to explore the kinetic energy release in similar

photodissociation processes.[30] This method provides direct insight into the energetics and dynamics of cation-π interactions. In this chapter, we investigate the kinetic energy release and energetics of Ag^+(benzene), Ag^+(toluene), Ag^+(furan).

There are many examples of metal ion-aromatic complexes in organometallic chemistry, which provide prototypical examples of cation-π interactions.[31-34] These types of complexes have been well studied in both experiment and theory.[35-48] The positive charge in these types of systems typically resides solely on the metal atoms in the ground state because their ionization energies are lower than that of ligands, such as benzene or toluene. Several laboratories have demonstrated this in collision induced dissociation (CID) experiments,[38,40,46] where the metal cation is the only dissociation product. As an example, Chen and Armentrout looked at the CID of Ag^+(benzene) and saw that only the silver cation was produced.[33] These experiments can also provide dissociation energies with the proper analysis, for which Chen and Armentrout determined a bond energy of 37.4 kcal/mol for Ag^+(benzene). The Armentrout group has also measured the binding energies of first row transition metal ion-benzene complexes for Ti through Cu.[40]

Metal cation-molecule excited electronic states correspond to excited atomic states of the metal ion and/or to the excited states of the molecule. The electronic spectroscopy on metal cation-ligand complexes in which the metal has low-lying excited has been done for several complexes, which allowed for the determination of their structures.[49-55] Metal cation-molecule complexes can also possess “charge transfer” states where the electronically excited state correlates to the neutral metal and the molecular cation. Many transition metals have ionization potentials in the 7-8 eV range, while many ligands have ionization potentials above 9 eV, so the charge transfer states lie higher in energy because of the difference in the ionization potentials

between metals and ligands.[17-30] For example, benzene has an ionization potential 9.24 eV,[56] which means the charge transfer asymptote in a metal ion-benzene complex will lie ~1−2 eV above the ground state dissociation limit. This type of charge transfer state is a characteristic of some of the low-lying excited states of these systems, and in some cases is the *only* low-lying excited state. Ag^+ has no low-lying excited states (the first being $4d^9 5s^1$ at 4.86 eV)[57] and the first excited states of benzene, toluene, and furan lie at 4.72 eV (262.6 nm),[58] 4.65 eV (266.8 nm),[59] and 6.04 eV (205.3 nm),[60] respectively. Therefore, complexes of Ag^+ with any of these ligands have only the charge transfer state when excited at low energies. These states can be recognized in photodissociation experiments by the production of the molecular cation as the photofragment ion instead of the atomic metal cation.[17-30]

Photodissociative charge transfer has been observed in several metal cation-π complexes with fixed frequency dissociation in the near-UV wavelength region and detecting the organic cation product.[17-30] In some cases, the wavelength was scanned and excitation spectra were measured recording the production of the organic cation, and the threshold for DCT was obtained.[18,21-24,26-28] An upper limit on the dissociation energy can be using this threshold and ionization potentials of the metal atom and the aromatic molecule with the following expression:

$$D_0''(M^+{-}L) \leq h\nu_0 - \Delta IP$$

where D_0'' is the cation-π bond energy, $h\nu_0$ is the threshold photon energy, and ΔIP is the difference in the ionization potentials between the metal atom and the organic molecule. This method has been applied previously by our group and the Yeh group to determine bond energies for the Ag^+(benzene)[15] and the Ag^+(furan)[27,28] complexes, respectively. More recently, our group has used velocity map imaging to record the kinetic energy release in the aromatic cation photoproduct following the DCT process.[30] The measured maximum kinetic energy release can

be used in a similar expression to the one above to obtain an upper limit on the metal cation-π binding energy without needing to scan the entire spectrum:

$$D_0''(M^+{-}L) \leq h\nu_{CT} - (KER + \Delta IP)$$

where $h\nu_{CT}$ is the input photon energy, KER is the maximum kinetic energy release, and the difference between these two values should equal $h\nu_0$ except for effects of the Franck-Condon factors of the vertical transition in obscuring the adiabatic threshold. Our initial work investigated the DCT of Ag^+(benzene) at 355 and 266 nm.[30] Complexes with the silver cation are particularly convenient for these types of studies because of their relatively simple electronic structure resulting from the closed-shell d^{10} configuration of Ag^+. In this chapter, this methodology will be used to investigate Ag^+(benzene) further as well provide data on the first imaging experiments of Ag^+(toluene) and Ag^+(furan).

Experimental

Silver cation-π complexes were produced via laser vaporization at 355 nm (Continuum Surelite SL-10) using the so-called "offset" source[61] and studied using the selected-ion velocity map imaging apparatus described in Chapter 2. Benzene, toluene, or furan were entrained in an argon expansion, taking advantage of their ambient vapor pressure above the liquid at room temperature. The configuration of the instrument was adjusted accordingly to record mass spectra and photodissociation mass spectra or photofragment images. Complexes of Ag^+(benzene), Ag^+(toluene), and Ag^+(furan) were mass selected and photodissociated using the third (355 nm) or fourth harmonic (266) of a Nd:YAG laser (Spectra Physics GCR-170) or 280 nm from the frequency-doubled output of a dye laser (Spectra Physics PDL-2). Laser power was kept ≤ 2 mJ/pulse and the laser polarization was set to vertical in the lab frame with either a $\lambda/2$

plate or a Fresnel double rhomb. For imaging, we use the DC-slice imaging technique.[62] A dual MCP/P47 phosphor detector (Beam Imaging Solutions BOS-75) is pulsed with a 140 ns gate, which results in the detection of the central ~90 ns of the molecular ion distribution. Images are collected over the course of 200,000-500,000 laser shots. A CCD camera (Edmund Optics) is used to record images in NuACQ with centroiding turned on. Images are analyzed using the Finite Slice Analysis software from the Suits group.[63] The images were not reconstructed; however it may be advantageous to reconstruct sliced or unsliced images showing vibrational structure using the BASEX algorithm of Reisler or the Finite Slice Analysis software of Suits.[63,64]

Computations were performed to calculate the structures, frequencies, and bond energies of Ag^+(benzene), Ag^+(toluene), and Ag^+(furan). Calculations were conducted using B3LYP and M06L functionals along with both the def2-TZVP and def2-QZVP basis sets. Frequencies were used to correct for zero-point vibrational energies and bond energies are corrected for this. The Gaussian 16 program package was employed to perform the calculations.[65]

Results and Discussion

A laser-generated plasma at the surface of a silver rod in the "offset" cluster source[61] configuration produces primarily atomic silver ions, not silver atom cluster ions as seen with other configurations. Collisions of these silver ions with molecules entrained in the expansion gas produce a variety of ion-molecule clusters of the form $Ag^+(L)_n$, where "L" indicates the molecular species. The conditions in the plasma produced from laser vaporization are gentle enough that intact molecules condense around the metal ion without any indication for a significant amount of fragmentation.[61] Figures 3.1 and 3.2 show mass spectra for Ag^+(toluene)$_n$

and $Ag^+(furan)_n$ clusters, respectively. The mass spectrum in Figure 3.1 shows mainly argon clustering around one silver ion, although it also shows a substantial amount of Ag^+(toluene) both with and without argon. The mass spectrum in Figure 3.2 shows that furan is the prominent ligand clustering around the silver ions. The difference in clustering is because of the much higher vapor pressure of furan, which means more furan is entrained in the expansion gas compared to toluene at room temperature. Mass spectra of $Ag^+(benzene)_n$ complexes have been reported in previous work.[30]

Photodissociation mass spectra collected at 355 nm are also shown at the bottom of Figures 3.1 and 3.2 for mass selected Ag^+(toluene) and Ag^+(furan). These fragmentation mass spectra are obtained in a difference mode of operation, where an average of the mass selected parent ion signal with the laser off is subtracted from an average with the laser on, which produces fragmentation and a decreased amount of parent. This produces a mass spectrum in which the parent ion signal appears as a negative peak, while the fragment ion signal appears positive. In both cases, the only fragment observed is that of the organic ion and not the silver ion. This is evident because the isotopic pattern is different between the parent ion depletion peak and the fragment peaks. The parent ion peak has the typical isotopic pattern of silver (107 and 109 amu; 51.8 and 48.2 % abundance) while the fragments have only one isotopic peak. Dissociation of Ag^+(benzene) at 355 nm from previous experiments showed similar results with the benzene cation being the only fragment observed.[17-19,30] These results indicate that Ag^+(benzene), Ag^+(toluene), and Ag^+(furan) undergo strictly dissociative charge transfer at 355 nm, which is consistent with previous work for these complexes. [17-19,27-30] DCT is also observed at 280 and 266 nm for these complexes.

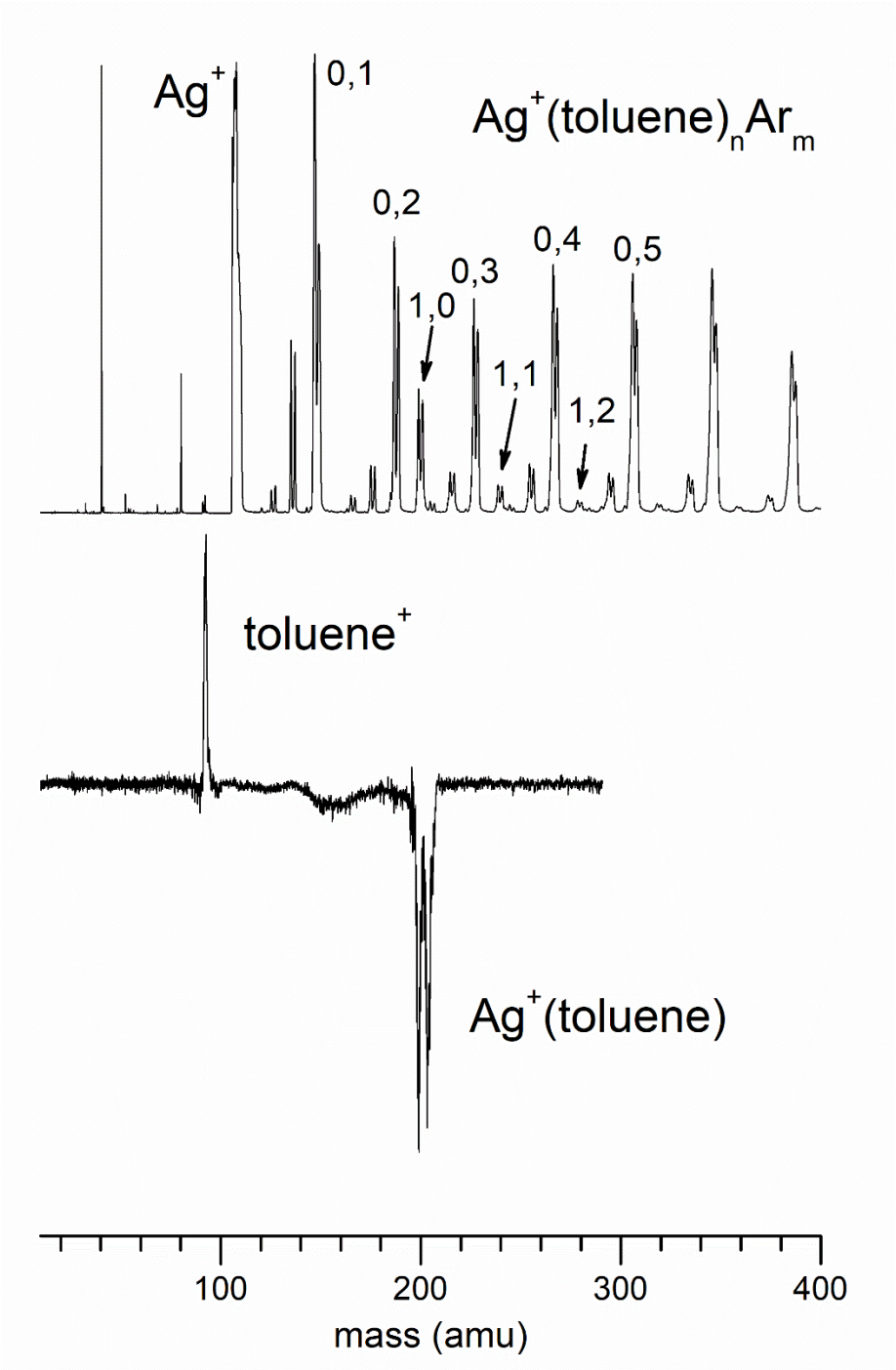

Figure 3.1. Mass spectrum (top) and 355 nm photodissociation mass spectrum (bottom) of Ag^+(toluene).

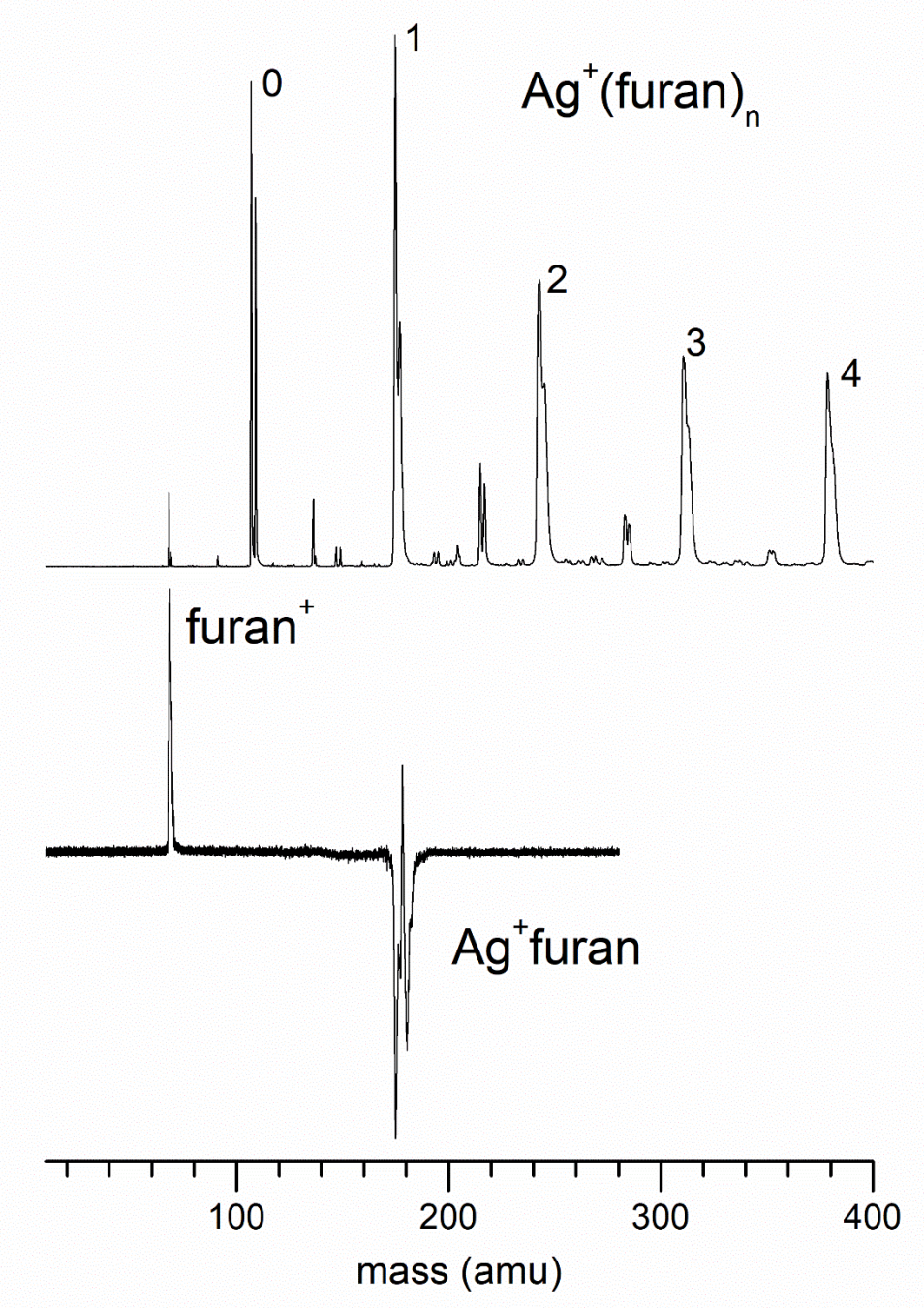

Figure 3.2. Mass spectrum (top) and 355 nm photodissociation mass spectrum (bottom) of Ag^+(furan).

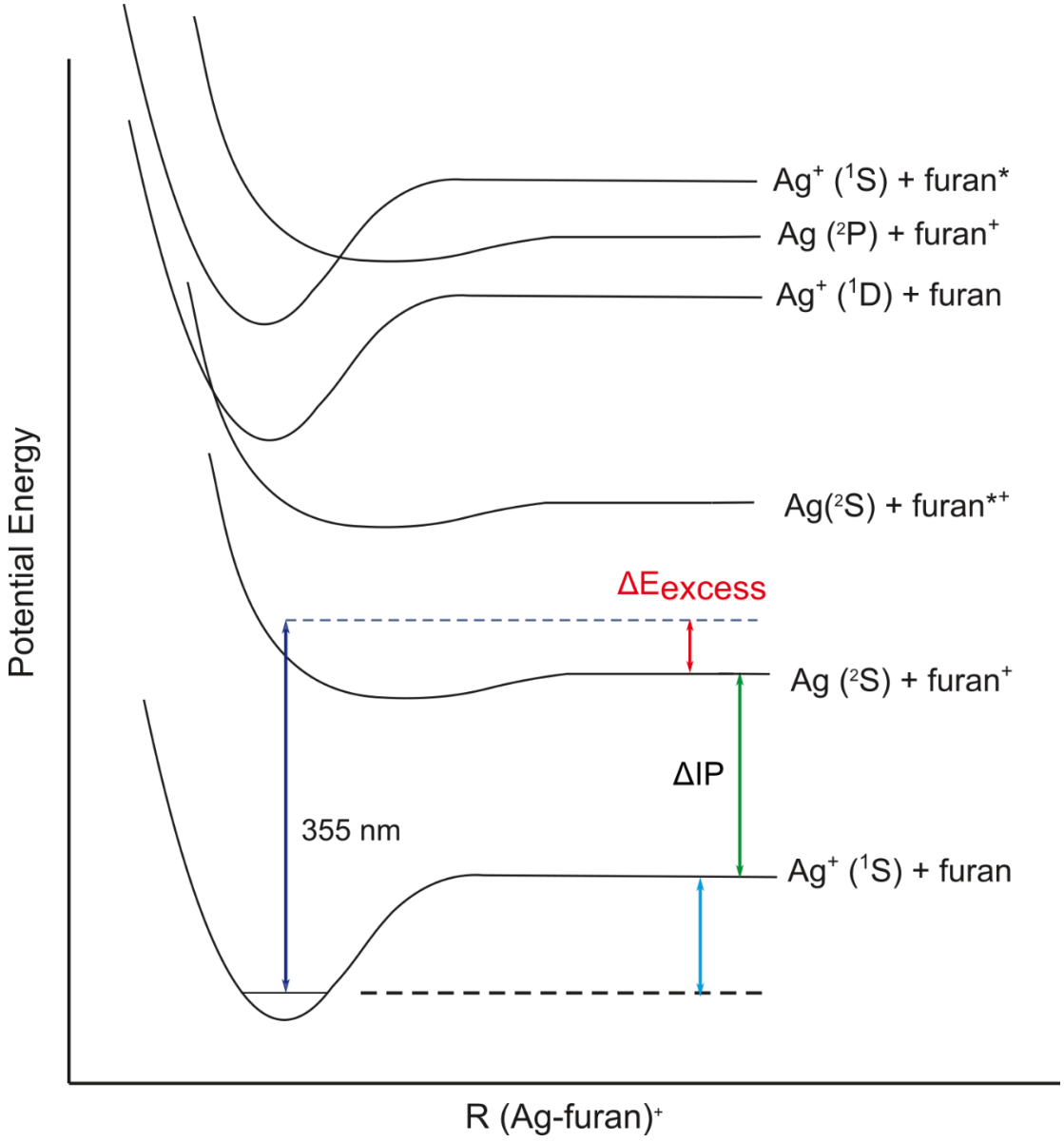

Figure 3.3. Schematic potential energy diagram for the Ag^+(furan) complex including the source of kinetic energy release.

The aromatic molecules used in these studies, along with the silver ion, have no low-lying excited state, so DCT is understandable for these ions. The only excited electronic state accessible at low energies corresponds to the charge transfer excited state as shown in Figure 3.3, which shows a schematic of the electronics states for the Ag^+(furan) complex. The ground state asymptote for this complex corresponds to the dissociation products Ag^+ + furan because of the lower ionization potential of silver (7.576 eV) than that of furan (8.886 eV).[66] This is also characteristic of the electronic states and energetics of the complexes with benzene and toluene, which have ionization potentials of 9.244 and 8.828 eV, respectively.[67,68] The states that correspond to a localized excitation on the silver ion or the furan molecule lie at high energies, while the charge transfer state lies at an intermediate energy whose asymptote corresponds to the difference in the ionization potentials of silver and furan (ΔIP = 1.310 eV). In the ground state, the silver ion is bound through cation-dipole interactions with the polarizable furan molecule. However, in the excited charge transfer state, the charge is delocalized throughout the organic ion which is not as effective in polarizing the neutral silver and is therefore more weakly bound than in the ground state. The transition into the charge transfer state accesses the repulsive wall and may lead to some kinetic energy release, which can be measured using photofragment imaging.

Figure 3.4 shows the results of geometry optimization calculations at the M06-L/def2-TZVP level. Calculations were also run at the M06-L/def2-TZVP, B3LYP/def2-QZVP, and B3LYP/def2-TZVP levels of theory. The full results of these computations can be seen in Appendix A. Table 3.1 shows the theoretical and experimentally measured bond energies for the systems studied here. The structure presented here for Ag^+(benzene) is the same as previously reported, with Ag^+ sitting η^2 above the edge of the benzene ring.[30,43] The computed dissociation

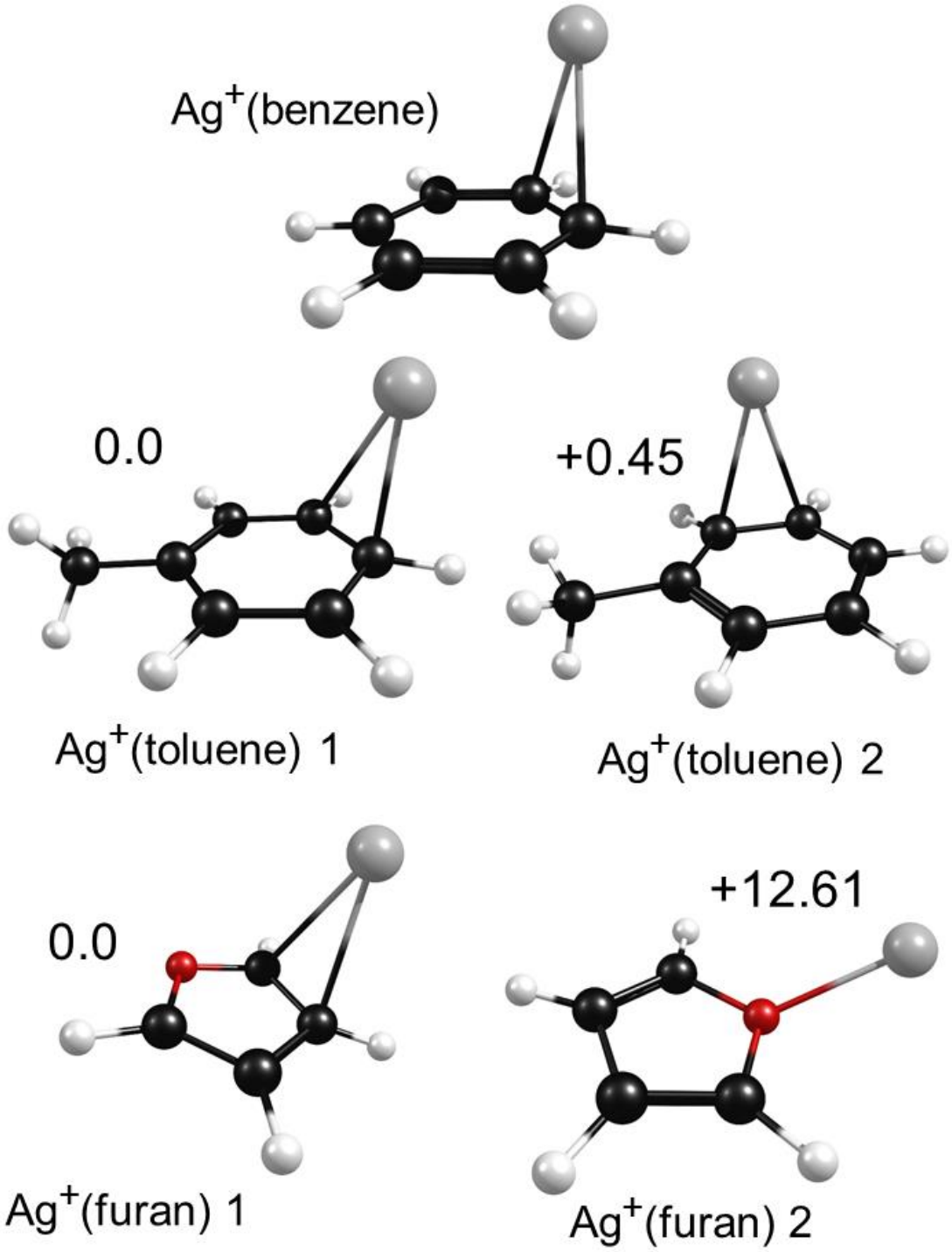

Figure 3.4. Computed structures and relative energies for Ag^+(benzene), Ag^+(toluene), and Ag^+(furan) at the M06-L/def2-TZVP level of theory.

Table 3.1. Ag^+(benzene), Ag^+(furan), and Ag^+(toluene) dissociation energies (in kcal/mol; ZPE corrected) resulting from our computations, compared to the upper limits derived here for these bond energies, and to the results of previous theory and experiment.

	B3LYP def2-TZVP	def2-QZVP	M06L def2-TZVP	def2-QZVP	Comparison
Ag^+(benzene)	37.83	38.30	36.58	37.53	$\leq 28.9 \pm 3.2$[a] ≤ 30.0[b] $\leq 32.8 \pm 1.5$[c] 37.4 ± 1.7[d] 35.4 ± 2.3[e] 44.2[f] 40.0[g]
Ag^+(toluene)					$\leq 35.9 \pm 3.2$[a]
Isomer 1	40.86	41.38	39.38	40.29	
Isomer 2	40.03	40.55	38.92	39.84	
Ag^+(furan)					$\leq 26.3 \pm 3.2$[a] ≤ 28.1[h]
Isomer 1	37.21	37.51	35.70	36.55	
Isomer 2	24.95	25.64	22.66	23.94	

[a]present experiments.
[b]tunable laser threshold spectroscopy (ref. 18).
[c]previous imaging experiments (ref. 30).
[d]collision-induced dissociation (ref. 37).
[e]reanalysis of data in ref. 36 (ref. 67).
[f]MP2 theory (ref. 41).
[g]CCSD(T) theory (ref. 41).
[h]tunable laser threshold spectroscopy (ref. 27).

energies (36−38 kcal/mol) are similar to that in our previous study (37.3 kcal/mol),[30] but somewhat lower than that obtained in older studies (40−44 kcal/mol).[37] The Ag^+(toluene) complex binds similarly, except that Ag^+ sits closer to one carbon above the ring. There are also two different sites for silver binding, either opposite or adjacent to the methyl group, with the more stable isomer being the silver bound further away from the methyl. The exact position of Ag^+ and relative energies vary slightly depending on the level of theory, but they are reflected in differences in the Ag^+(toluene) binding energies. At the B3LYP/def2-TZVP level of theory, isomer 1 is predicted to be more stable than isomer 2 by 0.9 kcal/mol. The computed bond energies of the two isomers are almost the same (39−41 kcal/mol), but higher than that of Ag^+(benzene) by 2−3 kcal/mol. Ag^+(furan) is also predicted to have two stable isomers, with the lower energy structure having the silver ion sitting η^2 above the two carbons adjacent to the oxygen (isomer 1). The higher energy isomer has the silver ion binding to the oxygen atom and slightly out of the plane of the ring (isomer 2); it is predicted to be less stable than isomer 1 by 12.3 kcal/mol at the B3LYP/def-2TZVP level of theory. As a result, isomer 2 is predicted to have a lower dissociation energy (23−26 kcal/mol) than isomer 1 (36−38 kcal/mol).

Imaging Ag^+(benzene)

Images of the benzene cation obtained from 355, 280, and 266 nm dissociation can be seen in Figure 3.5. This ion has been studied previously in our ion imaging experiment at 355 and 266 nm,[30] and the images presented here at those wavelengths are consistent with those of the previous experiment. Figure 3.5 shows the raw images of the benzene cation (left) from DCT and the resulting total kinetic energy release distribution (right) from analysis of the images. As can be seen from the images and KER spectra, the benzene cation is produced with a wide range

of kinetic energy values from the DCT process. This indicates that a portion of the excess energy is deposited into the rotational and/or vibrational degrees of freedom. The silver ion sits asymmetrically above the benzene the ring, which can lead to a significant torque placed on the benzene during dissociation. Therefore, it is possible that the dissociation also results in rotational and/or vibrational excitation. Franck-Condon factors may also play a role in the internal excitation of the benzene ion coming from the vertical transition from the ground state into the charge transfer state. The internal energy distribution must be matched by the same distribution of kinetic energies. It can be seen in Figure 3.5 that the distribution of kinetic energies ranges from 0 to ~1 eV, although the majority of the signal lies between 0.2 and 1.0 eV. This indicates that a significant portion of benzene fragment ions are produced with at least some kinetic energy, and very few have the entire amount of excess energy deposited into the internal degrees of freedom. This can also be seen from inspection of the raw image at 355 nm dissociation, which shows very little signal at the center of the image. However, the raw image from 266 and 280 nm dissociation has a greater amount of signal in the center, which indicates a greater number of ions produced with near zero kinetic energy release and a greater amount of internal excitation.

The yellow arrows in Figure 3.5 indicate the laser polarization, which is set vertically in the lab frame and parallel to the face of the detector. As can be seen in the image at 355 nm, the signal is concentrated in lobes on the top and bottom with a partial node going from left to right. Fitting this angular distribution as described in chapter 2 results in a β parameter of 0.38. A similar distribution is seen for dissociation at 280 nm ($\beta = 0.37$), while a more isotropic distribution is seen at 266 nm ($\beta = 0.17$). These values are presented in Table 3.2, and the fits to the angular distributions can be seen in Appendix A. The anisotropy of the images at 355 and

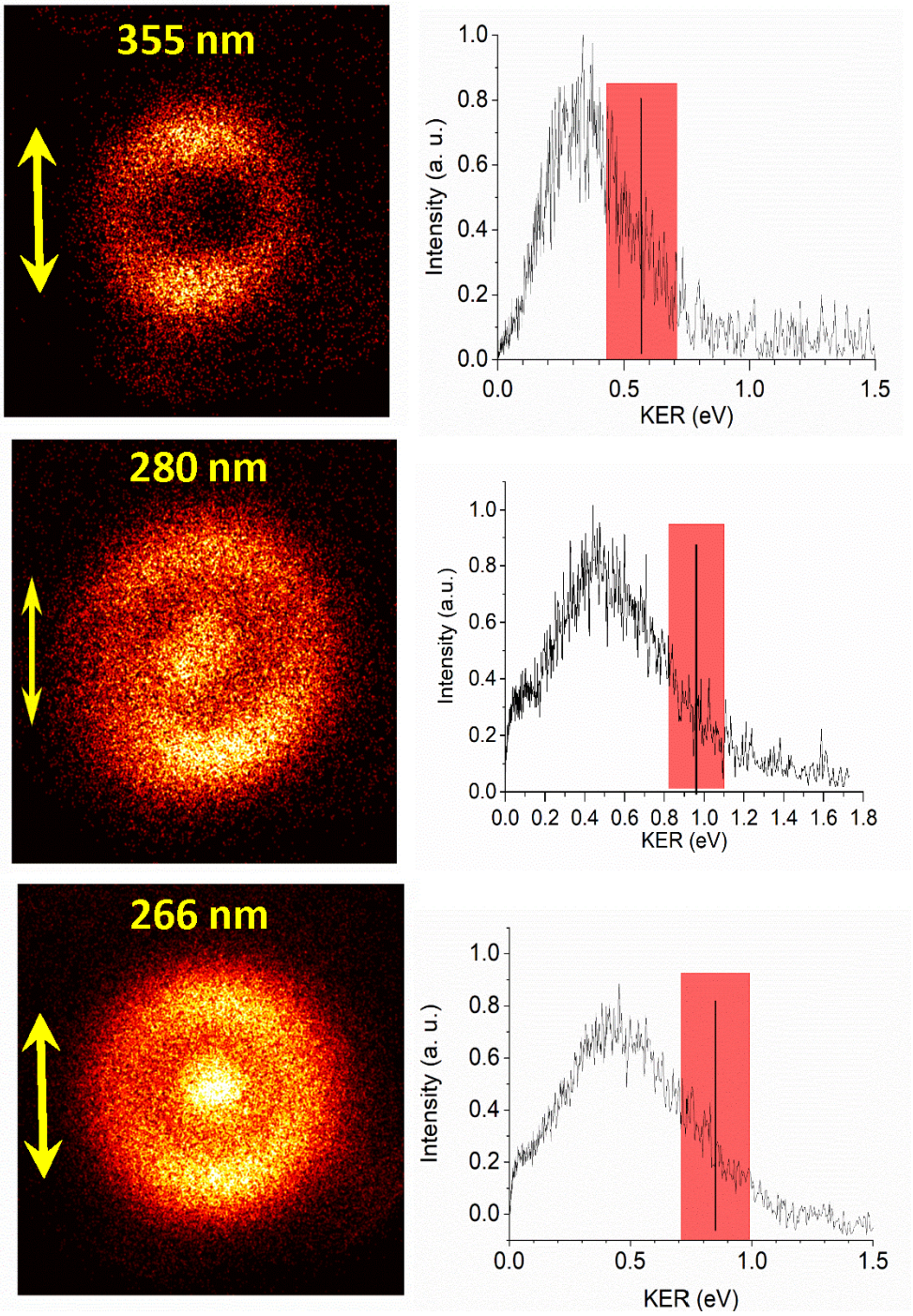

Figure 3.5. Raw images and kinetic energy release spectra for Ag^+(benzene) 355 nm (top), 280 nm (middle), and 266 nm (bottom). Yellow arrows indicate laser polarization, and red boxes indicate uncertainties in KER values.

Table 3.2. Ionization energies, dissociation wavelengths, measured kinetic energy release values, anisotropy parameters, and derived upper limits to the bond energies for the Ag^+(benzene), Ag^+(toluene), and Ag^+(furan) complexes studied here.

Complex	ΔIP (eV)	λ Exc. (nm)	Max. KER (eV)	D_0" Limit (kcal/mol)	β Parameter
Ag^+(benzene)	1.668	355	0.57	28.9 ± 3.2	0.38
Ag^+(benzene)	1.668	280	0.96	41.6 ± 3.2	0.37
Ag^+(benzene)	1.668	266	0.85	49.4 ± 3.2	0.17
Ag^+(toluene)	1.252	355	0.68	35.9 ± 3.2	0.42
Ag^+(toluene)	1.252	266	0.86	58.8 ± 3.2	0.07
Ag^+(furan)	1.310	355	1.04	26.3 ± 3.2	1.17
Ag^+(furan)	1.310	266	0.86	57.4 ± 3.2	0.91

280 nm is greater than that seen at 266 nm, which is almost isotropic. This result may stem from different Franck-Condon factors at the higher excitation energy, resulting in greater vibrational excitation prior to dissociation. Electronic mixing between the charge transfer state and the HOMO−LUMO transition in benzene could also result in a more isotropic image. This transition in benzene is excited near 260 nm;[58] if the transition moment for this excitation is different from that of the charge transfer state it would cause a more isotropic distribution. Also, if there were predissociation involving such a state, it could cause or allow rotation in the excited state complex before the fragments separate. This would wash out any of the initial polarization of the transition.

Even though the images indicate that there is a significant amount of energy deposited into the rotational/vibrational modes of the benzene ion at each wavelength, the outer edge still provides useful information about the complex bond energy. The maximum KER value obtained from the outside edge of the image represents a lower limit on the total excess energy, however, because we cannot guarantee that these ions had the full excess energy transferred into translational energy. The black line in the KER spectra of Figure 3.5 shows the maximum KER obtained from analyzing the images. The shaded region represents the uncertainty of the measurement which is derived from the instrument resolution. The instrument resolution is determined by the width of the Ar^+ image from photodissociation of Ar_2^+, as described in Chapter 2, under the same beam conditions. A detailed analysis showing how the maximum kinetic energy release is determined can be seen in Appendix A. Briefly, a baseline level for noise is determined. The signal level rising above this baseline level on the high KER side of the spectrum is set as the upper limit to our instrument resolution. The maximum KER is then assigned as the center value determined from the from the width of the instrument resolution.

Using this method, the maximum KER determined from dissociating at 280 nm is 0.96 ± 0.14 eV. Taking this value along with the photon energy and the difference in the ionization potentials of Ag (7.576 eV) and benzene (9.244 eV),[67] ΔIP = 1.668 eV, and upper limit to the Ag^+(benzene) bond energy is calculated to be 41.6 ± 3.2 kcal/mol. The error bars are due mainly to the uncertainty in the measurement, as the photon energy and ionization potentials are known with a much higher accuracy. The maximum KER determined using 355, 280, and 266 nm dissociation wavelengths are presented in Table 3.2. The maximum KER detected at 355 and 266 nm wavelengths are 0.57 and 0.85 eV, which are slightly different than those previously reported by our group.[30] We have improved our method for determining the edge of the image and our calibration, which resulted in slightly different values and wider error bars for the images reproduced here. The higher KER obtained at 280 nm compared to that at 355 nm reflects to some extent the higher excitation energy. The lower KER at 266 nm compared to that at 280 nm is reasonable with the significant change in image anisotropy. This is probably due, in some extent, to electronic state mixing and a larger amount of excess energy deposited into the internal degrees of freedom of the benzene cation.

The different values of KER determined at the different wavelengths give different limits on the Ag^+(benzene) dissociation energy. Using the energetic cycle as described previously in this chapter, we determined upper limits of 28.9 ± 3.5, 41.6 ± 3.5, and 41.6 ± 3.5 kcal/mol at 355, 280, and 266 nm, respectively. The tightest limit on bond energy comes at 355 nm, which is lower than previously reported with our imaging experiment (32.8 ± 1.5 kcal/mol).[30] This is because of the new calibration and image analysis method, which also increased our error bars but made them more realistic. This new number is, however, in better agreement with our previous result of 30.0 kcal/mol,[18] which was obtained by finding the threshold for charge

transfer by scanning a tunable laser. The new number is also lower than the value obtained in the previous CID experiment by Armentrout and co-workers who initially reported a bond energy of (37.4 ± 1.7 kcal/mol) that was later revised (35.4 ± 2.3 kcal/mol) by reanalyzing the original data.[30,33] It is also lower than the values obtained in the computations performed here and previously, which found dissociation energies between 34 – 44 kcal/mol.[37,43]

Ag^+(toluene) Imaging

The images and KER spectra for the Ag^+(toluene) complexes are shown in Figure 3.6. Again, the left frames are the raw images of the toluene cation photofragment, while the right frames are the kinetic energy release distribution. The yellow arrows in the image indicated laser polarization. The top of the figure represents 355 nm photodissociation, while the bottom is for photodissociation at 266 nm. A detailed analysis of the images is given in Appendix A. The image from 355 nm dissociation looks similar to that of Ag^+(benzene) at the same wavelength. It is less intense on the left and right vs. top and bottom and has only a small amount of signal in the center. The image shows a broad distribution of KER values, which can be attributed to factors similar to those for the Ag^+(benzene) images. Computations predict two isomers, with the carbon sitting above a C−C bond in the ring in both isomers, which could cause a significant amount of torque during dissociation. A fit of the angular distribution gives a β parameter of 0.42, which is slightly more isotropic than the Ag^+(benzene) image.

The image and angular distribution for dissociation at 266 nm is drastically different than those at 355 nm. The image intensity is concentrated in the center, gradually trails down at higher KER values, and there is virtually no anisotropy. This means that most of the available excess energy goes into the internal degrees of freedom of the toluene cation and not into

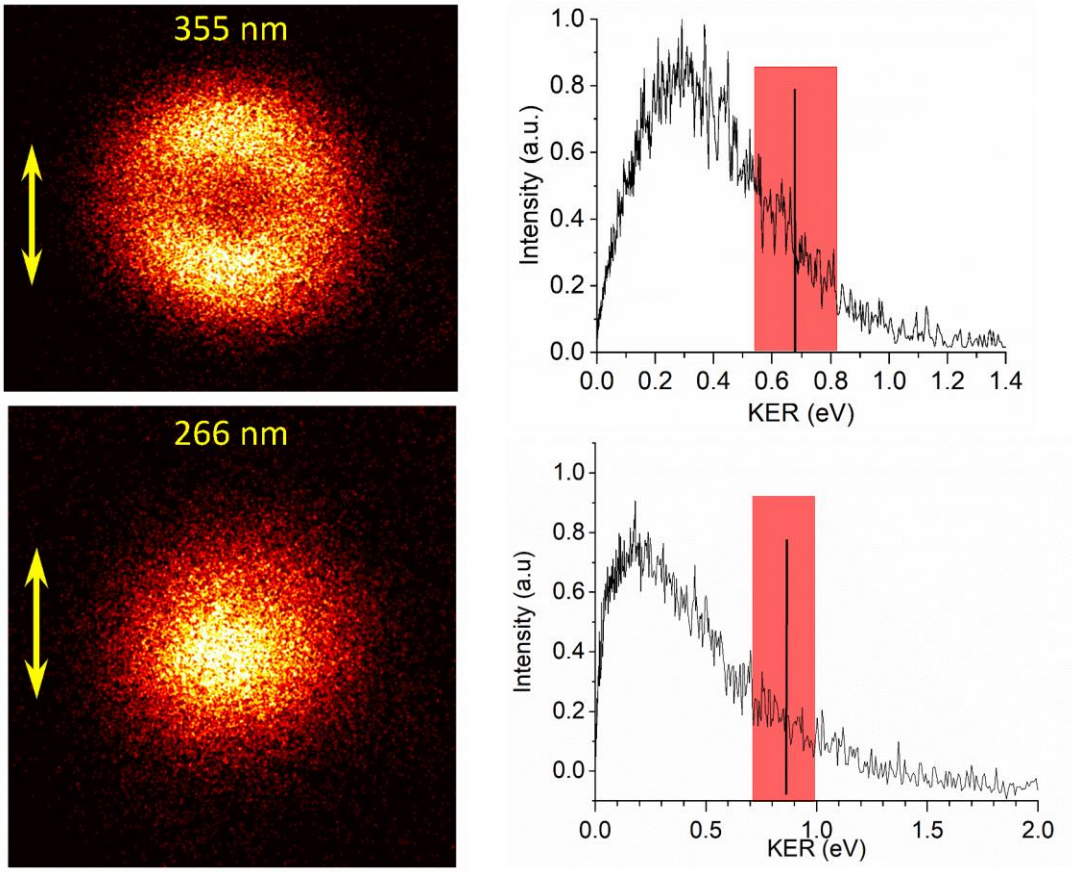

Figure 3.6. Raw images of the toluene cation and KER spectra from photodissociation of Ag^+(toluene) at 355 and 266 nm.

translational energy. There are several possible explanations for this difference at high excitation energy; the most intriguing is the possibility of excited electronic state mixing. The first excited electronic state of toluene is lower in energy than that of benzene at 266.8 nm,[59] so there might be some excitation of the neutral toluene along with the charge transfer. However, dissociation must occur on the charge transfer potential energy surface to produce the toluene cation, the measured fragment ion. But excitation into a state with mixed character that was followed by predissociation before fragmentation could result in rotation of the parent and/or excitation of the internal degrees of freedom causing a loss of KER, which would be consistent with a more isotropic KER distribution.

Even if there is a large internal excitation of the organic fragment ion, the maximum KER value can still be used to put an upper limit on the dissociation energy. The maximum KER values for Ag^+(toluene) were 0.68 and 0.86 eV for dissociation at 355 and 266 nm, respectively. The data for 355 nm excitation provides the tightest limit on the dissociation energy. The difference in the ionization potentials of Ag (7.576 eV) and toluene (8.828 eV)[68] is 1.252 eV. Using this value along with the photon energy, and upper limit on the bond energy of Ag^+(toluene) was determined to by 35.9 ± 3.2 kcal/mol. The value for the predicted bond energy in this system varies between the functionals and basis sets used, as well as between the isomeric structures. These values are presented in Table 1, and are within the range of 39−41 kcal/mol. Similar to the results for Ag^+(benzene), this upper limit is well below that predicted by theory for either isomer. In this case, the only other experimental work to compare to puts an upper limit on the dissociation energy at ≤ 58 kcal/mol,[39] much higher than presented here, and there are no other computational studies to compare to.

Our studies suggest that the bond energy for Ag^+(toluene) is greater than that for Ag^+(benzene). However, this is not surprising based on previous work by Schwarz and coworkers on transition metal-arene cation complexes.[42] In that study, they noted that electron donating groups, such as -CH_3, which increases the electron density within the ring, which facilitates cation-π interactions and increases the bond energy. However, the systems studied had the metal in an η^6 position above the six-fold symmetry axis of the aromatic ring, and it is unclear if this trend holds true when the metal binds along the edge of the ring. Wheeler and coworkers have more recently suggested that local-dipoles, rather than shifts in electron density, are responsible for binding in cation-π systems with substituted benzenes.[69,70] Although it seems clear that the binding is stronger in Ag^+(toluene) than in Ag^+(benzene), it would be beneficial for further computational work to be done to provide a more detailed explanation of the difference in the electrostatic interactions in these systems.

Ag^+(furan) Imaging

The raw images of the furan cation and KER spectra from the photodissociation of Ag^+(furan) at 355 nm and 266 nm are presented in Figure 3.7. A detailed analysis of the images and spectra can be found in Appendix A. The images of the furan cation at both 355 and 266 nm are more anisotropic than either of the Ag^+(benzene) or Ag^+(toluene) complexes. The KER distribution is still somewhat broad, suggesting internal excitation of the furan cation, however, there are well-defined lobes of intensity towards the top and bottom of the image and little signal towards the center of the image. The β values obtained from fitting the angular distribution of the furan cation in the images is 1.17 and 0.91 for photodissociation at 355 and 266 nm, respectively. The first excited state in furan is at a much higher energy than for either benzene or toluene, so it

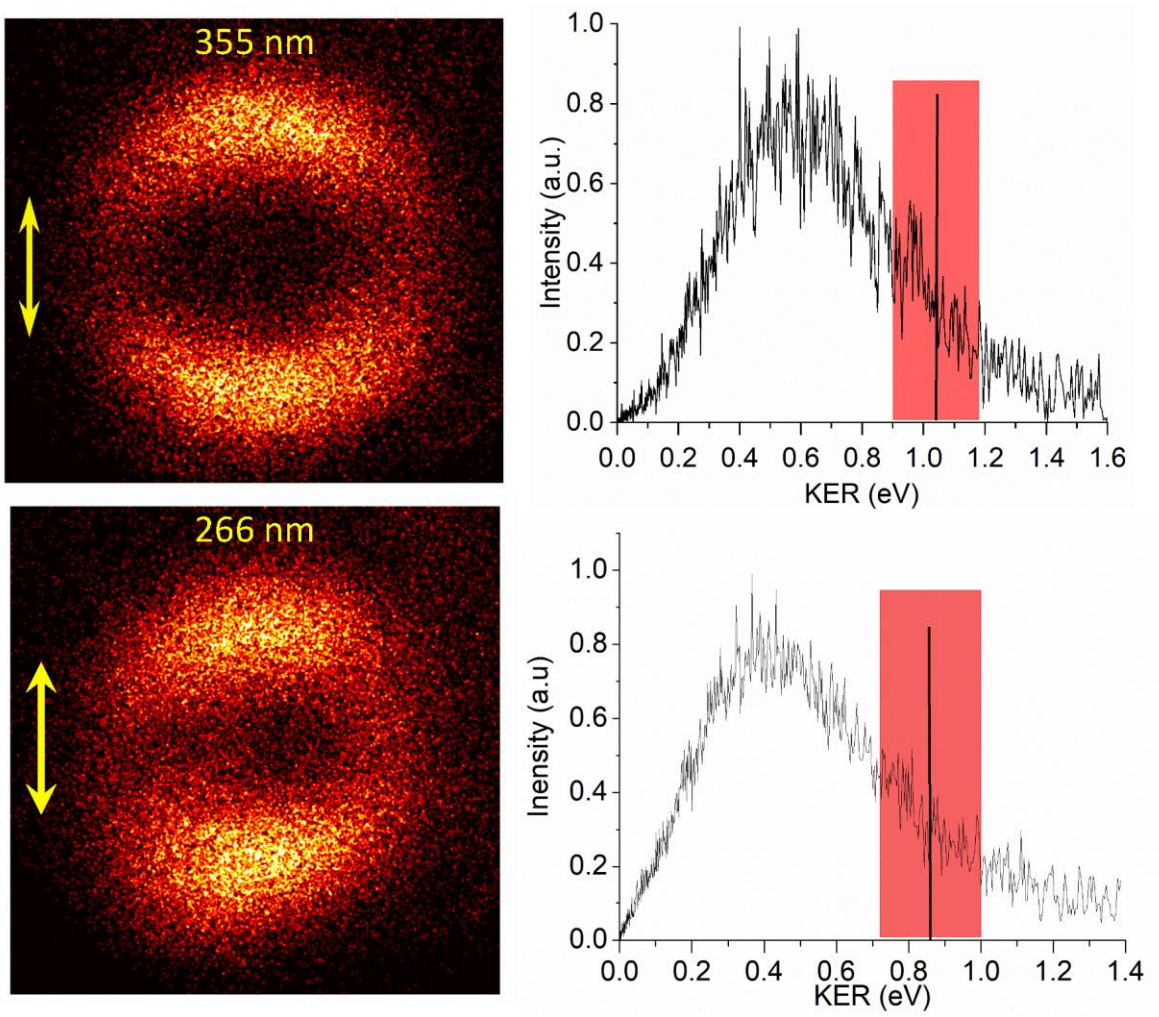

Figure 3.7. Raw images of the furan cation and KER spectra from photodissociation of Ag^{+}(furan) at 355 and 266 nm.

is therefore unlikely that there is any electronic mixing with the charge transfer state and that the images are coming from dissociation off of a purely charge transfer potential.

The same procedure used for Ag^+(benzene) and Ag^+(toluene) is used for determining the maximum kinetic release in these images as was used for Ag^+(benzene) and Ag^+(toluene). Using the maximum KER, along with the difference in ionization potentials of silver (7.576 eV) and furan (8.886 eV), $\Delta IP = 1.310$ eV, and the photon energy, an upper limit on the dissociation energy of Ag^+(furan) was determined to be 26.3 ± 3.2 and 57.4 ± 3.2 kcal/mol at 355 and 266 nm, respectively. These values compare to the computed bond energies here for isomers **1** and **2** of 35−38 and 22−26 kcal/mol, respectively.

The data obtained at 266 nm is so high as to be consistent with the binding energies computed for either isomer. However, the upper limit obtained with 355 nm dissociation, 26.3 ± 3.2 kcal/mol, can help shed some light on the isomer(s) present in this study. This value is not consistent with the predicted binding energy of isomer **1**, 35−38 kcal/mol. It seems to suggest that we are detecting isomer **2** instead of isomer **1**, even though it is much less stable. Interestingly, Yeh and coworkers have also studied Ag^+(furan) using a tunable laser to scan for the threshold of the appearance of the furan cation and reported a bond energy (28.1 kcal/mol) similar to that reported here.[27] If there were any population of isomer **2** in Yeh's experiment, it could not rule out the presence of isomer **1**, as it would have a dissociation threshold that would overlap with isomer **2** beginning at a higher energy. This may also be the case in our experiment though. If isomer **1** were present, it would have a high energy limit ~0.6 eV, which might be hidden underneath the width of the KER distribution. Although, if the KER distribution were wide like the others seen here, then there should be signal at lower KER values coming from the center of the image, where there is none. It might also be expected for isomer **1** to produce a

more isotropic image, like Ag^+(benzene) or Ag^+(toluene). The predicted structure of isomer **1** is similar to the other complexes with the silver binding over a C-C almost perpendicular to the plane of the ring. If a significant amount of torque and internal excitation of the ring during dissociation caused the more isotropic images in the other complexes it is reasonable that the same would happen for isomer **1**. However, we cannot rule out the existence of isomer **1**, but it seems it is either not present or has much sharper KER profile than the other complexes presented here. To explain the high KER value seen in the image, there must be a significant amount of isomer **2** present, which is consistent with the results of Yeh and coworkers.[27] The presence of a more unstable isomer is surprising, but not entirely unreasonable. There have been other examples in infrared spectroscopy experiments where a less stable structure had been kinetically trapped and survived long enough to be detected.[71] It would be interesting to do infrared spectroscopy on the Ag^+(furan) complex to determine if both of the isomers are indeed present and what their relative abundances are.

Even though these imaging studies are not state selective and are sensitive to all of the ions regardless of their internal states, they provide new insights into the photodissociation dynamics of silver cation-π complexes. It has been shown that dissociation takes place impulsively on an excited state potential, which produces a significant amount of kinetic energy in the fragments. Because of the asymmetrical structure of these complexes, a significant amount of excess energy is placed into their ro-vibrational states, which causes a broad kinetic energy distribution. Ag^+(furan) has the narrowest KER spectrum and highest β value of the three systems studied here, presumably because the structure is more symmetric (isomer **2**). Excitation at higher energy generally produces a broader KER spectrum with less anisotropy, which could be attributed to more recoil off of the excited state surface or a greater geometry change between

ground and excited states, resulting in a Franck-Condon population of vibrational states. Electronic state mixing is another possible issue for the Ag^+(benzene) and Ag^+(toluene) complexes because of the excited states of the ligands that lie near the same energy as the higher wavelength excitations.

The upper limits placed on the bond energies are generally lower than those predicted by theory for these complexes and even other experiments, which is a significant issue. Comparison of the bond energies from theory and experiments is presented in Table 3.1. As mentioned earlier, Armentrout and coworkers have previously done CID on Ag^+(benzene) and determined a bond energy of 35.4 ± 2.3 kcal/mol after reanalysis of their data.[30,38] This value was higher than our initial imaging result (32.8 ± 1.5 kcal/mol) and the agreement is worse here with our revised number (28.9 ± 3.2 kcal/mol). The only experimental work for Ag^+(toluene) puts a much higher limit (58 ± 5 kcal/mol)[39] on the dissociation energy than our result here (35.9 ± 3.2 kcal/mol), which is lower than that predicted by theory by 4−5 kcal/mol. The result for the Ag^+(furan) bond energy presented here (26.3 ± 3.2 kcal/mol) is only slightly higher than that predicted by theory for isomer **2** and agrees within our error bars with the result presented by Yeh and coworkers (28.1 kcal/mol).[27] Thus, we are systematically lower for the benzene and toluene complexes, but agree reasonably well with theory and experiment for the furan complex.

Because of the issues found when determining the bond energies for Ag^+(benzene) and Ag^+(toluene), the possible sources of error have been carefully considered. A higher kinetic energy release than there should be would result in lower values for the dissociation limits. This is possible if the ions in this experiment were not completely cooled and had unquenched internal energy prior to photodissociation. This has been tested with Ag^+(benzene) using different expansion gases in the source and the results are presented in Figure 3.8. Using helium

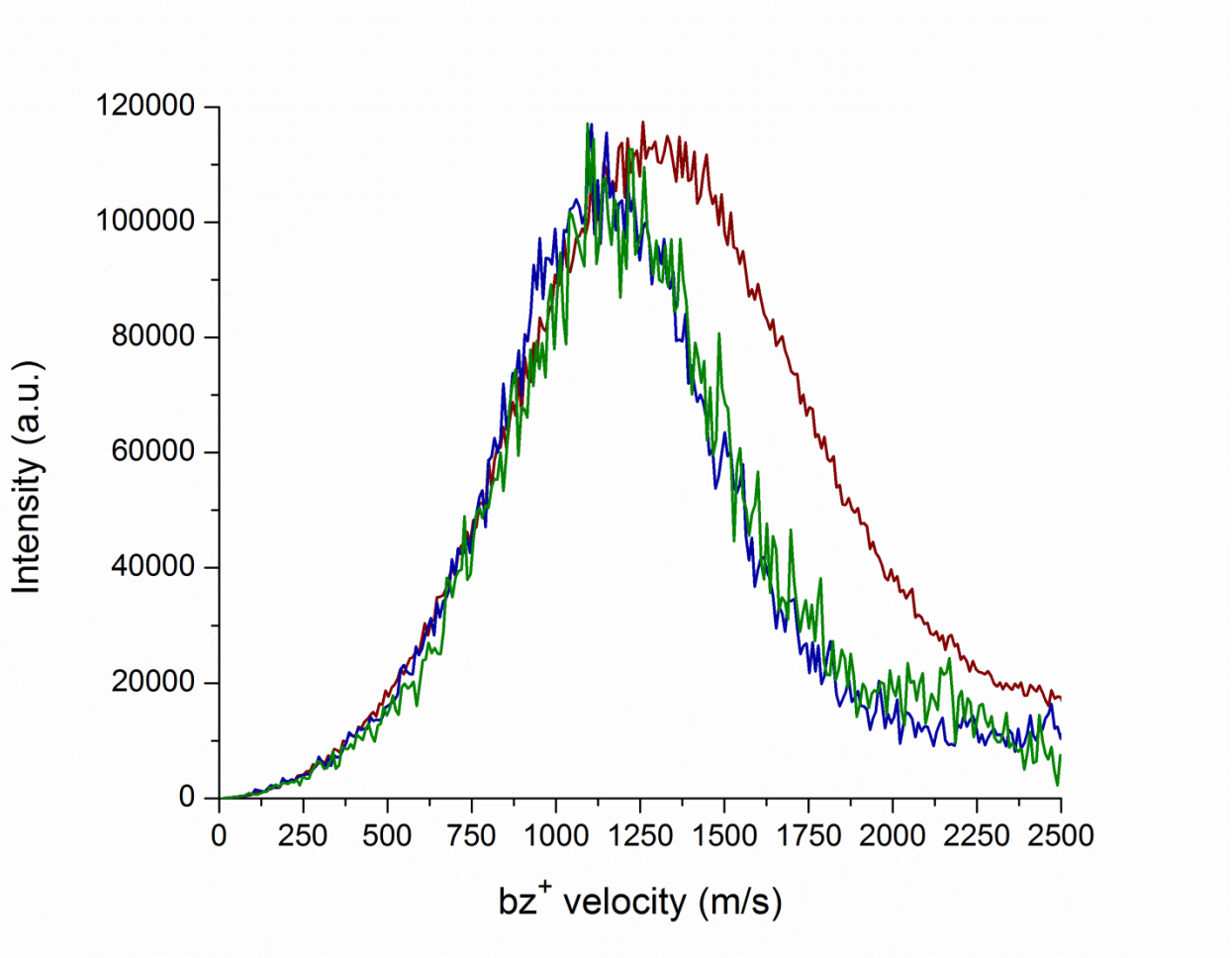

Figure 3.8. Velocity distributions of the benzene cation from photodissociation at 355 nm in helium (red), argon (blue), and CO_2 (green).

as an expansion gas resulted in a higher maximum kinetic energy release, showing that the ions have not been completely cooled. Using CO_2 as an expansion gas gave comparable results to argon, which suggests that the ions have been cooled as much as is feasible in our experiment. The estimated temperatures in our experiment are 30−50 K, whereas theory and Armentrout's work present values for ions at 0 K. This higher temperature can account for ~0.5 kcal/mol of energy, which would shift our upper limits on the dissociation energies slightly higher. Multiphoton processes could shift the KER values higher, however, careful power dependence studies have been conducted to ensure only single photon absorption. There are certain issues that might affect the CID results, such as large kinetic shifts in thresholds for such large ions, but Armentrout has addressed them as much as possible.[46] Finally, the use of DFT methods is common when using transition metals because of its feasibility to handle systems with many electrons, however, these methods are recognized as problematic for thermochemistry. Errors in these calculations as high as 5 kcal/mol are not uncommon, and there is no way to achieve more accurate results.[72-76] Our calculations do not include any spin-orbit or relativistic effects that could affect the energetics for silver complexes. It is also not feasible to use higher levels of theory such as CCSD(T), which have trouble running systems involving transition metals. Therefore, it is not possible to identify the exact source of the discrepancies in our results.

Conclusion

Dissociative charge transfer was found to be the prominent photodynamic process in Ag^+(benzene), Ag^+(toluene), and Ag^+(furan) to produce the organic cation as a photoproduct at the wavelengths investigated here. Photofragment imaging of the fragment ions provides evidence for significant kinetic energy release in each of these systems, as well as the excitation

of the rotational and vibrational degrees of freedom of the organic fragment. The amount of energy deposited into the internal degrees of freedom increases with increasing excitation energy, which is attributed to a more energetic kick off the excited state potential, Franck-Condon effects, or electronic state mixing between the neutral ligand and the charge transfer state. An energetic cycle using the maximum KER values was used to determine upper limits on the bond energies in these systems. The Ag^+(benzene) and Ag^+(toluene) limits are less than those predicted by theory. The results for Ag^+(furan) suggest that there is a significant amount of a more unstable isomer than the global minimum predicted by theory. Overall, these results provide new insights into the photodissociation dynamics on charge transfer excited states and the bonding thermochemistry of cation-π complexes.

References

1. Bagchi, B. Dynamics of Solvation and Charge Transfer Reactions in Dipolar Liquids. *Annu. Rev. Phys. Chem.* **1989**, *40*, 115−141.
2. Marcus, R. A. Electron Transfer Reactions in Chemistry: Theory and Experiment (Nobel Lecture). *Angew. Chem. Int. Ed.* **1993**, *32*, 1111–1121.
3. Barbara, P. F.; Meyer, T. J.; Ratner, M. A. Contemporary Issues in Electron Transfer Research. *J. Phys. Chem.* **1996**, *100*, 13148−13168.
4. Adams, D. M.; Brus, L.; Chidsey, C. E. D.; Creager, S.; Creutz, C.; Kagan, C. R.; Kamat, P. V.; Lieberman, M.; Lindsay, S.; Marcus, R. A.; Metzger, R. M.; Michel-Beyerle, M. E.; Miller, J. R.; Newton, M. D.; Rolison, D. R.; Sankey, O.; Schanze, K. S.; Yardley, J.; Zhu, X. Charge transfer on the Nanoscale: Current Status. *J. Phys. Chem. B* **2003**, *107*, 6668−6697.
5. Mulliken, R. S. Molecular Compounds and their Spectra. II *J. Am. Chem. Soc*.**1952**, *74*, 811−824.
6. Huhey, J. E.; Keiter, E. A.; Keiter, R. L. *Inorganic Chemistry*, 4th ed.; Harper Collins: New York, 1993.
7. Long, N. J. *Metallocenes*; Blackwell Science: Oxford, U.K., 1998.
8. Ardo, S.; Meyer, G. J. Photodriven Heterogeneous Charge Transfer with Transition-Metal Compounds Anchored to TiO_2 Semiconductor Surfaces. *Chem. Soc. Rev.* **2009**, *38*, 115−164.
9. Crabtree, R. H. *The Organometallic Chemistry of the Transition Metals*, 5th edition; John Wiley & Sons: Hoboken, NJ, 2009.
10. Hartwig, J. F. *Organotransition Metal Chemistry: From Bonding to Catalysis*; University Science Books: Sausalito, CA, 2010.

11. Park, H.; Kim, H.-I.; Moon, G.-H.; Choi, W. Photoinduced Charge Transfer Processes in Solar Photocatalysis Based on Modified TiO_2. *Energy Environ. Sci.* **2016**, *9*, 411−433.
12. Barragan, A. M.; Schulten, K.; Solovyov, I. A. Mechanism of the Primary Charge Transfer Reaction in the Cytochrome bc_1 Complex. *J. Phys. Chem. B* **2016**, *120*, 11369−11380.
13. Yam, V. W.-W.; Chan, A. K.-W.; Hong, E. Y.-H. Charge-Transfer Processes in Metal Complexes Enable Luminescence and Memory Functions. *Nature Reviews Chemistry* **2020**, *4*, 528–541.
14. Jarrold, M. F.; Misev, L.; Bowers, M. T. Charge Transfer Half-Collisions: Photodissociation of the $Kr{\cdot}O_2^+$ Cluster Ion with Resolution of the O_2 Product Vibrational States. *J. Chem. Phys.* **1984**, *81*, 4369–4379.
15. Illies, J. I.; Jarrold, M. F.; Wagner-Redeker, W.; Bowers, M. T. Photoinduced Intramolecular Charge Transfer: Photodissociation of $CO_2^+{\cdot}Ar$ Cluster Ions. *J. Am. Chem. Soc.* **1985**, *107*, 2842–2849.
16. Kim, H.-S.; Kuo, C.-H.; Bowers, M. T. Photon Driven Charge Transfer Half Collisions: The Photodissociation of $CO_2^+{\cdot}O_2$ Cluster Ions with Resolution of the O_2 Product Vibrational States. *J. Chem. Phys.* **1987**, *87*, 2667–2676.
17. Willey, K. F.; Cheng, P. Y.; Pearce, K. D.; Duncan, M. A. Photoinitiated Charge Transfer and Dissociation in Mass-Selected Metallo-Organic Complexes. *J. Phys. Chem***. 1990**, *94*, 4769−4772.
18. Willey, K. F.; Cheng, P. Y.; Bishop, M. B.; Duncan, M. A. Charge-Transfer Photochemistry in Ion-Molecule Cluster Complexes of Silver. *J. Am. Chem. Soc.* **1991**, *113*, 4721−4728.
19. Willey, K. F.; Yeh, C. S.; Robbins, D. L.; Duncan, M. A. Charge Transfer in the Photodissociation of Metal Ion-Benzene Complexes. *J. Phys. Chem.* **1992**, *96*, 9106−9111.

20. Jaeger, T. D.; Duncan, M. A. Photodissociation of $M^+(benzene)_x$ Complexes (M = Ti, V, Ni) at 355 nm. *Int. J. Mass Spectrom.* **2005**, *241*, 165−171.

21. Chen, J.; Wong, T. H.; Cheng, Y. C.; Montgomery, K.; Kleiber, P. D. Photodissociation Spectroscopy and Dynamics of $MgC_2H_4^+$. *J. Chem. Phys.* **1998**, *108*, 2285–2296.

22. Lu, W.-Y.; Wong, T.-H.; Kleiber, P. D. Photochemistry of $Zn^+(CH_4)$. Chem. Phys. Lett. **347**, 183 (2001).

23. Lu, W.-Y.; Kleiber, P. D.; Young, M. A. Photodissociation Spectroscopy of $Zn^+(C_2H_4)$. J. Chem. Phys. **115**, 5823 (2001).

24. Lu, W.-Y.; Wong, T.-H.; Sheng, Y.; Lytle, A. T.; Kleiber, P. D. Photodissociation Spectroscopy of Zn^+—Methanol. J. Phys. Chem. A **107**, 984 (2003).

25. Yang, Y.-S.; Yeh, C.-S. Photodissociative Charge Transfer in Ag^+-Pyridine Complex. *Chem. Phys. Lett.* **1999**, *305*, 395–400.

26. Yang, Y.-S.; Hsu, W.-Y.; Lee, H.-F.; Huang, Y.-C.; Yeh, C.-S. Experimental and Theoretical Studies of Metal Cation-Pyridine Complexes Containing Cu and Ag. *J. Phys. Chem. A* **1999**, *103*, 11287–11292.

27. Su, P. H.; Yeh, C. S. Photofragmentation of the Ag^+-Furan Complex in the Gas-Phase. *Chem. Phys. Lett.* **2000**, *331*, 420–424.

28. Su, P. H.; Lin, F. W.; Yeh, C. S. Photodissociation Studies of $M(Furan)^+$ (M = Cu, Ag, and Au) and $Au(C_3H_4)^+$ Complexes. *J. Phys. Chem. A* **2001**, *105*, 9643–9648.

29. Hsu, H.-C.; Lin, F.-W.; Lai, C.-C.; Su, P.-H.; Yeh, C.-S. Photodissociation and Theoretical Studies of the Au^+-(C_5H_5N) Complex. *New J. Chem.* **2002**, *26*, 481−484.

30. Maner, J. A.; Mauney, D. T.; Duncan, M. A. Imaging Charge Transfer in a Cation-π System: Velocity-Map Imaging of Ag^+(benzene) Photodissociation. *J. Phys. Chem. Lett.* **2015**, *6*, 4493–4498.

31. Dougherty, D. A. Cation-π Interactions in Chemistry and Biology: A New View of Benzene, Phe, Tyr, and Trp. *Science* **1996**, *271*, 163–168.

32. Ma, J. C.; Dougherty, D. A. The Cation-π Interaction. *Chem. Rev.* **1997**, *97*, 1303–1324.

33. Dougherty, D. A. The Cation-π Interaction. *Acc. Chem. Res.* **2012**, *46*, 885–893.

34. Mahadevi, A.S.; Sastry, G. N. Cation-π Interaction: Its Role and Relevance in Chemistry, Biology, and Material Science. *Chem. Rev.* **2012**, *113*, 2100–2138.

35. Hettich, R. L.; Jackson, T. C.; Stanko, E. M.; Freiser, B. S. Gas-Phase Photodissociation of Organometallic Ions. Bond Energy and Structure Determination. *J. Am. Chem. Soc.* **1986**, *108*, 5068−5093.

36. Eller, K.; Schwarz, H. Organometallic Chemistry in the Gas Phase**.** *Chem. Rev.* **1991**, *91*, 1121−1177.

37. Bauschlicher, C. W., Jr.; Partridge, H.; Langhoff, S. R. Theoretical Study of Transition-Metal Ions Bound to Benzene. *J. Phys. Chem.* **1992**, *96*, 3273−3278.

38. Chen, Y.-M.; Armentrout, P. B. Collision-Induced Dissociation of $Ag(C_6H_6)^+$. *Chem. Phys. Lett.* **1993**, *210*, 123−128.

39. Afzaal, S.; Freiser, B. S. Gas-phase Photodissociation Study of $Ag(benzene)^+$ and $Ag(toluene)^+$. *Chem. Phys. Lett.* **1994**, *218*, 254–260.

40. Meyer, F.; Khan, F. A.; Armentrout, P. B. Thermochemistry of Transition Metal Benzene Complexes: Binding Energies of $M(C_6H_6)_x^+$ (x = 1, 2) for M = Ti to Cu. *J. Am. Chem. Soc.* **1995**, *117*, 9740−9748.

41. Yasuike, T.; Nakajima, A.; Yabushita, S.; Kaya, K. Why Do Vanadium Atoms Form Multiple-Decker Sandwich Clusters with Benzene Molecules Efficiently? *J. Phys. Chem. A* **1997**, *101*, 5360−5367.

42. Schroeter, K.; Wesendrup, R.; Schwarz, H. Substituent Effects on the Bond-Dissociation Energies of Cationic Arene-Transition-Metal Complexes. *Eur. J. Org. Chem.* **1998**, 565–571.

43. Dargel, T. K.; Hertwig, R. H.; Koch, W. How Do Coinage Metal Ions Bind to Benzene? *Molec. Phys*. **1999**, *96*, 583−591.

44. Nakajima, A.; Kaya, K. A Novel Network Structure of Organometallic Clusters in the Gas Phase. *J. Phys. Chem. A* **2000**, *104*, 176−191.

45. Duncan, M. A. Structures, Energies and Spectroscopy of Gas Phase Transition Metal-Benzene Complexes. *Int. J. Mass Spectrom*. **2008**, *272*, 99−118.

46. Rodgers, M. T.; Armentrout, P. B. Cationic Noncovalent Interactions: Energetics and Periodic Trends. *Chem. Rev.* **2016**, *116*, 5642–5687.

47. Reddic, J. E.; Robinson, J. C.; Duncan, M. A. Growth and Photodissociation of Ag_x-C_{60} Cation Complexes. *Chem. Phys. Lett*. **1997**, *279*, 203–208.

48. Buchanan, J. W.; Grieves, G. A.; Flynn, N. D.; Duncan, M. A. Photodissociation of Silver-Coronene Cluster Cations. *Int. J. Mass Spectrom*. **1999**, *185/186/187*, 617−624.

49. Yeh, C. S.; Pilgrim, J. S.; Robbins, D. L.; Willey, K. F.; Duncan, M. A. Spectroscopy of Weakly-Bound Magnesium Ion Complexes. *Int. Rev. Phys. Chem.* **1994**, *13*, 231−262.

50. Lessen, D.; Asher, R. L.; Brucat, P. J. Spectroscopic Characterization of Inductive Binding in Ions. *Int. J. Mass Spectrom. Ion Processes* **1990**, *102*, 331−351.

51. Sanekata, M.; Misaizu, F.; Fuke, K.; Iwata, S.; Hashimoto, K. Reactions of Singly Charged Alkaline Earth Metal Ions with Water Clusters: Characteristic Size Distribution of Product Ions. *J. Am. Chem. Soc.* **1995**, *117*, 747–754.

52. Duncan, M. A. Spectroscopy of Metal Ion Complexes: Gas Phase Models for Solvation. *Annu. Rev. Phys. Chem.* **1997**, *48*, 69–93.

53. Duncan, M. A. Frontiers in the Spectroscopy of Mass-Selected Molecular Ions. *Int. J. of Mass Spectrom.* **2000**, *200*, 545–569.

54. Farrar, J. M. Size-Dependent Reactivity in Open Shell Metal-Ion Polar Solvent Clusters: Spectroscopic Probes of Electronic-Vibration Coupling, Oxidation and Ionization. *Int. Rev. Phys. Chem.* **2003**, *22*, 593–640.

55. Metz, R. B. Photofragment Spectroscopy of Covalently Bound Transition Metal Complexes: A Window into C-H and C-C Bond Activation by Transition Metal Ions. *Int. Rev. Phys. Chem.* **2004**, *23*, 79–108.

56. Lias, S. G. "Ionization Energy Evaluation" in NIST Chemistry WebBook, NIST Standard Reference Database Number 69, Eds. P. J. Linstrom and W.G. Mallard, National Institute of Standards and Technology, Gaithersburg, MD, 20899, https://doi.org/10.18434/T4D303, (accessed Apr. 5, 2022).

57. Kramida, A., Ralchenko, Yu., Reader, J. and NIST ASD Team (2019). *NIST Atomic Spectra Database* (version 5.7.1), National Institute of Standards and Technology, Gaithersburg, MD, https://physics.nist.gov/asd, (accessed Apr. 5, 2022).

58. Parmenter, C. S. Radiative and Non-Radiative Processes in Benzene. *Adv. Chem. Phys.* **1972**, *22*, 365–421.

59. Hopkins, J. B.; Powers, D. E.; Smalley, R. E. Vibrational Relaxation in Jet-Cooled Alkyl Benzenes. I. Absorption Spectra. *J. Chem. Phys.* **1980**, *72*, 5039–5048.

60. Christiansen, O.; Jørgensen, P. The Electronic Spectrum of Furan. *J. Am. Chem. Soc.* **1998**, *120*, 3423–3430.

61. Duncan, M. A. Laser Vaporization Cluster Sources. *Rev. Sci. Instrum.* **2012**, *83*, 041101.

62. Townsend, D.; Minitti, M. P.; Suits, A. G. Direct Current Slice Imaging. *Rev. Sci. Instrum.* **2003**, *74*, 2530–2539.

63. Li, W.; Chambreau, S. D.; Lahankar, S. A.; Suits, A. G. Megapixel Ion Imaging with Standard Video. *Rev. Sci. Instrum.* **2005**, *76*, 063106. See also NuAcq 0.9 software: Suits, A.G., http://faculty.missouri.edu/suitsa/NuAcq.html.

64. Dribinski, V.; Ossadtchi, A.; Mandelshtam, V. A.; Reisler, H. Reconstruction of Abel-Transformable Images: the Gaussian Basis-set expansion Abel Transform Method," *Rev. Sci. Instrum.* **2002**, *73*, 2634-2642.

65. Frisch, M. J.; Trucks, G. W.; Schlegel, H. B.; Scuseria, G. E.; Robb, M. A.; Cheeseman, J. R.; Scalmani, G.; Barone, V.; Peterson, G. A.; Nakatsuji, H. et al. *Gaussian16*, Gaussian, Inc.; Wallingford, CT, **2009**.

66. Ridley, T.; Lawley, K. P.; Al-Kahali, M. H.S.N.; Donovan, R. J. Determination of the First Ionization Energy of Furan (C_4H_4O) from an Extrapolation of Two *n*d Rydberg Series Observed in the Mass-Resolved (2+1) Resonance Enhanced Multiphoton Ionization Spectrum. *Chem. Phys. Lett.* **2004**, *390*, 376–379.

67. Chewter, L. A.; Sander, M.; Müller-Dethlefs, K.; Schlag, E. W. High Resolution Zero Kinetic Energy Photoelectron Spectroscopy of Benzene and Determination of the Ionization Potential. *J. Chem. Phys.* **1987**, *86*, 4737–4744.

68. Lu, K.-T.; Elden, G. C.; Weisshaar, J. C. Toluene Cation: Nearly Free Rotation of the Methyl Group. *J. Phys. Chem.* **1992**, *96*, 9742–9748.

69. Wheeler, S. E. Understanding Substituent Effects in Noncovalent Interactions Involving Aromatic Rings. *Acc. Chem. Res.* **2013**, *46*, 1029–1038.

70. Wheeler, S. E.; Bloom, J. W. G. Toward a More Complete Understanding of Non-Covalent Interactions Involving Aromatic Rings. *J. Phys. Chem. A* **2014**, *118*, 6133–6147.

71. Duncan, M. A. Infrared Laser Spectroscopy of Mass-Selected Carbocations. *J. Phys. Chem. A* **2012**, *116*, 11477–11491.

72. Harvey, J. N. DFT Computation of Relative Spin-State Energetics of Transition Metal Compounds. *Structure and Bonding.* **2004**, *112*, 151−184.

73. Cramer, C. J.; Truhlar, D. J. Density Functional Theory for Transition Metals and Transition Metal Chemistry. *Phys. Chem. Chem. Phys.* **2009**, *11*, 10757−10816.

74. Cohen, A. J.; Mori-Sanchez, P.; Yang, W. Challenges for Density Functional Theory. *Chem. Rev.* **2012**, *112*, 289–320.

75. Shil, S.; Bhattacharya, D.; Sarkar, S.; Misra, A. Performance of the Widely Used Minnesota Density Functionals for the Prediction of Heat of Formations, Ionization Potentials of Some Benchmarked First Row Transition Metal Complexes. *J. Phys. Chem. A* **2013**, *117*, 4945–4955.

76. Moltved, K. A.; Kepp, K. P. Chemical Bond Energies of 3d Transition Metals Studied by Density Functional Theory. *J. Chem. Theory Comput.* **2018**, *14*, 3479−3492.

CHAPTER 4

CHARGE TRANSFER IN ZINC-METHANOL CATION STUDIED WITH VELOCITY MAP IMAGING

Introduction

Metal ion-ligand interactions form the basis for solvation which is ubiquitous in many areas of chemistry, such as catalysis, aerosols, biochemistry, and the industrial manufacturing of organic substances.[1-5] Much of condensed-phase inorganic chemistry and catalysis takes place in solution with solvated metal atoms in various oxidation states driving reactions.[4] Metal ion cofactors are often found to be required for biochemical processes like protein folding or cell signaling.[5] Many of these systems are dominated by the electrostatic interactions between a metal ion and its solvating medium. However, detailed pictures of these interactions are difficult because of the difficulties between experiment and theory to study the same systems in the same environment. In this study, we investigate the strength of the interactions between zinc cation and methanol using velocity-map imaging (VMI).

The solvation of metal cations in the gas phase has been studied previously with mass spectrometry based techniques,[11-25] UV-vis and infrared spectroscopies,[16-39] and corresponding computational studies.[40-49] Most of the work has looked at the solvation of ions with water, but several of these studies have looked at the interactions of metal cation—methanol complexes. Farrar and co-workers looked at the visible photodissociation of $Sr^+(CH_3OH)$ and $Sr^+(CH_3OD)$ leading to the dissociation products Sr^+, $SrOH^+$, and $SrOD^+$.[27] A reaction yield of ~90% was observed for the higher energy $5p\pi$—$5s\sigma$ transition centered on Sr^+, while the lower vibrationally

resolved 4d—5s transition showed an anticorrelation between the vibrational resonances and the reaction products $SrOH^+$ and $SrOD^+$.

Our group has studied the photodissociation of $Mg^+(CH_3OH)_n$ (n = 1 — 6), looking at the spectroscopy of the monomer and the fragmentation of larger clusters at selected wavelengths.[26,28] The major fragmentation channels for the monomer were solvent elimination to produce Mg^+ and an excited state reaction producing $MgOH^+$, along with a small amount of MgO^+ and CH_3^+. Similar fragmentation was seen in the larger clusters ($1 < n < 6$) with Mg^+ and $MgOH^+$ solvated with different numbers of CH_3OH molecules. The fragmentation efficiency for clusters larger than n = 5 quickly died off, suggesting that an intracluster reaction had taken place producing Mg^{+2} coordinated with an anion, OH^- or CH_3O^-. This onset of a solvation induced intracluster reaction was different from that observed by Lu and Yang[13] who observed a reaction channel at n = 5 and Stace and co-workers[12] who saw it at n = 3. These other studies took place with a "pick-up" cluster source, so it is likely the reaction is sensitive the temperatures in the different cluster sources.

There have also been several studies looking at the solvation of zinc cation.[22-24,29-32,34,38,39] Previous work from our group[38] and that of Beyer and co-workers[39] studied the IR photodissociation spectroscopy of $Zn^+(H_2O)_n$ and found Zn^+ to have a coordination number of 3. While a collision induced dissociation (CID) study by Armentrout and co-workers found a coordination number of 5 for doubly-charged $Zn^{2+}(H_2O)_n$.[22] Kleiber and co-workers have studied the UV photodissociation spectroscopy of several Zn^+L complexes, where L = H_2O, CH_4, C_2H_4, H_2CO, and CH_3OH.[29-32,34] In their study of $Zn^+(CH_3OH)$,[34] the Kleiber group found that the main dissociation channel was for the formation of the charge transfer product, CH_3OH^+, which is markedly different than results of $Mg^+(CH_3OH)$ studies even though both complexes have very

similar electronic valence character. The charge transfer state in $Zn^+(CH_3OH)$ is accessible because of the relatively low difference in ionization potentials between Zn (9.39 eV)[50] and CH_3OH (10.84 eV)[51], $\Delta IP = 1.45$ eV, as compared to that of Mg[51] (7.64 eV) and CH_3OH, $\Delta IP = 3.20$ eV. The smaller ΔIP results in a low lying excited state that asymptotes to the *neutral* metal atom and *cationic* molecular fragment.

Photoinduced charge transfer has been observed previously in several photodissociation experiments on both atmospheric ion-molecule clusters[52-54] and transition metal ion-molecule complexes.[55-64] In some cases, the excitation spectra of the complexes were recorded and the threshold for dissociative charge transfer (DCT) were documented by the appearance of the organic fragment ion. Using the threshold observed and the difference of the known ionization potentials of the photodissociation fragments, an upper limit on the dissociation energy of the complex could be calculated via the expression:

$$D_0''(A^+{-}B) \leq h\nu_0 - \Delta IP$$

where D_0'' is the complex bond energy, $h\nu_0$ is the threshold photon energy, and ΔIP is the ionization potential difference between the two fragments. In recent work, our group has utilized VMI to measure the kinetic energy release following the DCT process,[65-67] where a similar energetic cycle can be used to determine an upper limit on the bond energy using the kinetic released:

$$D_0''(A^+{-}B) \leq h\nu_{CT} - (KER + \Delta IP)$$

where $h\nu_{CT}$ is the photodissociation energy, KER is the measured kinetic energy release, and ΔIP is the difference in ionization potentials. Here we use this approach to investigate the binding energy and photodissociation dynamics in $Zn^+(CH_3OH)$.

Methods

Experimental

Ions were produced via laser vaporization at 355 nm (SureLite SL-10 Nd:YAG laser) of a zinc rod in the so-called "offset" source configuration. Complexes were formed and cooled in a supersonic expansion of argon seeded with methanol from its ambient vapor pressure above liquid samples at room temperature.[68,69] Ions were skimmed and extracted orthogonally into a reflectron time-of-flight mass spectrometer, and mass selection occurs using a pair of pulsed deflection plates for photodissociation in the reflectron. The instrument is designed for mass analyzing dissociation products in the reflected ion beam or to allow transmission of the ion beam to detect kinetic energy release using the velocity map imaging (VMI) technique. The fragmentation laser used for either photodissociation experiments or for imaging experiments is either a Nd:YAG (Spectra Physics GCR-170) or a Nd:YAG pumped dye laser (Spectra Physics PDL-2). The apparatus for selected-ion velocity map imaging (SI-VMI) has been described previously.[65-67] Briefly, for VMI, the reflectron is grounded to allow transmission of ions into the collinear VMI flight tube, where they are decelerated into the photoexcitation region. Ions produced after photodissociation are then reaccelerated with an assembly of electrostatic lenses designed for VMI and detected using a dual MCP/P-47 phosphor detector (Beam Imaging Solutions BOS-75). The DC-slice imaging technique is used to detect only the central ~90 ns "slice" of the expanding Newton sphere of ions.[70] The slicing is achieved by activating the detector with a narrow time window using a fast rise-time high voltage pulser (DEI PVX-4140). This method throws a majority of the signal away, but allows for the determination of kinetic energy release and angular distribution without extensive processing of the image. A CCD camera (Edmund Optics) is used to collect the images over several hundred thousand laser shots,

and a photomultiplier tube observes the phosphor screen to detect time-of-flight information and monitor intensities. The images are processed using the NuAcq and BasisFit software of Suits.[70]

This SI-VMI is similar to other experiments for photofragment imaging of mass-selected ions recently reported, but it also has its unique features.[71-78] Ions are generated directly in the laser vaporization process, not with photoionization, and undergo cooling in the supersonic expansion. Argon is used for the expansion instead of helium to promote better cooling of the ions. Ions generated under similar conditions have been shown to have rotational temperatures in the 10–50 K range. The flight path from the ion extraction region to the imaging detector is 3 m, with 1.5 m from the photodissociation point to the detector. The ions are extracted perpendicularly to the molecular beam direction, but fly a colinear path through the time-of-flight spectrometer for mass selection before entering the imaging flight tube. Extraction energies can be adjusted to vary ion beam energy to optimize spatial filling of the detector with the ion image. The photodissociation of Ar_2^+, which has a well-known binding energy, was used to calibrate the instrument under the same ion beam conditions.[66] Analysis of the images of Ar^+ show that the instrument has no VMI lens-induced image expansion under the current ion beam conditions.[67,79] The imaged ions are not state selected as they are in other imaging experiments,[79] so the detected ions are representative of a distribution of species in all internal states populated in the photodissociation process and the resultant image provides an overview of the dynamics.

Computational

Computations employed density functional theory (DFT) and equation-of-motion coupled cluster (EOM-CC) methods as employed in the Gaussian16 software. Geometry optimizations were carried out using the B3LYP, M06L, and MN15L functionals with the def2TZVP and def2-

QZVP basis sets. Frequency calculations were also done at these same levels to correct for zero-point energy in the bond energies calculated. The reported bond energies have also been corrected for basis set superposition error. Excited state calculations were done using EOM-CCSD with the def2-TZVP basis set.[80]

Results and Discussion

Laser vaporization of a zinc rod in an expansion of argon seeded with methanol produces a distribution of ions of the form $Zn^+(CH_3OH)_n$ out to approximately $n = 10$. The conditions for generating ions in the laser vaporization source are gentle and lead to the addition of intact molecules to the metal ion; there is little evidence for fragmentation of the methanol. A photodissociation mass spectrum for $Zn^+(CH_3OH)$ at 266 nm is shown in Figure 4.1. This is a difference spectrum obtained from subtracting the selected parent ion intensity from the diminished parent and fragment ion intensities produced after excitation. The mass spectrum both with and without the fragmentation laser were averaged before subtraction. This difference mode of operation makes the parent ion depletion appear as a negative peak and the fragment ions appear as positive peaks. The fragment ions produced in this experiment were Zn^+ and the charge transfer product, CH_3OH^+. We do not see the CH_3^+ fragment ion. Laser-power dependence studies were carried out to ensure only single photon processes.

To investigate the structure and energetics of the $Zn^+(CH_3OH)$ complex, computations were carried out using the B3LYP, M06L, and MN15L funtionals with both the def2-TZVP and def2-QZVP basis sets. The optimized structures can be found in Appendix B. In each case, the predicted structure has the zinc binding to the alcohol atom. The predicted dissociation energies at each level of theory can be seen in Table 4.1, and they range between 37.26 and 38.23

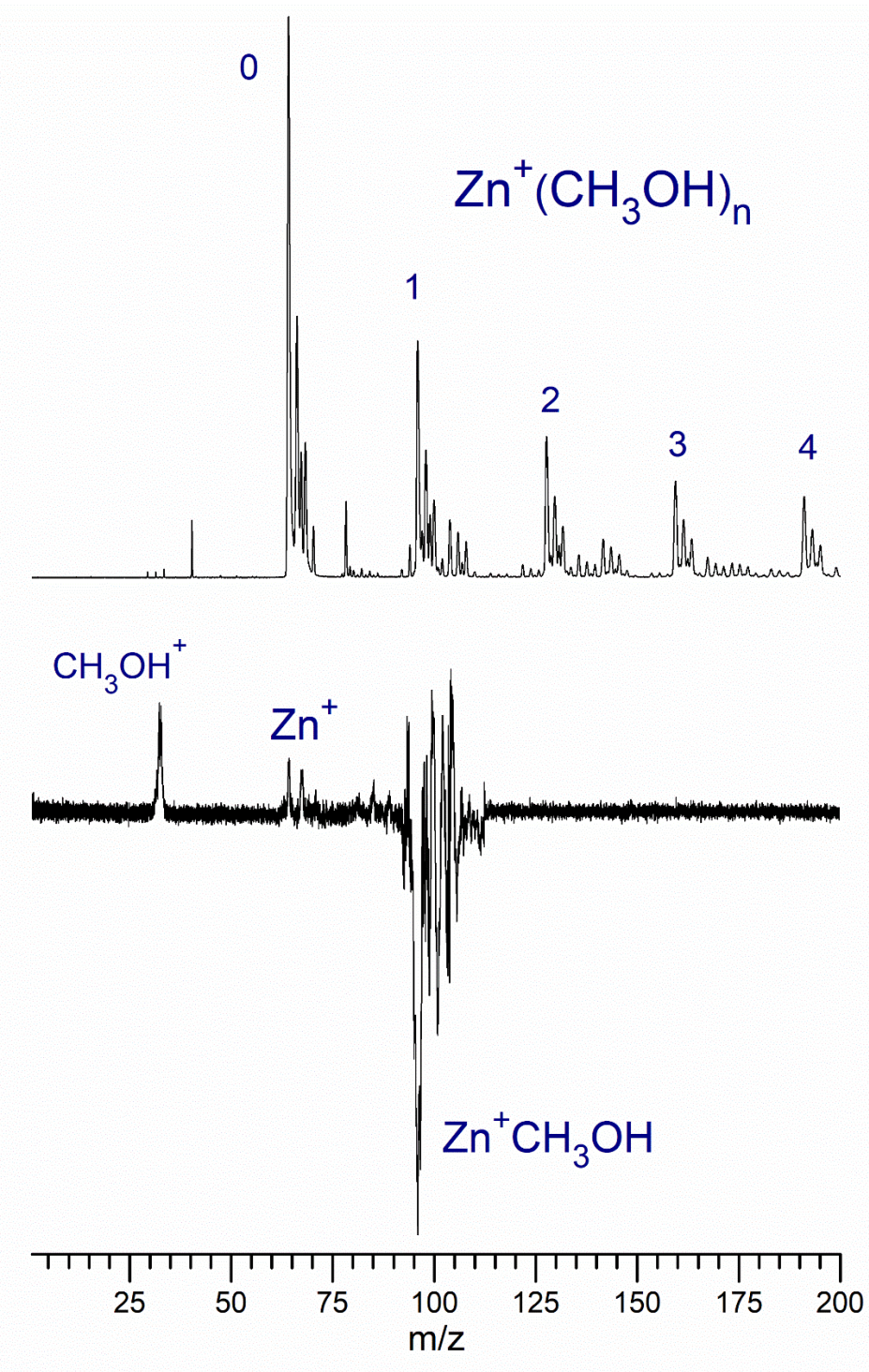

Figure 4.1. Mass spectrum (top) and 266 nm photodissociation mass spectrum of $Zn^+(CH_3OH)$.

Table 4.1. Bond dissociation energies (kcal/mol; ZPE Corrected) for $Zn^+(CH_3OH)$ and $Zn^+(CD_3OD)$ resulting from our computations, compared to the upper limits derived here and to the results of previous theory. Included is the relative energy in eV (kcal/mol in parenthesis) of the Zn insertion complex, CH_3-Zn-OH^+, coompared to $Zn^+(CH_3OH)$ at the same level.

		$Zn^+(CH_3OH)$	$Zn^+(CD_3OD)$	CH_3-Zn-OH^+
B3LYP	def2-TZVP	37.56	37.71	1.31(30.22)
	def2-QZVP	38.17	38.31	1.25(28.76)
M06L	def2-TZVP	37.27	37.37	0.99(22.82)
	def2-QZVP	38.23	38.33	0.93(21.52)
MN15L	def2-TZVP	37.26	37.41	–
	def2-TZVP	37.55	37.69	–
This experiment		39.66 ± 4.15[a]	36.44 ± 4.15[a]	1.81(41.74)[d]
		33.42 ± 4.15[b]		1.44(33.21)[f]
		31.13 ± 4.15[c]		
		33.25[d]		
		38.10[e]		
		38.511[f]		

[a]present experiment; CH_3OH^+ (CD_3OD^+) image at 266 nm
[b]present experiment; CH_3OH^+ image at 280 nm
[c]present experiment; Zn^+ image at 266 nm; assuming a two photon process
[c]HF theory (ref. 31)
[d]MP2 theory (ref. 31)
[e]B3LYP theory (ref. 31)

kcal/mol, depending on the level. The dissociation energies for the deuterated zinc-methanol cation, $Zn^+(CD_3OD)$, were also computed and have a predicted binding energy ~ 0.10 – 0.15 kcal/mol above that of the non-deuterated cation at the same level after correcting for zero point vibrational energy. The relative energies of a zinc insertion complex, CH_3-Zn-OH^+, were also calculated, since insertion has been previously observed in the iron-methanol complex.[80] The insertion complex has a relative energy ~ 1.0 − 1.3 eV higher than the ground state minimum. These values are lower than those predicted previously of 1.81 and 1.44 eV,[31] however, we do not see any evidence for the formation of this complex based on our photodissociation mass spectrum.

As discussed previously, a dissociative charge transfer transition is understandable in this system because there are no low-lying excited states of the methanol ligand and the difference in the ionization potentials of Zn and methanol is lower than the lowest excited state of the zinc cation. Potential energy curves of ground state $Zn^+(CH_3OH)$ and the four lowest excited states are shown in Figure 4.2, and were calculated at the EOM-CCSD/def2-TZVP level of theory. The optimized geometry of the $Zn^+(CH_3OH)$ complex has the zinc cation binding to methanol through its oxygen atom. The energies of four electronic states were also calculated, three involving the Zn^+ $4s^1 \rightarrow 4p^1$ transition and one that is the charge transfer state producing CH_3OH^+, and three of these were found to be accessible under the energies used in this experiment (266 nm (4.66 eV) and 280 nm (4.43 eV)).[51] The lowest energy transition predicted was the charge transfer corresponding to Zn $4s^2$ and CH_3OH^+ at 293.0 nm. Two higher excited states corresponding to Zn^+ atomic transitions were predicted to have transition energies of 286.2 nm and 268.9 nm which are the transitions into the Zn^+ $4p_y$ and $4p_x$ orbitals, respectively. The highest energy transition predicted at 234.1 nm is the Zn^+ $4s^1 \rightarrow 4p_z^1$ transition, which involves

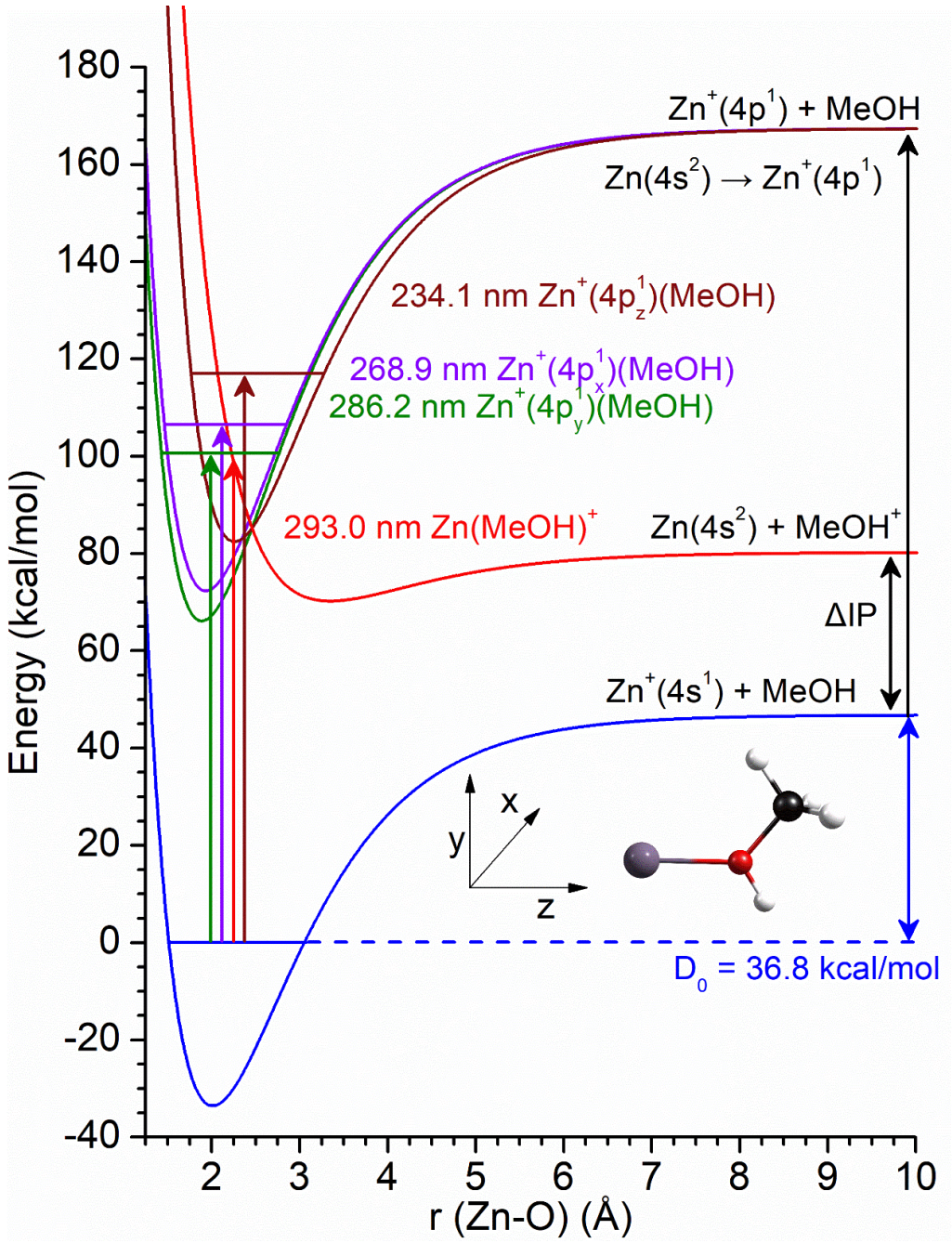

Figure 4.2. Potential energy surface of ground state and four lowest electronic excited states of $Zn^{+}(CH_3OH)$ at the EOM-CCSD/Def2TZVP level of theory.

moving an electron into an orbital parallel with the Zn–oxygen bond, thus driving the excitation energy up.

Figure 4.3 shows images of the methanol cation photofragment from excitation at 266 (top) and 280 (middle) nm and the zinc cation (bottom) photofragment from excitation at 266 nm, with the polarization of the fragmentation laser set to be parallel to the face of the detector. The left side of Figure 4.3 shows the raw images of the photofragments without any processing, and the right shows the total kinetic energy release obtained from analyzing the raw images. As can be seen from the kinetic energy release spectra, there is a broad range of fragment ions produced with varying amounts of translational energy. This indicates that some of the excess energy has been transferred into the rotational and/or vibrational degrees of freedom of the methanol fragment regardless of which fragment ion is being imaged. The majority of the signal lies above 0.5 eV which suggests that most of the fragment ions have been produced with some significant amount of kinetic energy. As can be seen by the raw images, the signal is isotropic in nature. Fitting the angular distribution of the images gives β parameters of -0.04 – 0.18. This isotropic distribution could be due to dissociation taking place over a longer time frame than a molecular rotation, which could send fragments moving in any direction as the complex rotates, regardless of laser polarization. However, because of the asymmetry of the complex, the dissociation axis may not align well with the transition dipole moment and this would result in an isotropic image.

The maximum kinetic energy release values determined from these images are shown in Table 4.2, and more detailed KER spectra including error bars can be found in Appendix B. Dissociation of $Zn^{+}(CH_3OH)$ at 266 and 280 nm gave maximum kinetic energy release values of 1.49 and 1.52 eV, respectively, when imaging the methanol cation fragment. This result is

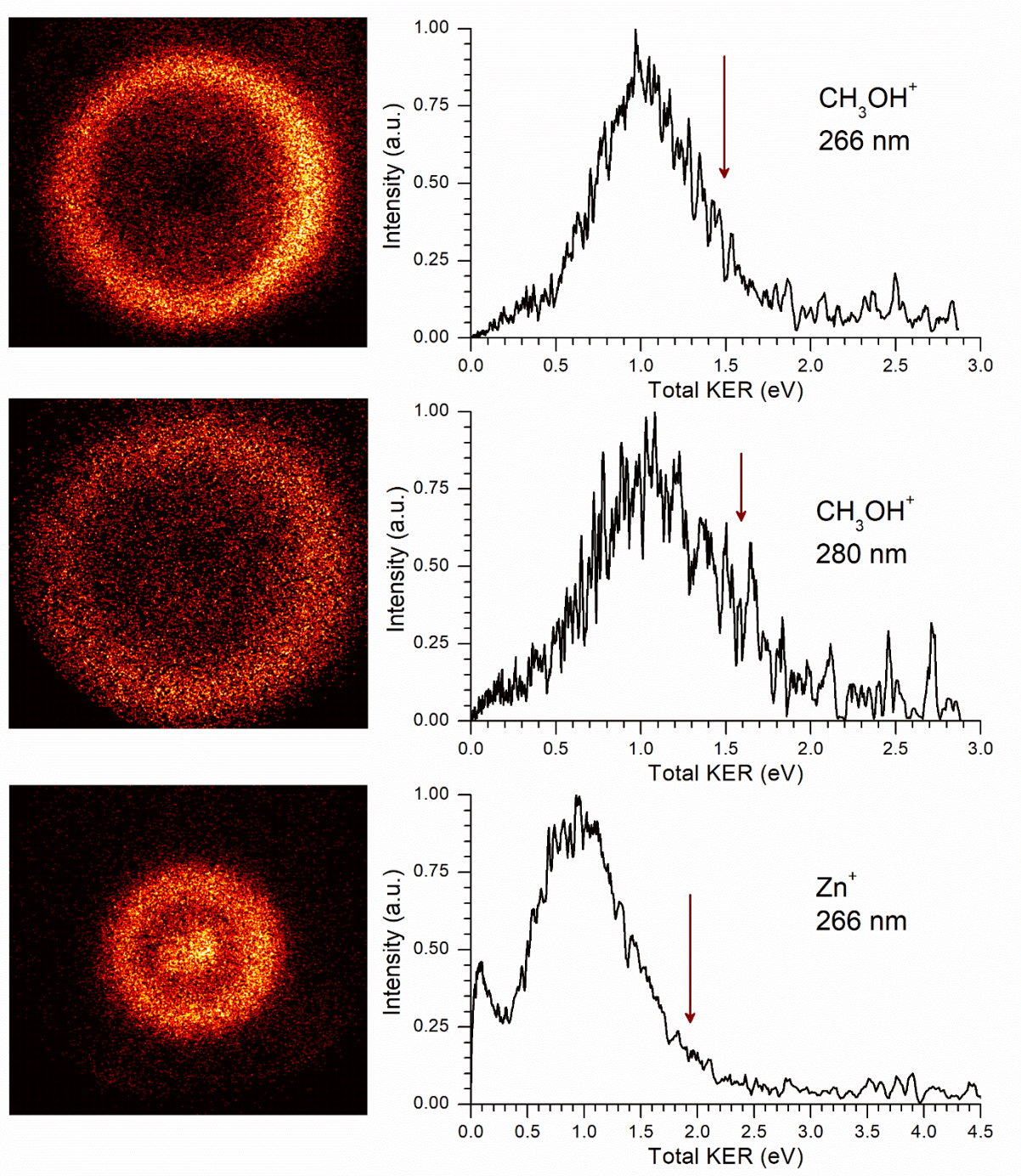

Figure 4.3. Raw images from $Zn^+(CH_3OH)$ photodissociation recording the CH_3OH^+ fragment at 266 nm (top) and 280 nm (middle) and the Zn^+ fragment at 266 nm (bottom). The resulting kinetic energy release distribution are shown to the right. Red arrows indicate the maximum kinetic energy release determined.

unexpected, since dissociation at a longer wavelength should produce less kinetic energy release. However, in our previous experiments on silver cation-aromatic complexes, the images indicated that excitation at a higher energy produced fragment ions with more energy deposited into the internal degrees of freedom of the ion and less into translational energy. This may be one explanation as to why there is less kinetic energy release here at 266 nm. The image from 280 nm dissociation is also much less intense than the 266 nm one, even though it was acquired over a much longer time scale. As a result, there is also much more noise, which might skew our results slightly towards higher KER. However, it is doubtful that this would skew the result by more than the difference in energy of the two dissociating wavelengths (0.24 eV). The tightest value for the upper limit on the dissociation energy given by these two values is 33.42 ± 4.15 kcal/mol at 280 nm. This value compares to our computed values for the bond energy of 37−39 kcal/mol, which varies depending on functional and basis set. The upper limit derived here agrees with that predicted by our theory and the theory reported by Kleiber and coworkers[31] considering the errors between the experiment and computations.

The image of the zinc cation fragment, shown in Figure 4.3, gives a maximum kinetic energy release value of 1.96 ± 0.18 eV. The $^2P_{1/2} \leftarrow {}^2S_{1/2}$ atomic transition of zinc cation is at dissociation energy could be determined by subtracting the kinetic energy release from the input photon energy, if the zinc cation fragment is in its ground state. However, this gives an upper limit on the dissociation energy of 62.26 ± 4.15 kcal/mol, which is much higher than predicted by theory and derived from the other images. Even though laser power was kept to a minimum (~1 mJ/pulse), there is the possibility of multiphoton excitation. The symmetry of the lowest bound state (^{2}A') transition predicted to be at 286.2 nm (Figure 4.2) matches the symmetry in the ground state. It is possible that we could be exciting this transition, followed by absorption of

Table 4.2. Max kinetic energy release values determined from the images.

Fragment Imaged	Dissociation Wavelength	Max KER (eV)
CH_3OH^+	266 nm	1.49 ± 0.18
CH_3OH^+	280 nm	1.52 ± 0.18
Zn^+	266 nm	1.96 ± 0.18
CD_3OD^+	266 nm	1.60 ± 0.18

another photon which leads to dissociation. This would impart 9.32 eV worth of energy into the zinc-methanol cation. A modification of the energetic cycle discussed previously allows for the derivation of an upper limit on the dissociation energy, assuming two-photon absorption into a different electronic state.

$$D_0''(A^+{-}B) \leq 2h\nu - (KER + E^2P{\leftarrow}^2S)$$

Where $E^2P{\leftarrow}^2S$ is the energy of the Zn^+ $4p^1{\leftarrow}4s^1$ transition (6.01 eV), since these are the asymptotic limits between the ground and bound excited states. Using this energetic cycle leads to an upper limit on the dissociation energy of 31.13 ± 4.15 kcal/mol. This value compares much better to the other values, however, it is lower. There is also that possibility that the excited state fluoresces back down to the ground state before dissociation. If this were the case, we have no way of knowing how much energy was lost to fluorescence in this experiment, thus no way to apply an energetic cycle to place an upper bound on the dissociation energy.

We also looked at the dissociative charge transfer of $Zn^+(CD_3OD)$ at 266 nm to study the effects of deuteration on the kinetic energy release. The image of CD_3OD^+ is shown in Figure 4.4, along with the image of CH_3OH^+ at 266 nm discussed previously. Again, the velocity distribution is broad, suggesting a significant amount of excitation of the rotational and/or vibrational states of the CD_3OD^+ fragment. The majority of the signal lies above 0.5 eV, which shows that even the most internally excited fragments are produced with a significant amount of kinetic energy. The maximum kinetic energy determined from the image is 1.60 ± 0.18 eV. This leads to an upper limit on the dissociation energy of 36.44 ± 4.15 kcal/mol. This compares to our computed values of between 37−39 kcal/mol, which varies depending on functional and basis set. The derived value is slightly lower than that predicted by theory, although not by as much as the value for the undeuterated complex. Because of zero point vibrational energy, deuterated

zinc-methanol cation is expected to have a slightly higher binding energy. This is reflected in our predicted bond energies, where $Zn^+(CD_3OD)$ is calculated to be more strongly bound than $Zn^+(CH_3OH)$ by about 0.15 kcal/mol. Our derived upper limit for deuterated zinc-methanol cation *is* higher than that derived from $Zn^+(CH_3OH)$, although by about 3 kcal/mol.

To the best of our knowledge, these are the first experimentally reported values for an upper limit on the dissociation of $Zn^+(CH_3OH)$ and its deuterated complex. Therefore, there are no other values for us to compare to other than theory. Because of this, and our relatively wide error bars, we have carefully considered any possible sources of error in the experiment. If the ions were not cooled completely and had unquenched internal energy, there may be a higher kinetic energy release than there should be due to ions in excited ro-vibrational states. This would lead to a lower value for the limit on the dissociation energy. We have tested this with photofragment imaging of the silver-benzene cation in different expansion gases (He, Ar, and CO_2), as reported previously. Helium did produce a KER spectrum with a higher kinetic energy release, but argon and CO_2 gave similar results. This indicates that we have cooled the ions as much as possible expanding in argon. It is estimated that the ions in our experiment are at a temperature between 30 − 50 K. This would account for about 0.5 kcal/mol of energy and would raise our values for the upper limits. There is also the potential of multiphoton excitation, which could raise the amount of KER seen from the charge transfer state, and lower the upper limit on the bond energy. We have tried to be as careful as possible to eliminate the chance of multiphoton effects, but it seems this may be a possible explanation for the result seen in the Zn^+ fragment image. Our tightest limit on the bond energy in this system is 33.42 ± 4.15 kcal/mol from the CH_3OH^+ image at the 280 nm wavelength. The zinc cation image does give a lower

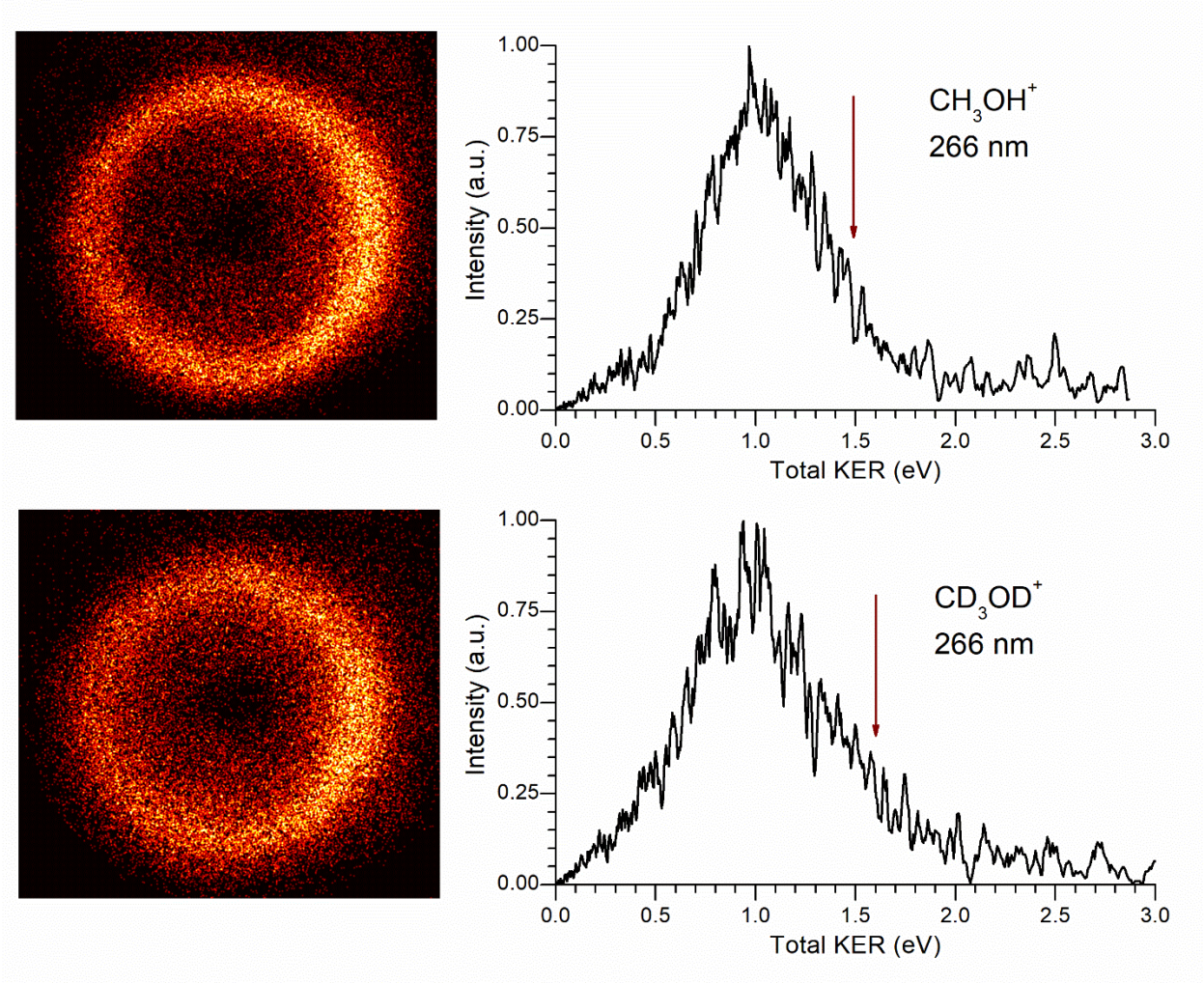

Figure 4.4. Raw images recording the CH_3OH^+ and CD_3OD^+ fragments from photodissociation of $Zn^+(CH_3OH)$ & $Zn^+(CD_3OD)$.

limit at 31.13 ± 4.15 kcal/mol, however it is uncertain if this value is actually a product of a multiphoton process or not. The 33.42 kcal/mol value does agree with the binding energy predicted by theory when considering our error (±4.15 kcal/mol) and that of theory. DFT is commonly used in computations involving transition metals, but has been recognized as being problematic for thermochemistry and errors of 5 kcal/mol are not uncommon. Because of this, our derived value for the upper limit on the dissociation energy agrees reasonably well within uncertainties.

Conclusion

In the photodissociation of the $Zn^+(CH_3OH)$ complex, the charge transfer product, CH_3OH^+, is the dominant fragmentation product. The excess energy from photodissociation is partitioned between the internal rotational and vibrational states of the methanol product and translational energy. Photofragment imaging provides evidence for a significant amount of kinetic energy release upon dissociation. Measurement of the excess kinetic energy allows for the determination of an upper limit on the bond energy of this system. The values from imaging the CH_3OH^+ product agree reasonably well with those predicted by theory. Imaging of the Zn^+ fragment gives an unusual result for the kinetic energy release, and may suggest a multiphoton absorption process. Overall, this data provides new insight into the binding energetics and dissociative charge transfer dynamics on the excited potential energy surface of $Zn^+(CH_3OH)$.

References

1. Y. Marcus, *Ion Solvation* (John Wiley and Sons, Chichester, UK, 1985).
2. J. Burgess, *Ions in Solution* (Horwood Publishing, Chichester, UK, 1999).
3. Y. Marcus, *Ions in Solution and their Solvation* (John Wiley & Sons, Hoboken, NJ, 2015).
4. J. F. Hartwig, *Organotransition Metal Chemistry: From Bondiing to Catalysis* (University Science Books, Sausalito, CA, 2010).
5. I. Bertini, H. B. Gray, E. I. Stiefel, J. S. Valentine, *Biological Inorganic Chemistry: Structure and Reactivity* (University Science Books, Sausalito, CA, 2007).
6. P. Kebarle, "Ion Thermochemistry and Solvation from Gas Phase Ion Equilibria," Annu. Rev. Phys. Chem. **28**, 445 (1977).
7. T. F. Magnera, D. E. David, J. Michl, "Gas-Phase Water and Hydroxyl Binding Energies for Monopositive first-Row Transition Metal Ions," J. Am. Chem. Soc. **111**, 4100 (1989).
8. P. J. Marinelli, R. R. Squires, "Sequential Solvation of Atomic Transition-Metal Ions. The Second Solvent Molecule Can Bind More Strongly than the First," J. Am. Chem. Soc. **111**, 4101 (1989).
9. P. Jayaweera, A. T. Blades, M. G. Ikonomou, P. Kebarle, "Production and Study in the Gas Phase Multiply Charged Solvated or Coordinated Metal Ions," J. Am. Chem. Soc. **112**, 2452 (1990).
10. Y. M. Chen, D. E. Clemmer, P. B. Armentrout, "Conversion of CH_4 to CH_3OH: Reactions of CoO^+ with CH_4 and D_2, Co^+ with CH_3OD and D_2O, and $Co^+(CH_3OD)$ with Xe," J. Am. Chem. Soc. **116**, 7815 (1994).

11. N. F. Dalleska, K. Honma, L. S. Sunderland, P. B. Armentrout, "Solvation of Transition Metal Ions by Water. Sequential Binding Energies of $M^+(H_2O)_x$ (x = 1−4) for M = Ti to Cu Determined by Collision Induced Dissociation," J. Am. Chem. Soc. **166**, 3519 (1994).

12. C. A. Woodward, M. P. Dobson, A. J. Stace, "Chemistry of Mg^+ and Mg^{2+} in Association with Methanol Clusters," J. Phys. Chem. A **101**, 2279 (1997).

13. W. Lu, S. Yang, "Reactions of Alkaline Earth Metal Ions with Methanol Clusters," J. Phys. Chem. A **102**, 825 (1998).

14. D. Schröder, H. Schwarz, "Generation, Stability, and Reactivity of Small, Multiply Charged Ions in the Gas Phase," J. Phys. Chem. **103**, 7385 (1999).

15. J. C. Amicangelo, P. B. Armentrout, "Absolute Binding Energies of Alkali-Metal Cation Complexes with Benzene Determined by Threshold Collision-Induced Dissociation Experiments and Ab Initio Theory" J. Phys. Chem. A **104**, 11420 (2000).

16. A. Andersen, F. Muntean, D. Walter, C. Rue, P. B. Armentrout, "Collision-Induced Dissociation and Theoretical Studies of Mg^+ Complexes with CO, CO_2, NH_3, CH_3OH, and C_6H_6," J. Phys. Chem. A **104**, 692 (2000).

17. L. Poisson, P. Pradel, F. Lepetit, F. Réau, J.-M. Mestdagh, J.-P. Visticot, "Binding Energies of First and Second Shell Water Molecules in the $Fe(H_2O)^{2+}$, $Co(H_2O)^{2+}$ and $Au(H_2O)^{2+}$ Cluster Ions," Eur. Phys. J. D, **14**, 89 (2001).

18. V. E. Bondybey, M. K. Beyer, "Many Molecules Make a Solution?" Int. Rev. Phys. Chem. **21**, 277 (2002).

19. A. J. Stace, "Metal Ion Solvation in the Gas Phase: The Quest for Higher Oxidation States," J. Phys. Chem. A **106**, 7993 (2002).

20. P. B. Armentrout, “Guided Ion Beam Studies of Transition Metal-Ligand Thermochemistry,” Int. J. Mass Spectrom. **227**, 289 (2003).

21. H. Koizumi, M. Larsen, P. B. Armentrout, D. Feller, “Collision-Induced Dissociation and Theoretical Studies of Ag^+(methanol)$_n$, n = 1−4,” J. Phys. Chem. A **107**, 2829 (2003).

22. T. E. Cooper, D. R. Carl, P. B. Armentrout, “Hydration Energies of Zinc(II): Threshold Collision-Induced Dissociation Experiments and Theoretical Studies,” J. Phys. Chem. A **113**, 13727 (2009).

23. T. E. Cooper, J. T. O’Brien, E. R. Williams, P. B. Armentrout, “Zn^{2+} Has a Primary Hydration Sphere of Five: IR Action Spectroscopy and Theoretical Studies of Hydrated Zn^{2+} Complexes in the Gas Phase,” J. Phys. Chem. A **114**, 12646 (2010).

24. C. Van der Linde, S. Hemmann, R. F. Höckendorf, O. P. Balaj, M. K. Beyer, “Reactivity of Hydrated Monovalent First Row Transition Metal Ions $M^+(H_2O)_n$ M=V, Cr, Mn, Fe, Co, Ni, Cu, Zn, toward Molecular Oxygen, Nitrous Oxide, and Carbon Dioxide,” J. Phys. Chem. A **117**, 1011 (2013).

25. M. T. Rodgers, P. B. Armentrout, “Cationic Noncovalent Interactions: Energetics and Periodic Trends,” Chem. Rev **116**, 5642 (2016).

26. C. S. Yeh, K. F. Willey, D. L. Robbins, M. A. Duncan, “Photodissociation of Magnesium Ion/Molecule Complexes in a Relfectron Time-of-Flight Mass Spectrometer” Int. J. Mass Spectrom. **131**, 307 (1994).

27. J. Qian, A.J. Midey, S.G. Donnelly, J.I. Lee, J.M. Farrar, “Solvated metal cation photochemistry. Electronic state-selective reaction versus evaporation in $Sr^+(CH_3OH)/Sr^+(CH_3OD)$,” Chem. Phys. Lett. **244**, 414 (1995).

28. M. R. France, S. H. Pullins, M. A. Duncan, "Photodissociation of Mg^+-$(CH_3OH)_N$ Complexes: Evidence for the Onset of Solvation." Chem. Phys. **239**, 447 (1998).

29. W.-Y. Lu, T.-H. Wong, P. D. Kleiber, "Photochemistry of $Zn^+(CH_4)$," Chem. Phys. Lett. **347**, 183 (2001).

30. W.-Y. Lu, P. D. Kleiber, M. A. Young, "Photodissociation Spectroscopy of $Zn^+(C_2H_4)$," J. Chem. Phys. **115**, 5823 (2001).

31. W.-Y. Lu, T.-H. Wong, Y. Sheng, A. T. Lytle, P. D. Kleiber, "Photodissociation Spectroscopy of Zn^+—Methanol," J. Phys. Chem. A **107**, 984 (2003).

32. W. Lu, Y. Abate, T.-H. Wong, P. D. Kleiber, "Photodissociation Spectroscopy of Zn^+—Formaldehyde," J. Phys. Chem. A **108**, 10661 (2004).

33. R. B. Metz, "Photofragment Spectroscopy of Covalently bound Transition Metal Complexes: A Window into C−H and C−C Bond Activation by Transition Metal Ions," Int. Rev.Phys. Chem. **23**, 79 (2004).

34. Y. Abate, P. D. Kleiber, "Photodissociation Spectroscopy of $Zn^+(H_2O)$ and $Zn^+(D_2O)$," J. Chem. Phys. **122,** 084305 (2005).

35. N. C. Polfer, J. Oomens, "Vibrational Spectroscopy of Bare and Solvated Ionic Complexes of Biological Relevance," Mass Spectrom. Rev. **28**, 468 (2009).

36. G. Altinay, M. Citir, R. B. Metz, "Vibrational Spectroscopy of Intermediates in Methane-to-Methanol Conversion by FeO^+," J. Phys. Chem. A **114**, 5104 (2010).

37. K. Furukawa, K. Ohashi, T. Imamura, J. Sasaki, K. Judai, N. Nishi, H. Sekiya, "Methanol Solvation of the Ag^+ Ion Probed with Infrared Photodissociation Spectroscopy of $Ag^+(CH_3OH)_n$ (n = 1-5)," Chem. Phys. Lett. **495**, 8 (2010).

38. B. Bandyopadhyay, K. N. Reishus, M. A. Duncan, “Infrared Spectroscopy of Solvation in Small $Zn^+(H_2O)_n$ Complexes,” J. Phys. Chem. A **117**, 7794 (2013).

39. E. M. Cunningham, T. Taxer, J. Heller, M. Ončák, C. van der Linde, M. K. Beyer, “Microsolvation of Zn Cations: Infrared Multiple Photon Dissociation Spectroscopy of $Zn^+(H_2O)_n$ (n = 2-35),” Phys. Chem. Chem. Phys. **23**, 3627 (2021).

40. M. Rosi, C. W. Bauschlicher, Jr., “The Binding Energies of One and Two Water Molecules to the first Transition-Row Metal Positive Ions,” J. Phys. Chem A **90**, 7264 (1989).

41. M. Rosi, C. W. Bauschlicher, Jr., “The Binding Energies of One and Two Water Molecules to the first Transition-Row Metal Positive Ions,” J. Phys. Chem A **92**, 1876 (1990).

42. C. W. Bauschlicher, Jr., M. Sodupe, H. Partridge, “A Theoretical Study of the Positive and Dipositive Ions of $M(NH_3)_n$ and $M(H_2O)_n$ for M=Mg, Ca, or Sr,” J. Chem. Phys. **96**, 4453 (1992).

43. D. Feller, E. D. Glendening, R. A. Kendall, K. A. Peterson, “An Extended Basis Set Ab Initio Study of $Li^+(H_2O)_n$, n=1−6,” J. Chem. Phys. **100**, 4981 (1994).

44. E. D. Glendening, D. Feller, “Cation-Water Interactions: the $M^+(H_2O)_n$ Clusters for Alkali Metals, M = Li, Na, K, Rb, and Cs,” J. Phys. Chem. **99**, 3060 (1995).

45. H. Watanabe, S. Iwata, K. Hashimoto, F. Misaizu, K. Fuke, “Molecular Orbital Studies of the Structures and Reactions of Singly Charged Magnesium Ion with Water Clusters, $Mg^+(H2O)_n$,” J. Am. Chem. Soc. **117**, 755 (1995).

46. E. Wasserman, J. R. Rustad, S. S. Xantheas, “Interaction Potential of Al^{3+} in Water from First Principles Calculations,” J. Chem. Phys. **106**, 9769 (1997).

47. J. M. Mercero, J. M. Matxain, X. Lopez, D. M. York, A. Largo, L. A. Eriksson, J. M. Ugalde, “Theoretical Methods that Help Understanding the Structure and Reactivity of Gas Phase Ions,” **240**, 37 (2005).

48. M. Schlangen, H. Schwarz, “Effects of Ligands, Cluster Size, and Charge State in Gas-Phase Catalysis: A Happy Marriage of Experimental and Computational Studies,” Catal. Lett. **142**, 1265 (2012).

49. H. Schwarz, “Ménage à trois: single-atom catalysis, mass spectrometry, and computational chemistry,” Catal. Sci. Technol. **7**, 4302 (2017).

50. A. Kramida, Yu. Ralchenko, J. Reader, NIST ASD Team NIST Atomic Spectra Database, ver. 5.9; National Institute of Standards and Technology: Gaithersburg, MD, 2021. https://physics.nist.gov/asd (accessed 2022-02-22).

51. S. G. Lias, “Ionization Energy Evaluation” In NIST Chemistry WebBook, NIST Standard Reference Database Number 69, P. J. Linstrom, W. G. Mallard, Eds.; National Institute of Standards and Technology: Gaithersburg, MD (accessed 2022-02-22). DOI: 10.18434/T4D303.

52. M. F. Jarrold, L. Misev, M.T. Bowers, “Charge Transfer Half-Collisions: Photodissociation of the $Kr{\cdot}O_2^+$ Cluster Ion with Resolution of the O_2 Product Vibrational States,” J. Chem. Phys. **81**, 4369 (1984).

53. J. I. Illies, M. F. Jarrold, W. Wagner-Redeker, M. T. Bowers, “Photoinduced Intramolecular Charge Transfer: Photodissociation of $CO_2^+{\cdot}Ar$ Cluster Ions,” J. Am. Chem. Soc. **107**, 2842 (1985).

54. H.-S. Kim, C.-H. Kuo, M. T. Bowers, "Photon Driven Charge Transfer Half Collisions: The Photodissociation of $CO_2^+ \cdot O_2$ Cluster Ions with Resolution of the O_2 Product Vibrational States." J. Chem. Phys.**87**, 2667 (1987).

55. K. F. Willey, P. Y. Cheng, K. D. Pearce, M. A. Duncan, "Photoinitiated Charge Transfer and Dissociation in Mass-Selected Metallo-Organic Complexes," J. Phys. Chem**. 94**, 4769 (1990).

56. K. F. Willey, P. Y. Cheng, M. B. Bishop, M. A. Duncan, "Charge-Transfer Photochemistry in Ion-Molecule Cluster Complexes of Silver," J. Am. Chem. Soc. **113**, 4721 (1991).

57. K. F. Willey, C. S. Yeh, D. L. Robbins, M. A. Duncan, "Charge Transfer in the Photodissociation of Metal Ion-Benzene Complexes," J. Phys. Chem. **96**, 9106 (1992).

58. J. Chen, T. H. Wong, Y. C. Cheng, K. Montgomery, P. D. Kleiber, "Photodissociation Spectroscopy and Dynamics of $MgC_2H_4^+$." J. Chem. Phys. **108**, 2285 (1998).

59. Y.-S.Yang, C.-S. Yeh, "Photodissociative Charge Transfer in Ag^+-Pyridine Complex," Chem. Phys. Lett," **305**, 395 (1999).

60. Y.-S. Yang, W.-Y. Hsu, H.-F. Lee, Y.-C. Huang, C.-S. Yeh, "Experimental and Theoretical Studies of Metal Cation-Pyridine Complexes Containing Cu and Ag," J. Phys. Chem. A **103**, 11287 (1999).

61. P. H. Su, C. S. Yeh, "Photofragmentation of the Ag^+-Furan Complex in the Gas-Phase," Chem. Phys. Lett. **331**, 420 (2000).

62. P. H. Su, F. W. Lin, C. S. Yeh, "Photodissociation Studies of $M(Furan)^+$ (M = Cu, Ag, and Au) and $Au(C_3H_4)^+$ Complexes," J. Phys. Chem. A **105**, 9643 (2001).

63. H.-C. Hsu, F.-W. Lin, C.-C. Lai, P.-H. Su, C.-S. Yeh, "Photodissociation and Theoretical Studies of the Au^+-(C_5H_5N) Complex," New J. Chem. **26**, 481 (2002).

64. T. D. Jaeger, M. A. Duncan, "Photodissociation of $M^+(benzene)_x$ Complexes (M = Ti, V, Ni) at 355 nm," Int. J. Mass Spectrom. **241**, 165 (2005).

65. J. A. Maner, D. T. Mauney, M. A. Duncan, "Velocity Map Ion Imaging Study of Ar_2^+ Photodissociation," Chem. Phys. Lett. **671**, 182 (2017).

66. J. A. Maner, D. T. Mauney, M. A. Duncan, "Imaging Charge Transfer in a Cation-π System: Velocity-Map Imaging of Ag^+(benzene) Photodissociation," J. Phys. Chem. Lett. **6**, 4493 (2015).

67. B. M. Rittgers, D. Leicht, M. A. Duncan, "Cation−π Complexes of Silver Studied with Photodissociation and Velocity-Map Imaging," J. Phys. Chem A **124**, 9166 (2020).

68. M. A. Duncan, "Laser Vaporization Cluster Sources," Rev. Sci. Instrum. **83**, 041101 (2012).

69. D. S. Cornett, M. Peschcke, K. LaiHing, P. Y. Cheng, K. F. Willey, M. A. Duncan, "Reflectron Time-of-Flight Mass Spectrometer for Laser Photodissociation," Re. Sci. Instrum. **63**, 2177 (1992).

70. W. Li, S. D. Chambreau, S. A. Lahankar, A. G. Suits, "Megapixel Ion Imaging with Standard Video," Rev. Sci. Instrum. **76**, 063106 (2005). See also: Suits, A. G. NuAcq 0.9 software. http://faculty.missouri.edu/suitsa/NuAcq.html.

71. H. Hoshino, Y. Yamakita, K. Okutsu, Y. Suzuki, M. Saito, K. Koyasu, K. Ohshimo, F. Misaizu, "Photofragment Imaging from Mass-Selected Ions Using a Reflectron Mass Spectrometer I. Development of an Apparatus and Application to Mg^+-Ar," Chem. Phys. Lett. **630**, 111 (2015).

72. K. Okutsu, K. Ohshimo, H. Hoshino, K. Koyasu, F. Misaizu, “Photofragment Imaging from Mass-Selected Ions Using a Reflectron Mass Spectrometer II. Formation Mechanism of MgF^+ in Photodissociation of Mg^+-FCH_3 Complex,” Chem. Phys. Lett. **630**, 57 (2015).

73. K. Okutsu, K. Yamazaki, K. Ohshimo, F. Misaizu, “Photofragment Ion Imaging from Mass-Selected Mg^+-$BrCH_3$ Complex: Dissociation Mechanism Following Photoinduced Charge Transfer,” J. Chem. Phys. **146**, 024301 (2017).

74. K. Okutsu, Y. Nakashima, K. Yamazaki, K. Fujimoto, M. Nakano, K. Ohshimo, F. Misaizu, “Development of a Linear-Type Double Reflectron for Focused Imaging of Photofragment Ions from Mass-Selected Complex Ions,” Rev. Sci. Instrum. **88**, 053105 (2017).

75. K. Okutsu, K. Yamazaki, M. Nakano, K. Ohshimo, F. Misaizu, “Ion Imaging of MgI^+ Photofragment in Ultraviolet Photodissociation of Mass-Selected Mg^+ICH_3 Complex,” J. Phys. Chem. A **122**, 4948 (2018).

76. M. D. Johnston, W. L. Pearson III, G. Wang, R. B. Metz, “A Velocity Map Imaging Mass Spectrometer for Photofragments of Fast Ion Beams,” Rev. Sci. Instrum. **89**, 014102 (2018).

77. M. D. Johnston, S. P. Lockwood, R. B. Metz, “Photofragment Imaging and Electronic Spectroscopy of Al^{2+},” J. Chem. Phys. **148**, 214308 (2018).

78. M. D. Johnston, M. R. Gentry, R. B. Metz, “Photofragment Imaging, Spectroscopy, and Theory of MnO^+,” J. Phys. Chem. A **122**, 8047 (2018).

79. Eppink, A. T. J. B.; Parker, D. H. Velocity Map Imaging of Ions and Electrons Using Electrostatic Lenses: Application in Photoelectron and Photofragment Ion Imaging of Molecular Oxygen. *Rev. Sci. Instrum.* **1997**, *68*, 3477-3484.

80. M. J. Frisch, G. W. Trucks, H. B. Schlegel, G. E. Scuseria, M. A. Robb, J. R. Cheeseman, G. Scalmani, V. Barone, G. A. Petersson, H. Nakatsuji, X. Li, M. Caricato, A. V. Marenich, J. Bloino, B. G. Janesko, R. Gomperts, B. Mennucci, H. P. Hratchian, J. V. Ortiz, A. F. Izmaylov, J. L. Sonnenberg, D. Williams-Young, F. Ding, F. Lipparini, F. Egidi, J. Goings, B. Peng, A. Petrone, T. Henderson, D. Ranasinghe, V. G. Zakrzewski, J. Gao, N. Rega, G. Zheng, W. Liang, M. Hada, M. Ehara, K. Toyota, R. Fukuda, J. Hasegawa, M. Ishida, T. Nakajima, Y. Honda, O. Kitao, H. Nakai, T. Vreven, K. Throssell, J. A. Montgomery, Jr., J. E. Peralta, F. Ogliaro, M. J. Bearpark, J. J. Heyd, E. N. Brothers, K. N. Kudin, V. N. Staroverov, T. A. Keith, R. Kobayashi, J. Normand, K. Raghavachari, A. P. Rendell, J. C. Burant, S. S. Iyengar, J. Tomasi, M. Cossi, J. M. Millam, M. Klene, C. Adamo, R. Cammi, J. W. Ochterski, R. L. Martin, K. Morokuma, O. Farkas, J. B. Foresman, and D. J. Fox, Gaussian 16 Revision C.01, Gaussian, Inc., Wallingford CT, 2016.

81. F. Aguirre, J. Husband, C. J. Thompson, K. L. Stringer, R. B. Metz. "Electronic Spectroscopy of Intermediates Involved in the Conversion of Methane to Methanol by FeO^+." J. Chem. Phys. **116**, 4071 (2002).

82. Harvey, J. N. DFT Computation of Relative Spin-State Energetics of Transition Metal Compounds. *Structure and Bonding.* **2004**, *112*, 151–184.

83. Cramer, C. J.; Truhlar, D. J. Density Functional Theory for Transition Metals and Transition Metal Chemistry. *Phys. Chem. Chem. Phys.* **2009**, *11*, 10757–10816.

84. Cohen, A. J.; Mori-Sanchez, P.; Yang, W. Challenges for Density Functional Theory. *Chem. Rev.* **2012**, *112*, 289–320.

85. Shil, S.; Bhattacharya, D.; Sarkar, S.; Misra, A. Performance of the Widely Used Minnesota Density Functionals for the Prediction of Heat of Formations, Ionization Potentials of Some Benchmarked First Row Transition Metal Complexes. *J. Phys. Chem. A* **2013**, *117*, 4945–4955.

86. Moltved, K. A.; Kepp, K. P. Chemical Bond Energies of 3d Transition Metals Studied by Density Functional Theory. *J. Chem. Theory Comput.* **2018**, *14*, 3479−3492.

CHAPTER 5

VELOCITY MAP IMAGING OF CARBON CLUSTER CATIONS: EVIDENCE FOR EXPLOSIVE RING RUPTURE

Introduction

The study of pure carbon clusters has been an ongoing venture for chemists and physicists for some time.[1] They exist in a wide variety of sizes and geometries, and can be found in neutral, cationic, or anionic charge states. Carbon clusters have been of astrochemical relevance since their discovery in comets more than a century ago.[2,3] They play an important role in the chemistry of carbon rich stars and comets,[2-6] and have also been implicated as carriers of the unassigned diffuse interstellar bands (DIBS).[7-20] The clusters C_2, C_3, C_5, C_{60}, C_{60}^+, and C_{70} have all been identified within molecular clouds and circumstellar environments,[4,5,15-18,21-25] and they can act as building blocks for more complex carbon containing molecules and larger pure carbon materials.[23] The discovery of C_{60} led to an increase in the interest of new materials made of pure carbon,[26,27] which facilitated the discovery graphene and carbon nanotubes.[28,29] In this work, the photodissociation dynamics of small carbon cluster cations are studied using velocity map imaging of mass-selected ions.

Small carbon clusters are highly reactive species, which makes their experimental synthesis and characterization challenging.[29,30] However, they are the predominant species in soot producing flames, and it has been determined that emission from C_2 is responsible for the blue glow in burning hydrocarbons.[31] It has also been shown that they are important intermediates in the production of carbon thin films.[32] These clusters also posses a high density

of singlet/triplet electronic states that lie low in energy and they have significant multi-reference character, which makes the theoretical treatment of these systems a challenge.[33-48] Despite these challenges, it is important to understand the properties of small carbon clusters to attain an understanding of the possible mechanisms that lead to the formation of larger structures (e.g., fullerenes, polycyclic rings, or nanotubes) or to aid in their detection in space.

There is an extensive amount of work already done on carbon clusters using matrix isolation, optical and infrared spectroscopy, and mass spectrometry-based techniques.[12-14,16-18,49-70] Maier and coworkers measured the electronic spectroscopy of C_{60}^+ and C_{60}^- in neon matrices, which indicated they may be responsible for two DIBs.[16,17] However, the spectroscopy done in neon matrices cannot be directly compared to astronomical observations due to matrix shifts in the absorption bands. Maier and coworkers later followed up with observations of the electronic spectroscopy of cold C_{60}^+ in gas phase.[16,17] This work confirmed the presence of C_{60}^+ in the interstellar medium and identified the carrier of two of the DIBS. Bowers and coworkers have studied the ion mobility of carbon cluster cations from C_3^+ to C_{84}^+.[64-66] Their results indicate that linear structures exist up to C_{10}^+ with ring structures beginning at C_7^+, so there is some mixture of linear and ring structures between C_7^+-C_{10}^+. The ring structures persist up to C_{40}^+ with bicyclic rings beginning at C_{30}^+ and tricyclic rings starting at C_{30}^+. Three dimensional structures begin at C_{29}^+, however, the exact structure could not be unambiguously identified. Collision induced dissociation (CID) studies measured bond energies for these clusters in the range of 4−6 eV. [57,60] Theoretical studies supported the results for the binding energies from CID.[34-37,39,40,69] Interestingly, theory also predicts the cyclic structures are lower in energy for C_6^+−C_9^+. The observed linear structures for the smaller clusters are likely due to the amount of energy available during cluster formation. Entropy favors chains rather than rings, which means the

linear structures may preferentially form in a laser ablation source. However, because of the multireference character in the carbon cluster electronic structure and the difficulty of thermochemistry experiments on strongly bound complexes, these results remain uncertain.

UV photodissociation experiments found that carbon cluster cations dissociated quite efficiently at thresholds near 3.5 eV.[55,58,59,61,70] These results contradicted those of the CID experiments and theory. However, this discrepancy was later determined to be the result of efficient multiphoton absorption. Because of the high binding energies and low-lying electronic states in these clusters, it is impossible to do photodissociation spectroscopy under single photon conditions without the aid of tagging. Recently, helium and nitrogen tagging were used to obtain the electronic spectra of carbon cluster cations for sizes ranging from C_5^+–C_{28}^+ in the visible to near-infrared.[71-73] The origin band of the lowest lying $^2\Pi_g \leftarrow X\ ^2\Sigma_u^+$ transition of C_5^+ was found to be at 513 nm; this band redshifts as cluster size grows. Campbell and coworkers successfully carried out a two-color experiment to obtain the electronic spectrum of bare C_5^+, thus eliminating any perturbation caused by the helium tagging. The C_5^+-He and C_5^+ spectra matched within the error bars of the experiment.

Although the bond energies derived from UV photodissociation experiments proved to be unreliable, valuable information on the dynamics of carbon cluster cation fragmentation was still obtained.[53-55,57,59] It was shown that neutral C_3 is a prominent fragmentation product, and the sole product coming from linear clusters (C_7^+–C_{10}^+), whereas C_2 and C_5 were also eliminated from clusters with a cyclic structure. Here, photofragment ion imaging is used to explore the multiphoton photodissociation dynamics of carbon cluster cations, C_n^+ (n = 6, 7, 10, 11, 12, 15, and 20), to identify any possible differences in the photodissociation dynamics of ring vs. linear structures.

Experimental

Carbon cluster cations were produce via laser vaporization of an amorphous carbon rod with the third harmonic of a Nd:YAG laser (Continuum Surelite SL-10) in a pulsed supersonic expansion of helium. The so-called "2-4 turbo" block was used to hold the rod in place and confine the gas pulse in the region of the laser plasma.[74,75] The block has a 2 mm hole bored from where gas enters the block from the nozzle, which then expands to a 4 mm hole in the region after the rod. This increases the number of collisions and promotes cluster growth of the rod being vaporized. The vaporization conditions employed are the same as used in previous ion mobility and electronic spectroscopy experiments. Therefore, cluster structures are assumed to be the same as in those experiments, i.e., linear for $C_{6\text{-}9}^{+}$ and cyclic for $C_{10\text{-}20}^{+}$. Ions are skimmed and extracted orthogonally into a reflectron time-of-flight mass spectrometer. Pulsed deflection plates are used for mass selecting ions for photodissociation in the reflectron. Mass spectra with and without photodissociation are recorded in the second flight tube of the reflectron using methods described previously.

For imaging experiments, the reflectron is grounded to allow ions to pass through it and into the imaging flight tube as described in Chapter 2. In the imaging flight tube, ions are initially decelerated before photodissociation at 355 nm with a Nd:YAG laser (Spectra Physics GCR-170). After dissociation, ions are reaccelerated using a stack of electrostatic lenses optimized for velocity map imaging (VMI)[76] onto a dual MCP/phosphor screen position sensitive detector (Beam Imaging Solutions). The detection of the fragment ions is done by time-gating the detector; however, the expanding ion cloud is not "sliced" as in previous experiments,[77-82] to reduce data acquisition times, and the full two-dimensional projection is recorded. Each ion impact is recorded using a CCD camera (Edmund Optics) and accumulated using the NuAcq

software of the Suits' group.[79] Structures and energetics were calculated in the Gaussian16 program package at the B3LYP/def2-TZVP level of theory.[83]

Results and Discussion

Laser vaporization of a carbon rod in the turbo block source generates carbon cluster ions of the form C_n^+, out to approximately *n = 24*. The carbon cluster mass spectrum produced by this method is shown in Figure 5.1., and the photodissociation mass spectra of C_6^+, C_7^+, C_{10}^+, C_{11}^+, C_{12}^+, C_{15}^+, and C_{20}^+ are shown in Figure 5.2. The photodissociation mass spectra are recorded in a difference mode of operation where an average with the laser off is subtracted from an average with the laser on. The amount of averaging is the same for both the laser on and laser off. This produces a mass spectrum showing depletion of the parent ion intensity as a negative signal and formation of the fragment ions as positive signal. The mass spectrometer is optimized for fragment ion intensity, so the signal for parent ion depletion is not representative of its actual intensity. In all photodissociation mass spectra, C_3 is the major neutral fragment observed, but there are also prominent fragment peaks corresponding to loss of C_2 and C_5. There is no fragmentation observed at laser powers below 15 mJ/pulse-cm^2, which indicates that photodissociation is a result of multiphoton absorption.

Our photofragment imaging experiment is able to determine the bond energy in simple systems such as Ar_2^+,[81] where excess energy can only go into kinetic energy, or to put upper limits on the binding energy for larger complexes with many degrees of freedom.[80,82] However, the laser power must be carefully controlled in order to ensure that only single photon absorption is occurring so that the amount of energy entering the system is well known. In the case of carbon clusters, the exact amount of energy deposited into the cluster is unknown because

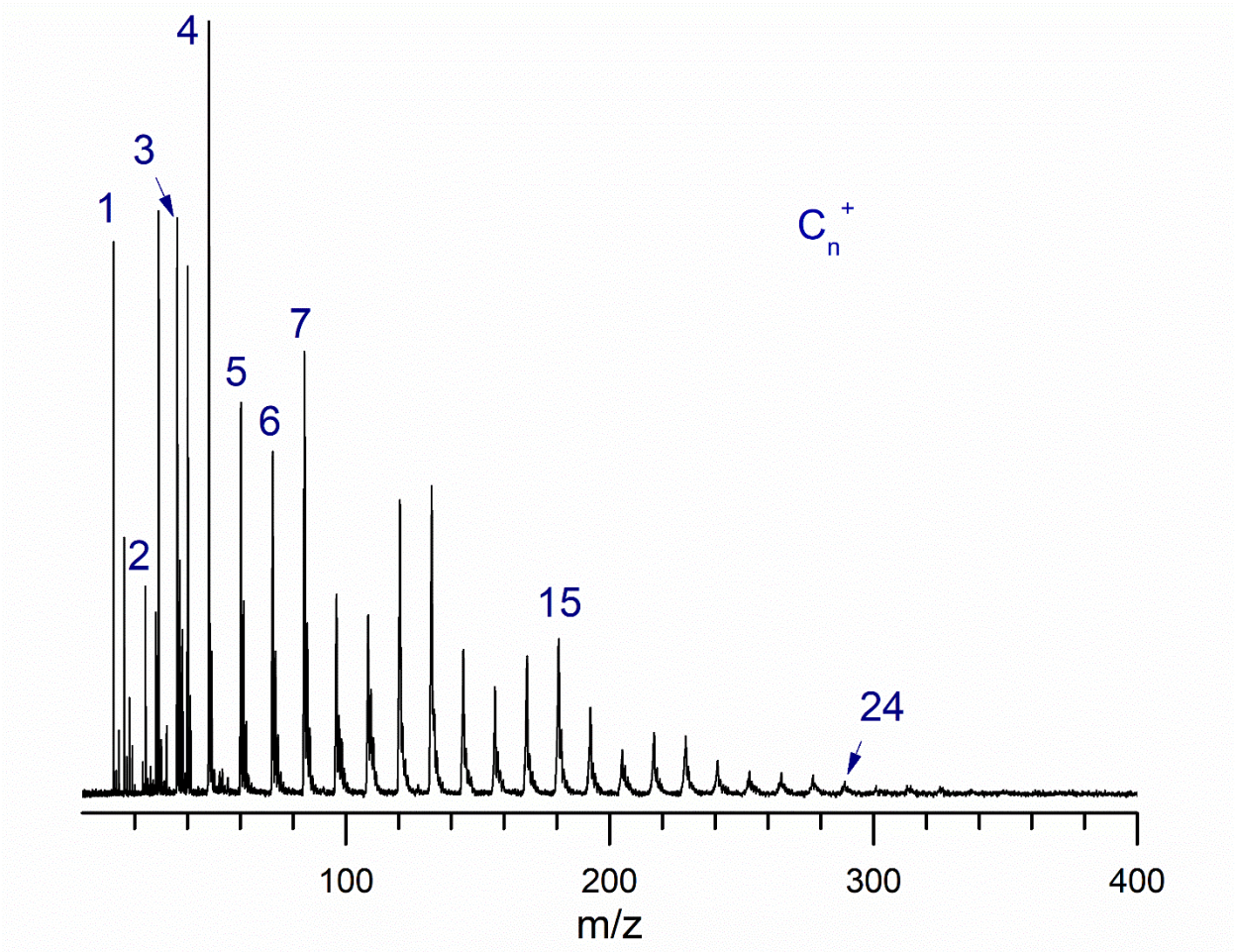

Figure 5.1. Mass spectrum obtained from laser vaporization of a carbon rod.

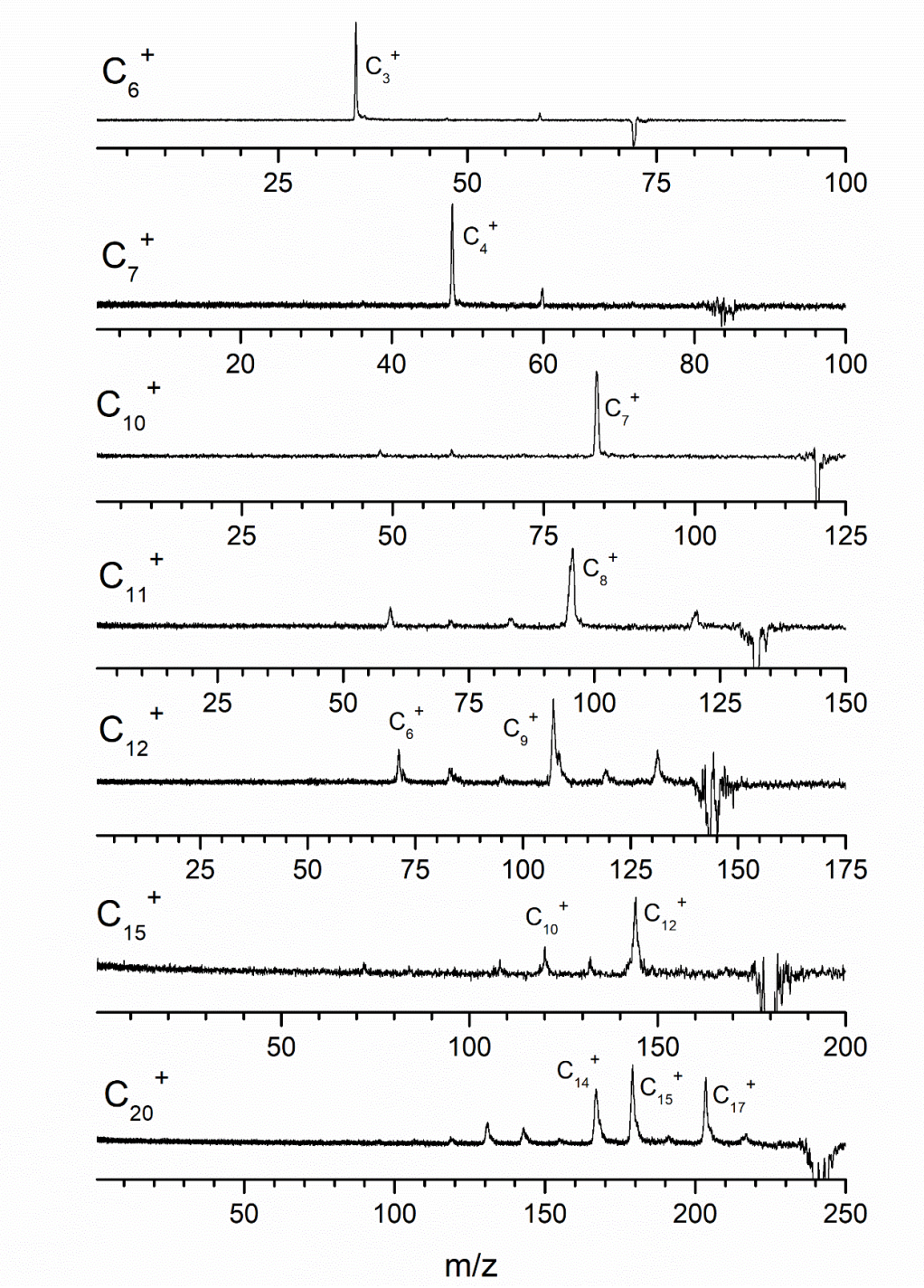

Figure 5.2. Photodissociation mass spectrum of C_6^+, C_7^+, C_{10}^+, C_{11}^+, C_{12}^+, C_{15}^+, and C_{20}^+ at 355 nm.

dissociation is a result of multiphoton absorption. Therefore, we are unable to use an energetic cycle like that discussed previously to put an upper limit on the dissociation energy.

Although no information on the binding energies of these clusters can be obtained, photofragment imaging has still provided intriguing results on the photodissociation dynamics of carbon cluster cations. Figure 5.3 show the raw images from photodissociation of C_6^+, C_7^+, C_{10}^+, C_{11}^+, C_{12}^+, C_{15}^+, and C_{20}^+ along with the corresponding kinetic energy release (KER) spectra. Initially, the most striking result is that the larger clusters seem to produce larger images. This is unusual because if the different size clusters produced the same amount of KER, the images from larger clusters would be smaller because of the heavier fragments. This means that the KER from larger clusters is not just the same as the smaller ones, but *more*, as can been seen from the analysis of the images in the KER spectra. The maximum KER values range from about 1.0 eV for C_6^+ and C_7^+ up to 6.4 eV for C_{20}^+, as shown in Table 5.1. These differences could be from the absorption of more photons in the larger clusters, or more interestingly, that dissociation of a ring structure inherently produces more KER. For large systems such as these, there is typically a large distribution of kinetic energies, which correspond to fragments that are produced with some amount of internal energy during the photodissociation process. In these images, the greatest signal intensity is concentrated in the center, indicating that most of the fragments are generated with a significant amount of internal energy. However, some of the ions are produced with a large amount of kinetic energy, located at the outer edge of the image, which is where we determine the maximum kinetic energy release (KER_{max}). of the ions are produced with a large amount of kinetic energy, located at the outer edge of the image, which is where we determine the maximum kinetic energy release (KER_{max}).

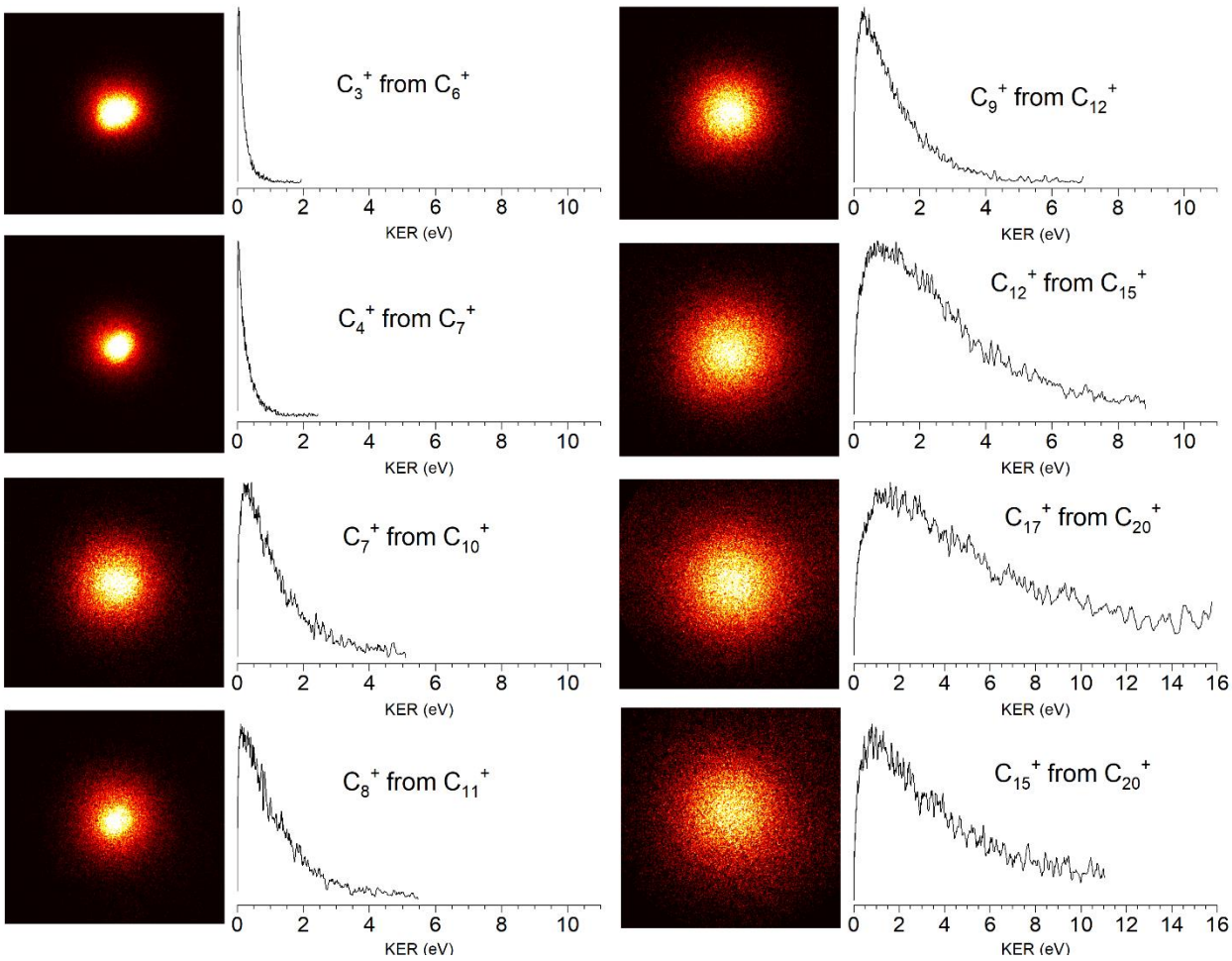

Figure 5.3. Images and kinetic energy release spectra of C_6^+, C_7^+, C_{10}^+, C_{11}^+, C_{12}^+, C_{15}^+, and C_{20}^+ from photodissociation at 355 nm.

Table 5.1 shows KER_{max} values determined in our experiment along with the bond energies from CID. [57,60] The excess energy available from absorption of 2 or 3 photons is also listed, which is determined using the CID dissociation energies.[57,60] If C_6^+ were to absorb two photons, there would be 1.71 eV worth of excess energy, and 5.27 eV for a three-photon absorption. Either of these values could produce the KER_{max} observed, however, it is likely that a two-photon process is taking place along with internal excitation of the fragments. In the case of C_7^+, two-photon absorption only gives 0.68 eV of excess energy and three-photon provides 4.57 eV. Unless the bond energy is lower than determined previously, two-photons is not enough energy to account for the 1.0 eV KER_{max} observed. However, three photons do account for the excess energy, and a significant amount of excess energy goes into internal excitation of the fragments.

The KER_{mzx} for C_{10}^+, C_{11}^+, and C_{12}^+ are 2.8, 2.7, and 3.0 eV, respectively. These values are about three times higher than that for C_6^+ and C_7^+. In the case of these clusters, the absorption of just two photons does not provide enough energy to produce the KER_{mzx} values observed, or even cause dissociation of C_{11}^+. These results indicate that a three-photon, or possibly even four-photon, process is occurring. C_{15}^+ and C_{20}^+ both produce over 6 eV worth of kinetic energy. The binding energy for C_{20}^+ has not been measured with CID, [57,60] so it is assumed to be the same as C_{15}^+. The observed KER_{max} for these two cluster sizes would require the absorption of four photons. It is surprising that efficient multiphoton absorption is required to dissociate these larger clusters, yet much of the energy is converted into KER.

Another possibility that is affecting the results of these measurements is the amount of steric strain present in the cyclic structures of these complexes. This issue has been discussed previously by Jarrold and coworkers for clusters undergoing collisional excitation; they estimate

Table 5.1. Energetics of carbon cluster cations (eV). Excess energies are for excitation with either two or three photons at 355 nm (3.49 eV).

	D_0 CID[57]	KER_{max}	Photons/Excess Energy	Ring Strain[84]
l-$C_6^+ \rightarrow C_3^+ + C_3$	5.2	0.8	2/1.71; 3/5.2.7	n/a
l-$C_7^+ \rightarrow C_4^+ + C_3$	6.3	0.9	2/0.68; 3/4.17	n/a
c-$C_{10}^+ \rightarrow C_7^+ + C_3$	5.9	2.8	2/1.08; 3/4.57	5.38
c-$C_{11}^+ \rightarrow C_8^+ + C_3$	7.3	2.7	3/3.17	4.89
c-$C_{12}^+ \rightarrow C_9^+ + C_3$	6.5	3.0	2/0.48; 3/3.97	4.48, 2.35[a]
c-$C_{15}^+ \rightarrow C_{12}^+ + C_3$	5.6	6.0	2/1.38; 3/4.87	3.59, 2.97[a]
c-$C_{20}^+ \rightarrow C_{17}^+ + C_3$	-	6.4	2/1.38; 3/4.87[b]	2.69, 2.14[a]
c-$C_{20}^+ \rightarrow C_{15}^+ + C_5$	-	5.9	2/1.38; 3/4.87[b]	2.69, 2.14[a]

[a]present work, computed.
[b]estimated value assuming D_0 (C_{20}^+) = 5.6 eV (i.e., same as C_{15}^+).

that the ring strain in these clusters is in the range of 5−7 eV.[84-86] We have computed these effects at a higher level of theory that gave similar results. Both estimates are presented in Table 5.1, and although they are very approximate, the strain is significant and is greater for small rings, ranging from 5 eV for C_{10}^+ to under 3 eV for C_{20}^+. As the ring breaks, it is possible that the fragments recoil from the strain in the ring, which may contribute to the amount of KER. The strain energies are comparable to that of a 355 nm photon (3.49 eV), so if ring strain contributes to KER, the number of photons required to explain the results is one less. C_{15}^+ and C_{20}^+ would still require a three-photon process. Considering ring strain, the case of C_{11}^+ is interesting because two photons would then be enough to break the bond and explain the KER. However, it is not clear that the ring strain energy can affect bond breaking, as opposed to only being released after bond breaking. If it could affect the bond breaking, ring strain would have affected the thresholds measured by CID, so it is more plausible the ring strain is released after bond breaking. Therefore, C_{11}^+ still requires a three-photon absorption for dissociation, and the KER observed for this cluster size is a smaller portion of the excess energy available compared to other cluster sizes. However, ring strain does not completely account for the trend of increasing KER with cluster size, as larger clusters have less ring strain but larger $KER_{max.}$

Another factor that could contribute to some kinetic energy release is the internal energy of the clusters. When the clusters grow in the gas expansion, energy equivalent to that of the bond being made is deposited into the internal degrees of freedom of the cluster and heats it. This makes carbon clusters difficult to cool in the supersonic expansion because of their high binding energies. A greater amount of internal energy in the clusters before photodissociation would result in a greater kinetic energy release. To test this, we used different expansion gases to see the effects of cooling on the maximum kinetic energy release (Appendix C). This did not affect

the observed KER by any significant amount. Although it is difficult to be sure that the clusters are as cold as possible, any residual energy does not affect the measured KER_{max} by any significant amount.

Because of the uncertainties in the exact energy entering the system and the effects of ring strain, it is not possible to determine the type of energetics discussed in the previous chapters. However, it is evident that photodissociation of C_6^+ only requires a two-photon absorption with about half of the excess energy going into KER, and C_7^+ requires three-photons with only about 25% going into KER. C_{10}^+ and C_{12}^+ could be dissociated with three-photons at 355 nm, or only two if ring strain plays a significant part in the dissociation dynamics. Three photons would be enough to dissociate the C_{11}^+ cluster, however almost all of the excess energy would have to go into KER; this is relaxed if there is any contribution from ring strain. C_{15}^+ and C_{20}^+ can be explained by either a four-photon absorption or a three-photon absorption with a significant contribution from ring strain to KER. With these high numbers of photon absorption, it is necessary to consider how such processes are possible. Other work in the lab has shown that there is a quasi-continuum at wavelengths lower than 450 nm. If there are resonances across this entire region present in other clusters, then the efficiency of multiphoton absorption is understandable.

These results showing such high KER values is surprising for these carbon cluster cations. Photoexcitation at high energies usually results in prompt fluorescence or rapid non-radiative relaxation through intersystem crossing, internal conversion, and intramolecular vibrational relaxation (IVR). Significant redistribution of energy across the internal degrees of freedom is therefore expected prior to dissociation, resulting in a smaller fraction of available excess energy for KER. A larger amount of energy redistribution is expected as cluster sizes

increase as the density of electronic and vibrational states increase. Prompt photodissociation is possible where photoexcitation is localized to a specific moiety or functional group. However, the molecular orbitals involved in excitation should be delocalized across the entire carbon cluster due to their symmetry. Hitting the repulsive wall of an excited electronic state will also enhance the kinetic energy release, however, it is unlikely that this would happen for *all* of the carbon clusters investigated here and at different wavelengths. The production of such high KER that increases with cluster size is therefore quite surprising.

The best explanation here is that carbon cluster cations efficiently absorb multiple photons in the UV and that the excess energy is not effectively redistributed across the cluster. This could be due to the rigid structures and poor coupling between electronic and vibrational states, which leads to a significant amount of kinetic energy release, even for the linear structures where ring strain does not play a role. The photochemistry here must be composed of a strange mixture of efficient UV absorption and dynamical conversion of ring strain into kinetic energy. Unfortunately, these remarkable dynamics are completely intractable by theory at the moment because of their size and the fact that higher electronic and vibrational states are unknown.

Conclusion

Carbon clusters cations in the range from C_6^+–C_{20}^+ were successfully photodissociated and imaged at 355 nm, despite one-photon not being enough energy to break any bonds in these structures. Neutral C_3 was seen to be the most prominent elimination product, as has been seen previously. Photodissociation of these clusters surprisingly produced a significant amount of kinetic energy release that increases as the clusters grow. Although the exact energetics and

dynamics cannot be nailed down, the results point toward a phenomenal mixture of multiphoton absorption and conversion of ring strain into explosive dissociation.

References

1. Varandas, A. J. C.; Rocha, C. M. R. C_n(n = 2−4): Current Status. *Phil. Trans. R. Soc. A.* **2018**. *376*, 20170145.
2. Huggins, W. Preliminary Note on the Photographic Spectrum of Comet b. *Proc. R. Soc. Lond.* **1881**, *33*, 1−3.
3. Herzberg, G. *The Spectra and Structures of Simple Free Radicals*, Cornell University Press, Ithaca, NY, 1971.
4. Hinkle, K. W.; Keady, J. J.; Bernath, P. F. Detection of C_3 in the Circumstellar Shell of IRC+10216. *Science*, **1988**, *241*, 1319−1322.
5. Bernath, P. F.; Hinkle, K. W.; Keady, J. J. Detection of C_5 in the Circumstellar Shell of IRC+10216. *Science*, **1989**, *244*, 562−564.
6. Lara, L. M.; Lin, Z. Y.; Rodrigo, R.; Ip, W. H. 67P/Churyumov-Gerasimenko Activity Evolution During its Last Perihelion Before the Rosetta Encounter. *Astron. Astrophys.* **2011**, *525*, A36.
7. Douglas, A. E. Origin of Diffuse Interstellar Lines. *Nature* **1977**, *269*, 130−132.
8. *Herbig, G. H. The Diffuse Interstellar Bands. Annu. Rev. Astron. Astrophys.* ***1995****, 33, 19–73.*
9. Tielens, A. G. G. M.; Snow, T. P. *The Diffuse Interstellar Bands*, Kluwer Academic Publishers, Dordrecht, The Netherlands, **1995**.
10. Hartquist, T. W.; Williams, D. A., eds., *The Molecular Astrophysics of Stars and Galaxies*, Clarendon Press, Oxford, **1998**.
11. Kirkwood, D. A.; Linnartz, H.; Grutter, M.; Dopfer, O.; Motylewski, C. T.; Pachkov, M.; Tulej, M.; Wyss, M.; Maier, J. P. Electronic Spectroscopy of Carbon Chains and

Relevance to Astrophysics. *Faraday Disc.* **1998**, *109*, 109−119.

12. Thaddeus, P.; McCarthy, M. C. Carbon Chains and Rings in the Laboratory and in Space. *Spectrochimica Acta A.* **2001**, *57A*, 757−774.

13. Maier, J. P.; Walker, G. A. H.; Bohlender, D. A. On the Possible Role of Carbon Chains as Carriers of Diffuse Interstellar Bands. *Astrophys. J.* **2004**, *602*, 286−290.

14. Zack, L. N.; Maier, J. P. Laboratory Spectroscopy of Astrophysically Relevant Carbon Species. *Chem. Soc. Rev.* **2014**, *43*, 4602−4614.

15. Cami, J.; Bernard-Salas, J.; Peeters, E.; Malek, S. Detection of C_{60} and C_{70} in a Young Planetary Nebula. *Science* **2010**, *329*, 1180−1182.

16. Campbell, E. K.; Holz, M.; Gerlich, D.; Maier, J. P. Laboratory Confirmation of C_{60}^+ as the Carrier of Two Diffuse Interstellar Bands. *Nature* **2015**, *523*, 322−323.

17. Walker, G. A. H.; Bohlender, D. A.; Maier, J. P.; Campbell, E. K. Identification of More Interstellar C_{60}^+ Bands. *Astrophys. J. Lett*. **2015**, *812*, L8.

18. Strelnikov, D.; Kern, B.; Kappes, M. M. On observing C_{60}^+ and C_{60}^{2+} in Laboratory and Space. *Astron. Astrophys.* **2015**, *584*, A55.

19. Omont, A. Interstellar Fullerene Compounds and Diffuse Interstellar Bands. *Astron. Astrophys.* **2016**, *590*, A52.

20. Campbell, E. K.; Maier, J. P. Perspective: C_{60}^+ and Laboratory Spectroscopy Related to Diffuse Interstellar Bands. *J. Chem. Phys.* **2017**, *146*, 160901.

21. Cox, N. L. J.; Patat, F. Dense Molecular Clouds in the SN 2008 fp Host Galaxy. *Astron. Astrophys.* **2014**, *565*, A61−A71.

22. Cernicharo, J.; Goicoechea, J. R.; Benilan, Y. A New Infrared Band in Interstellar and Circumstellar Clouds: C_4 or C_4H? *Astrophys. J.* **2002**, *580*, L157.

23. Wakelam, V.; Loison, J. C.; Herbst, E.; Talbi, D.; Quan, D.; Caralp, F. A Sensitivity Study of the Neutral-Neutral Reactions C + C_3 and C + C_5 in Cold Dense Interstellar Clouds. *Astron. Astrophys.* **2009**, *495*, 513–521.

24. *Maier, J. P.; Lakin, N. M.; Walker, G. A. H.; Bohlender, D. A. Detection of C3 in Diffuse Interstellar Clouds. Astrophys. J.* ***2001****, 553, 267–273.*

25. Souza, S. P.; Luts, B. L. Detection of C_2 in the Interstellar Spectrum of Cygnus OB2 Number 12 (IV Cygni Number 12). *Asrtophys. J.* **1977**, *216*, 49-51.

26. Kroto, H. W.; Heath, J. R.; O'Brien, S. C.; Curl, R. F.; Smalley, R. E. C_{60}: Buckminsterfullerene. *Nature* **1985**, *318*, 162–163.

27. Curl, R. F.; Smalley, R. E. Probing C_{60}. *Science* **1988**, *242*, 1017–1022.

28. Dresselhaus, M. S.; Dresselhaus, G.; Eklund, P. C. *Science of Fullerenes and Carbon Nanotubes*, Academic Press, San Diego, 1996.

29. Weltner, W., Jr., Van Zee, R. J. Carbon Molecules, Ions, and Clusters. *Chem. Rev*. **1989**, *89*, 1713–1737.

30. Van Orden, A.; Saykally, R. J. Small Carbon Clusters: Spectroscopy, Structure, and Energetics. *Chem. Rev.* **1998**, *98*, 2313–2357.

31. Swan, W. On the Prismatic Spectra of the Flames of Compounds of Carbon and Hydrogen. *Trans. R. Soc. Edinburgh.* **1857**, *21*, 411–429

32. Koinuma, H.; Horiuchi, T.; Inomata, K.; Ha, H. K.; Nakajima, K.; Chaudhary, K. A. Synthesis of Carbon Clusters and Thin Films by Low Temperature Plasma Chemical Vapor Deposition Under Atmospheric Pressure. *Pure Appl. Chem.* **1996**, *68*, 1151–1154.

33. Martin, J. M. L.; François, J. P.; Gijbels, R. On the Geometrical Structure of the C_3^+ Cation - An *ab initio* Study. *J. Chem. Phys.* **1990**, *93*, 5037–5045.

34. Watts, J. D.; Stanton, J. F.; Gauss, J.; Bartlett, R. J. A Coupled-Cluster Study of the Ground-State of C_3^+. *J. Chem. Phys.* **1991**, *94*, 4320–4327.

35. Giuffreda, M. G.; Deleuze, M. S.; François, J.-P. Structural, Rotational, Vibrational, and Electronic Properties of Ionized Carbon Clusters C_n^+ (n = 4–19). *J. Phys. Chem. A* **1999**, *103*, 5137–5151.

36. Deleuze, M. S.; Giuffreda, M. G.; François, J.-P.; Cederbaum, L. S. Valence One-Electron and Shake-Up Ionization Bands of Carbon Clusters. I. The C_n (n = 3, 5, 7, 9) Chains. *J. Chem. Phys.* **1999**, *111*, 5851–5865.

37. Deleuze, M. S.; Giuffreda, M. G.; François, J.-P.; Cederbaum, L. S. Valence One-Electron and Shake-Up Ionization Bands of Carbon Clusters. II. The C_n (n = 4, 6, 8, 10) Rings. *J. Chem. Phys.* **2000**, *112*, 5325–5338.

38. Boggio-Pasqua, M.; Voronin, A.I.; Halvick, P.; Rayez, J.C. Analytical Representations of High Level *ab initio* Potential Energy Curves of the C_2 Molecule. *J. Mol. Struct.: THEOCHEM*. **2000**, *531*,159–167.

39. Haubrich, J.; Mühlhaüser, M.; Peyerimhoff, S. D. The Electronic Spectrum of Linear and Cyclic C_6^+. A Theoretical Study. *Phys. Chem. Chem. Phys.* **2002**, *4*, 2891–2896.

40. Deleuze, M. S.; Giuffreda, M. G.; François, J.-P. Valence One-Electron and Shake-Up Ionization Bands of Carbon Clusters. III. The C_n (n = 5, 7, 9, 11) Rings. *J. Phys. Chem. A* **2002**, *106*, 5626–5637.

41. Orlova, G.; Goddard, J. D. Is Density Functional Theory Free of Spatial Symmetry Breaking? The Case of the Linear Carbon Radical Cations: C_3^+, C_5^+, C_7^+ and C_9^+. *Chem. Phys. Lett.* **2002**, *363*, 486–491.

42. Terentyev, A.; Scholz, R.; Schreiber, M.; Seifert, G. Theoretical Investigation of Excited

States of C_3. *J. Chem. Phys.* **2004**, *121*, 5767–5776.

43. Ahmed, K.; Balint-Kurti, G. G.; Western, C. M. *Ab initio* Calculations and Vibrational Energy Level Fits for the Lower Singlet Potential-Energy Surfaces of C_3. *J. Chem. Phys.* **2004**, *121*, 10 041–10 051.

44. Varandas, A. J. C. Extrapolation to the Complete-Basis-Set Limit and the Implications of Avoided Crossings: the $X^1\Sigma_g^+$, $B^1\Delta_g$, and $B'^1\Sigma_g^+$ States of C_2. *J. Chem. Phys.* **2008**, *129*, 234 103–234 116.

45. Varandas, A. J. C. A Simple, Yet Reliable, Direct Diabatization Scheme. The $^1\Sigma_g^+$ States of C_2. *Chem. Phys. Lett.* **2009**, *471*, 315–321.

46. Rocha, C. M. R.; Varandas, A. J. C. Accurate *ab initio*-Based Double Many-Body Expansion Potential Energy Surface for the Adiabatic Ground-State of the C_3 Radical Including Combined Jahn-Teller Plus Pseudo-Jahn-Teller Interactions. *J. Chem. Phys.* **2015**, *143*, 074 302–074 318.

47. Jin, Y.; Perera, A.; Lotrich, V. F.; Bartlett, R. J. Coupled Cluster Geometries and Energetics of C_{20} Carbon Cluster Isomers – A New Benchmark Study. *Chem. Phys. Lett.* **2015**, *629*, 76–80.

48. Rocha, C. M. R.; Varandas, A. J. C. The Jahn-Teller Plus Pseudo-Jahn-Teller Vibronic Problem in the C_3 Radical and its Topological Implications. *J. Chem. Phys.* **2016,** *144*, 064 309–064 324.

49. Weltner, W., Jr., Van Zee, R. J. Matrix-Isolated Polycarbon Molecules. *J. Molec. Struc.* **1990**, *222*, 201–207.

50. Maier, J. P. Electronic Spectroscopy of Carbon Chains. *J. Phys. Chem. A* **1998**, *102*, 3462–3469.

51. Lifshitz, C. Carbon Clusters. *Int. J. Mass Spectrom.* **2000**, *200*, 423–442.

52. Rohlfing, E. A.; Cox, D. M.; Kaldor, A. Production and Characterization of Supersonic Carbon Cluster Beams. *J. Chem. Phys.* **1984**, *81*, 3322–3330.

53. Geusic, M. E.; McIlrath, T. J.; Jarrold, M. F.; Bloomfield, L. A.; Freeman, R. R.; Brown, W. L. Photofragmentation of Mass-Resolved Carbon Cluster Ions: Observation of a "Magic" Neutral Fragment. *J. Chem. Phys.* **1986**, *84*, 2421–2422.

54. Geusic, M. E.; Jarrold, M. F.; McIlrath, T. J.; Freeman, R. R.; Brown, W. L. Photodissociation of Carbon Cluster Cations. *J. Chem. Phys.* **1987**, *86*, 3862–3869.

55. O'Brien, S. C.; Heath, J. R.; Curl, R. F.; Smalley, R. E. Photophysics of Buckminsterfullerene and Other Carbon Cluster Ions. *J. Chem. Phys.* **1988**, *88*, 220–230.

56. Radi, P. P.; Bunn, T. L.; Kemper, P. R.; Molchan, M. E.; Bowers, M. T. A New Method for Studying Carbon Clusters in the Gas Phase: Observation of Size Specific Neutral Fragment Loss from Metastable Reactions of Mass Selected C_n^+, n < 60. *J. Chem. Phys.* **1988**, *88*, 2809–2814.

57. Sowa, M. B.; Hintz, P. A.; Anderson, S. L. Dissociation Energies for Carbon Cluster Ions ($C_{2\text{-}15}^+$): A System Where Photodissociation is Misleading. *J. Chem. Phys.* **1991**, *95*, 4719–4720.

58. Bouyer, R.; Roussel, F.; Monchicourt, P.; Perdix, M.; Pradel, P. Energetics of C_{16}^+ to C_{36}^+ Photodissociation. *J. Chem. Phys.* **1994**, *100*, 8912–8919.

59. Pozniak, B. P.; Dunbar, R. C. Photodissociation and Photodetachment of Small Carbon Cluster Anions. *Int. J. Mass Spectrom. Ion Processes* **1994**, *133*, 97–110.

60. Sowa-Resat, M. B.; Hintz, P. A.; Anderson, S. L. Dissociation Energies for Small Carbon Cluster Ions ($C_{2\text{-}19}^+$) Measured by Collision-Induced Dissociation. *J. Phys. Chem.*

1995, *99*, 10736–10741.

61. Pozniak, B. P.; Dunbar, R. C. Photodissociation Studies of C_n^+ at 193 nm (n = 5–19). *Int. J. Mass Spectrom. Ion Processes* **1997**, *165/166*, 299–313.

62. Gluch, K.; Matt-Leubner, S.; Echt, O.; Concina, B.; Scheier, P.; Mark, T. D. High-Resolution Kinetic Energy Release Distributions and Dissociation Energies for Fullerene Ions C_n^+, $42 \leq n \leq 90$. *J. Chem. Phys.* **2004**, *121*, 2137–2143.

63. Concina, B.; Gluch, K.; Matt-Leubner, S.; Echt, O.; Scheier, P.; Mark, T. D. Metastable Fractions and Dissociations Energies for Fullerene Ions C_n^+, $42 \leq n \leq 70$. *Chem. Phys. Lett.* **2005**, *407*, 464–470.

64. von Helden, G.; Hsu, M. T.; Kemper, P. R.; Bowers, M. T. Structures of Carbon Cluster Ions from 3 to 60 Atoms: Linears to Rings to Fullerenes. *J. Chem. Phys.* **1991**, *95*, 3835–3837.

65. von Helden, G.; Hsu, M. T.; Gotts, N. G.; Bowers, M. T. Carbon Cluster Cations with up to 84 Atoms: Structures, Formation Mechanism, and Reactivity. *J. Phys. Chem.* **1993**, *93*, 8182–8192.

66. von Helden, G.; Gotts, N. G.; Bowers, M. T. Annealing of Carbon Cluster Cations: Rings to Rings and Rings to Fullerenes. *J. Am. Chem. Soc.* **1993**, *115*, 4363–4364.

67. Ramanathan, R.; Zimmerman, J. A.; Eyler, J. R. Ionization Potentials of Small Carbon Clusters. *J. Chem. Phys.* **1993**, *98*, 7838–7845.

68. Shvartsburg, A. A.; Hudgins, R. R.; Dugourd, P.; Gutierrez, R.; Frauenheim, T.; Jarrold, M. F. Observation of "Stick" and "Handle" Intermediates along the Fullerene Road. *Phys. Rev. Lett.* **2000**, *84*, 2421–2424.

69. Belau, L.; Wheeler, S. E.; Ticknor, B. W.; Ahmed, M.; Leone, S. R.; Allen, W. D.;

Schaefer, H. F.; Duncan, M. A. Ionization Thresholds of Small Carbon Clusters: Tunable VUV Experiments and Theory. *J. Am. Chem. Soc.* **2007**, *129*, 10229–10243.

70. Koyasu, K.; Ohtaki, T.; Hori, N.; Misaizu, F. Isomer-resolved Dissociation of Small Carbon Cluster Cations, $C_7^+ - C_{10}^+$. *Chem. Phys. Lett.* **2012**, *523*, 54–59.

71. Reedy, E. S.; Rademacher, J.; Szabla, R.; Campbell, E. K. Electronic Absorptions of C_5^+ Detected in the Visible through Action Spectroscopy in a Cryogenic Trap. *Molec. Phys.* **2021**, *119*, e1989070.

72. Buntine, J. T.; Cotter, M. I.; Jacovella, U.; Liu, C.; Watkins, P.; Carrascosa, E.; Bull, J. N.; Weston, L.; Muller, G.; Scholz, M. S.; Bieske, E. J. Electronic Spectra of Positively Charged Carbon Clusters – C_{2n}^+ (n = 6–14). *J. Chem. Phys.* **2021**, *155*, 214302.

73. Rademacher, J.; Reedy, E. S.; Campbell, E. K. Electronic Spectroscopy of Monocyclic Carbon Ring Cations for Astrochemical Consideration. *J. Phys. Chem. A* **2022**, DOI: 10.1021/acs.jpca.2c00650, in press.

74. Cornett, S.; Peschke, M.; LaiHing, K.; Cheng, P. Y.; Willey, K. F.; Duncan, M. A. Reflectron Time-of-Flight Mass Spectrometer for Laser Photodissociation. *Rev. Sci. Instrum.* **1992**, *63*, 2177–2186.

75. Duncan, M. A. Laser Vaporization Cluster Sources. *Rev. Sci. Instrum.* **2012**, *83*, 041101.

76. Eppink, A. T. J. B.; Parker, D. H. Velocity Map Imaging of Ions and Electrons using Electrostatic Lenses: Application in Photoelectron and Photofragment Ion Imaging of Molecular Oxygen. *Rev. Sci. Instrum.* **1997**, *68*, 3477–3484.

77. Suits, A. G. Invited Review Article: Photofragment Imaging. *Rev. Sci. Instrum.* **2018**, *89*, 111101.

78. Townsend, D.; Minitti, M. P.; Suits, A. G. Direct Current Slice Imaging. *Rev. Sci.*

Instrum. **2003**, *74*, 2530–2539.

79. Li, W.; Chambreau, S. D.; Lahankar, S. A.; Suits, A. G. Megapixel Ion Imaging with Standard Video. *Rev. Sci. Instrum.* **2005**, *76*, 063106. See also NuAcq 0.9 software: Suits, A.G., http://faculty.missouri.edu/suitsa/NuAcq.html.

80. Maner, J. A.; Mauney, D. T.; Duncan, M. A. Imaging Charge Transfer in a Cation-π System: Velocity-Map Imaging of Ag^+(Benzene) Photodissociation. *J. Phys. Chem. Lett.* **2015**, *6*, 4493−4498.

81. Maner, J. A.; Mauney, D. T.; Duncan, M. A. Velocity Map Ion Imaging of Ar_2^+ Photodissociation. *Chem. Phys. Lett.* **2017**, *671*, 182–185.

82. Rittgers, B. M.; Leicht, D.; Duncan, M. A. Cation-π Complexes of Silver Studied with Photodissociation and Velocity-Map Imaging. *J. Phys. Chem. A* **2020**, *124*, 9166–9176.

83. M. J. Frisch, G. W. Trucks, H. B. Schlegel, G. E. Scuseria, M. A. Robb, J. R. Cheeseman, G. Scalmani, V. Barone, G. A. Petersson, H. Nakatsuji, X. Li, M. Caricato, A. V. Marenich, J. Bloino, B. G. Janesko, R. Gomperts, B. Mennucci, H. P. Hratchian, J. V. Ortiz, A. F. Izmaylov, J. L. Sonnenberg, D. Williams-Young, F. Ding, F. Lipparini, F. Egidi, J. Goings, B. Peng, A. Petrone, T. Henderson, D. Ranasinghe, V. G. Zakrzewski, J. Gao, N. Rega, G. Zheng, W. Liang, M. Hada, M. Ehara, K. Toyota, R. Fukuda, J. Hasegawa, M. Ishida, T. Nakajima, Y. Honda, O. Kitao, H. Nakai, T. Vreven, K. Throssell, J. A. Montgomery, Jr., J. E. Peralta, F. Ogliaro, M. J. Bearpark, J. J. Heyd, E. N. Brothers, K. N. Kudin, V. N. Staroverov, T. A. Keith, R. Kobayashi, J. Normand, K. Raghavachari, A. P. Rendell, J. C. Burant, S. S. Iyengar, J. Tomasi, M. Cossi, J. M. Millam, M. Klene, C. Adamo, R. Cammi, J. W. Ochterski, R. L. Martin, K. Morokuma, O. Farkas, J. B. Foresman, and D. J. Fox, Gaussian 16 Revision C.01, Gaussian, Inc.,

Wallingford CT, 2016.

84. Hunter, J.; Fye, J.; Jarrold, M. F. Annealing C_{60}^{+}: Synthesis of Fullerenes and Large Carbon Rings. *Science* **1993**, *260*, 784–786.

85. Hunter, J.; Fye, J.; Jarrold, M. F. Carbon Rings. *J. Phys. Chem.* **1993**, *97*, 3460–3462.

86. Shelimov, K. B.; Hunter, J. M.; Jarrold, M. F. Small Carbon Rings: Dissociation, Isomerization, and a Simple Model Based on Strain. *Int. J. Mass Spectrom. Ion Proc.* **1994**, *138*, 17–31.

CHAPTER 6

CONCLUSION

The research presented in this dissertation gives a few examples of the types of studies that can be done with photofragment imaging of mass-selected cations. Very few cationic systems have well-known binding energies. This work demonstrates the capability of putting upper limits on the dissociation energy in these types of systems, which is good as a benchmark for theoretical work and for comparing other experiments in thermochemistry. Photofragment imaging is also able to measure the angular distributions of photofragments simultaneously with their velocity distributions. This makes it an excellent experiment for studying the photodissociation dynamics in cations, neutrals, or anions.

The work in Chapter 3 presents the photodissociation dynamics in silver cation−π systems. The angular distributions for the photodissociation of Ag^+(benzene), Ag^+(toluene), and Ag^+(furan) at various wavelengths. Upper limits on the metal-ligand binding energy were also determined. The tightest upper limit placed on the bond energy for Ag^+(benzene) was determined to be 28.9 ± 3.5 kcal/mol. The limits placed on the Ag^+(toluene) and Ag^+(furan) complexes were 35.9 ± 3.5 kcal/mol and 26.3 ± 3.5 kcal/mol, respectively. There is the possibility of having two isomers of Ag^+(furan) in the experiment, and will likely take an infrared spectroscopy experiment to confirm this.

The zinc-methanol cation cluster was investigated in the Chapter 4. All of the images presented for this cluster were isotropic in nature. This is likely due to the asymmetry in the complex, but may also be due to predissociation allowing for rotation of the parent and washing

out any anisotropy. The maximum kinetic energy release values were relatively high compared to the silver complexes, with much less signal concentrated in the center. This indicates a significant amount of excess energy being transferred into translation of the fragments. However, the kinetic energy release distribution was quite large, indicating that some excess energy also went to the internal excitation of the fragments. An upper limit of 33.42 ± 4.15 kcal/mol was placed on the dissociation energy of this complex from the image of CH_3OH^+ at 266 nm. Imaging of the Zn^+ fragment produced the greatest amount of kinetic energy release, however it was less than might be expected based on the known transitions and the theoretical calculations on binding energy. This suggests there could be interesting excited state dynamics that we are not aware of, but would require a different experiment to uncover.

Studies on the photodissociation dynamics of various carbon cluster cations were reported in Chapter 5. These studies are qualitative in nature because of the multiphoton absorption exhibited in the clusters. However, the results were quite surprising and suggest that strain built up in cyclic carbon clusters might be released during photodissociation, resulting in a greater amount of KER than would otherwise be detected. This work presents an example of photofragment imaging shedding light on the different photodissociation dynamics in similar clusters, even when the exact amount of energy put into the system is unknown.

This dissertation was also written as a starting point for the graduate student interested in the photofragment imaging of mass-selected cations, and it shows just a few flavors of systems that can be studied. Most cations have not been studied by this technique and the thermochemistry on many of them is totally unknown. An example of an extremely interesting system that could be studied with this technique is doubly charged metal-water complexes. A schematic of the potential energy surfaces of such a system is shown in Figure 6.1. A fascinating

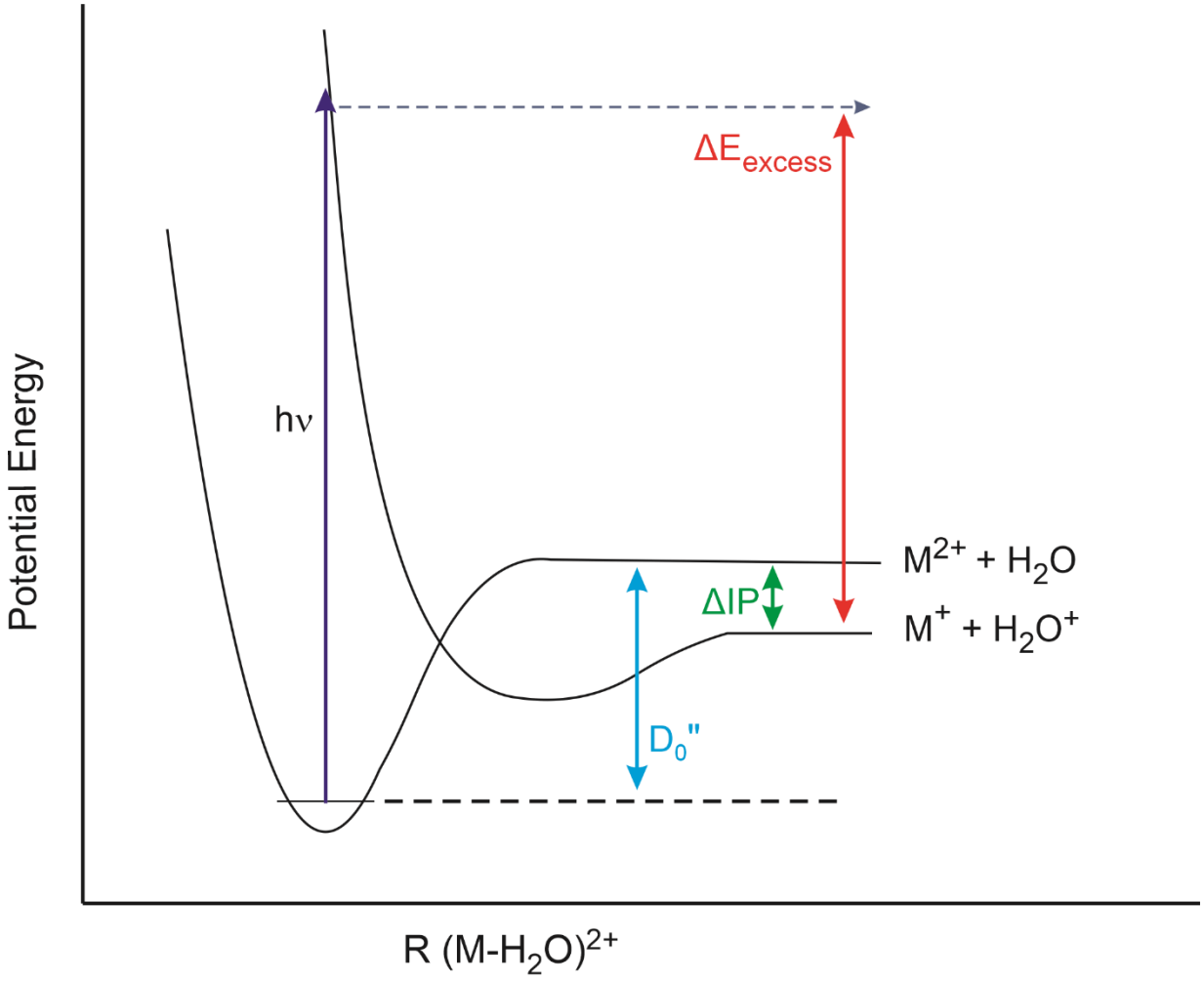

Figure 6.1. Schematic diagram showing the ground and excited charge transfer state in a doubly charged metal-water complex.

aspect of some of these complexes is that the 2+ charge is localized on the metal atom even though the second ionization potential is higher than that of water. With a high enough energy photon, the charge transfer state should be accessible and dissociation would lead to a singly charged metal atom and a singly charged water molecule as fragments. This would also lead to *adding* the ΔIP in the energetic cycle instead of subtracting to find an upper limit on the dissociation energy. It would also be very impactful to learn about the thermochemistry of doubly charged metal-water complexes since many metal atoms exist in this oxidation state in solution. There are many other systems that would be interesting to study with photofragment imaging, such as noble metal dimer and trimer cations, aluminum cation-(ethylene, propene, or butene), or vanadium oxide (V_nO_m) cation clusters, just to name a few.

APPENDIX A

COMPUTATIONAL CHEMISTRY AND IMAGE ANALYSIS

OF SILVER CATION-π COMPLEXES

Geometry Optimizations

Ag^+(benzene)

B3LYP/Def2TZVP

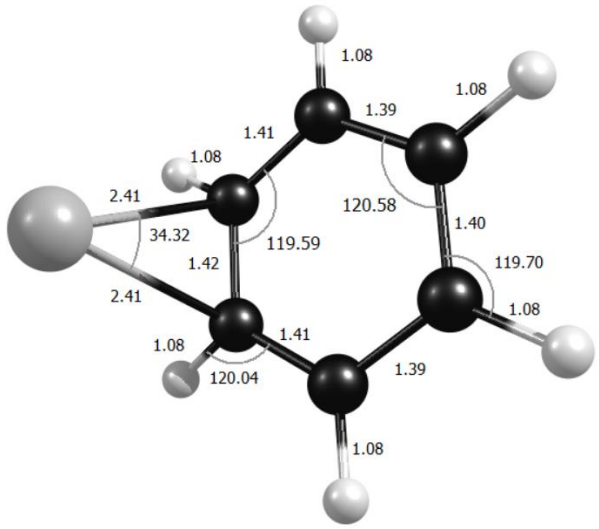

Coordinates:

Ag	-3.954172000	-4.009443000	1.549346000
C	-5.310836000	-2.025712000	1.388959000
C	-6.484749000	-2.325056000	2.100660000
C	-4.131566000	-1.667682000	2.098497000
H	-7.389206000	-2.573120000	1.561184000
H	-3.266517000	-1.302015000	1.556603000
C	-6.491832000	-2.242004000	3.485426000
C	-4.154875000	-1.617417000	3.502257000
H	-7.406029000	-2.438971000	4.029813000
H	-3.265392000	-1.320782000	4.042099000
C	-5.332764000	-1.889815000	4.182687000
H	-5.357820000	-1.816535000	5.262000000
H	-5.340231000	-1.930338000	0.309247000

B3LYP/Def2QZVP

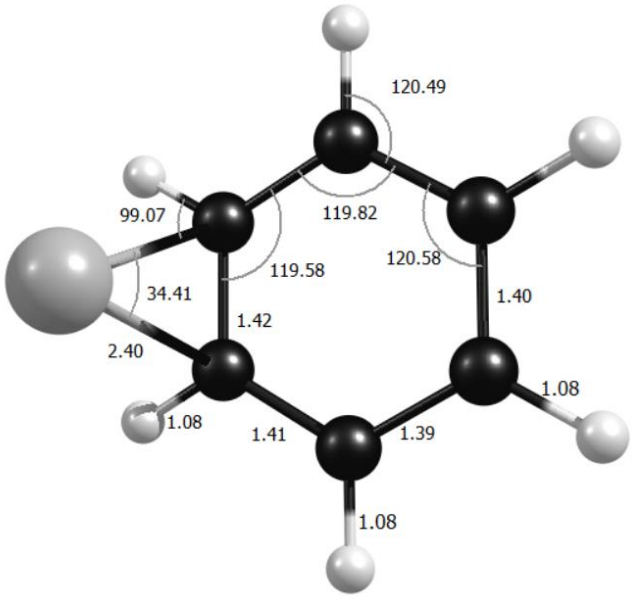

Coordinates:

Ag	-3.956477000	-4.003843000	1.555160000
C	-5.310730000	-2.026123000	1.388813000
C	-6.484372000	-2.324581000	2.100549000
C	-4.131697000	-1.668447000	2.098038000
H	-7.387172000	-2.573523000	1.561811000
H	-3.268228000	-1.301762000	1.557284000
C	-6.491254000	-2.242018000	3.484749000
C	-4.155203000	-1.617868000	3.501504000
H	-7.404004000	-2.439181000	4.028418000
H	-3.266384000	-1.323241000	4.040438000
C	-5.332456000	-1.890344000	4.181747000
H	-5.357164000	-1.817962000	5.259574000
H	-5.340845000	-1.929997000	0.310693000

M06L/Def2TZVP

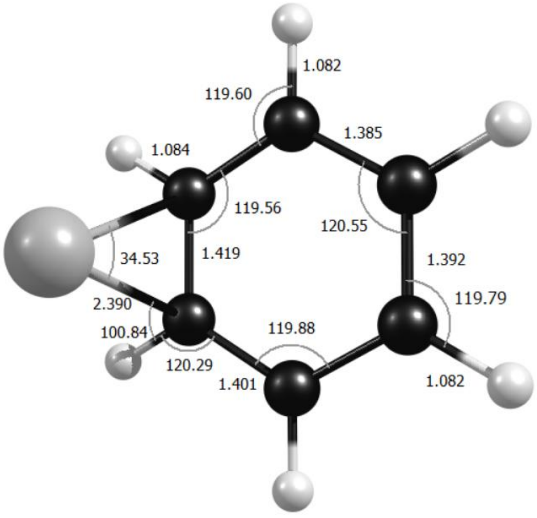

Coordinates:

Ag	-4.013605000	-3.992025000	1.651544000
C	-5.312584000	-2.003099000	1.382993000
C	-6.477375000	-2.319224000	2.093600000
C	-4.136110000	-1.646410000	2.090831000
H	-7.380827000	-2.570408000	1.554117000
H	-3.267627000	-1.291656000	1.547674000
C	-6.480458000	-2.255173000	3.477545000
C	-4.154708000	-1.615805000	3.491024000
H	-7.391183000	-2.467811000	4.021298000
H	-3.263935000	-1.323706000	4.031023000
C	-5.325712000	-1.905660000	4.172260000
H	-5.344882000	-1.848609000	5.252389000
H	-5.336982000	-1.919302000	0.302477000

M06L/Def2QZVP

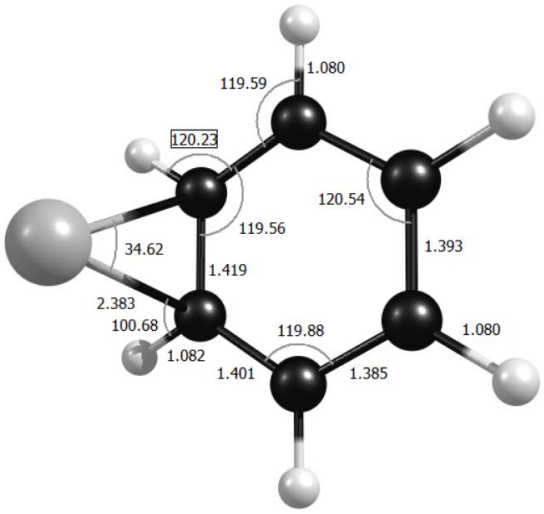

Coordinates:

Ag	-4.010512000	-3.985852000	1.643729000
C	-5.312441000	-2.005435000	1.383505000
C	-6.478082000	-2.319263000	2.094267000
C	-4.135829000	-1.648696000	2.091195000
H	-7.379026000	-2.571917000	1.555906000
H	-3.269024000	-1.294137000	1.549800000
C	-6.481455000	-2.253732000	3.478232000
C	-4.154838000	-1.615640000	3.491606000
H	-7.390193000	-2.465581000	4.021095000
H	-3.265211000	-1.326015000	4.030168000
C	-5.326178000	-1.904050000	4.173064000
H	-5.345403000	-1.846822000	5.250902000
H	-5.337797000	-1.921749000	0.305308000

Ag^+(toluene) Isomer 1

B3LYP/Def2TZVP

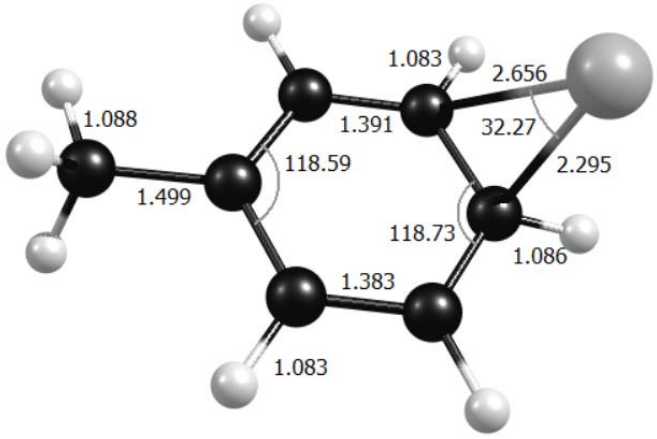

Coordinates:

Ag	1.849844000	-0.005748000	-0.422098000
H	-1.431677000	-1.320960000	1.760431000
C	-3.191267000	-0.936785000	-0.290228000
H	-3.409123000	-1.681287000	0.473052000
H	-3.088304000	-1.451307000	-1.249213000
H	-4.051932000	-0.270846000	-0.378723000
C	-1.949793000	-0.158827000	0.028597000
C	-1.571232000	0.929970000	-0.775055000
C	-0.447746000	1.683513000	-0.486627000
C	0.348083000	1.365851000	0.641677000
C	-0.020501000	0.256174000	1.445744000
C	-1.149552000	-0.490553000	1.125930000
H	-2.186742000	1.200252000	-1.624239000
H	-0.205202000	2.553107000	-1.083851000
H	1.081674000	2.079039000	1.005222000
H	0.531208000	0.045019000	2.353460000

B3LYP/Def2QZVP

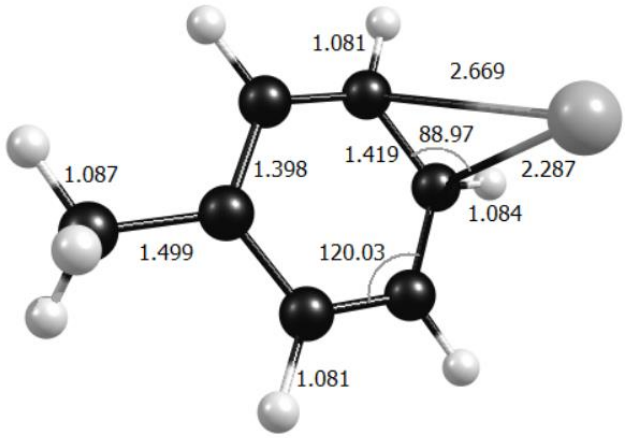

Coordinates:

Ag	1.833108000	0.026036000	-0.473714000
H	-1.425708000	-1.332407000	1.749351000
C	-3.190735000	-0.935525000	-0.289765000
H	-3.483020000	-1.584480000	0.531675000
H	-3.028833000	-1.561340000	-1.170153000
H	-4.022178000	-0.270969000	-0.521200000
C	-1.952214000	-0.154485000	0.032430000
C	-1.577967000	0.940549000	-0.762521000
C	-0.452119000	1.690173000	-0.472768000
C	0.351116000	1.359421000	0.646490000
C	-0.014050000	0.242369000	1.441072000
C	-1.145867000	-0.497770000	1.121957000
H	-2.197980000	1.220374000	-1.603215000
H	-0.213929000	2.565817000	-1.060123000
H	1.083532000	2.069219000	1.014715000
H	0.544582000	0.019628000	2.339846000

M06L/Def2TZVP

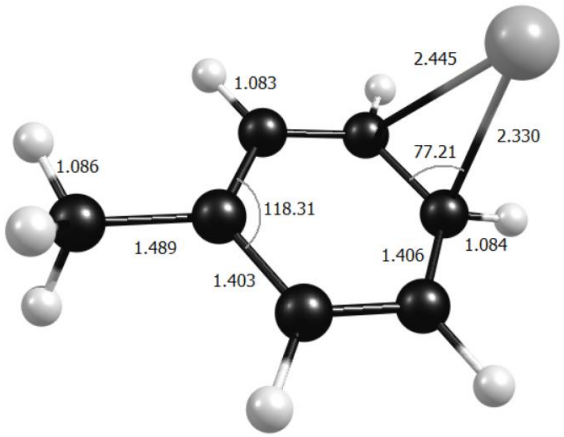

Coordinates:

Ag	1.691129000	-0.267964000	-0.230257000
H	-1.386949000	-1.313267000	1.738533000
C	-3.156487000	-0.944591000	-0.296670000
H	-3.271626000	-1.801418000	0.361066000
H	-3.144593000	-1.300575000	-1.326655000
H	-4.046906000	-0.322876000	-0.197286000
C	-1.931977000	-0.157133000	0.016605000
C	-1.574750000	0.942096000	-0.778160000
C	-0.465759000	1.713679000	-0.495116000
C	0.329771000	1.418697000	0.625505000
C	-0.011341000	0.301705000	1.429702000
C	-1.124610000	-0.474468000	1.106108000
H	-2.196404000	1.199845000	-1.627004000
H	-0.229522000	2.575408000	-1.105427000
H	1.096581000	2.111433000	0.953676000
H	0.531182000	0.116042000	2.349457000

M06L/Def2QZVP

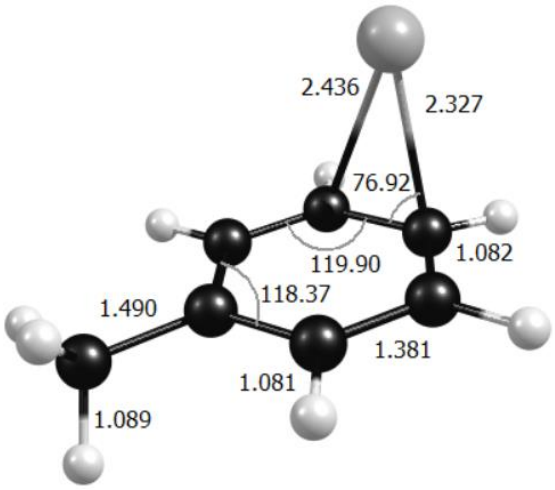

Coordinates:

Ag	1.690774000	-0.269094000	-0.223707000
H	-1.382430000	-1.315543000	1.733734000
C	-3.157225000	-0.944808000	-0.296846000
H	-3.282246000	-1.788409000	0.373094000
H	-3.131353000	-1.318246000	-1.318650000
H	-4.044519000	-0.318788000	-0.220737000
C	-1.932674000	-0.155824000	0.017966000
C	-1.578726000	0.945878000	-0.775176000
C	-0.468699000	1.716702000	-0.493226000
C	0.330724000	1.418007000	0.623801000
C	-0.007952000	0.299149000	1.426533000
C	-1.123291000	-0.476095000	1.104688000
H	-2.201432000	1.204716000	-1.620066000
H	-0.233225000	2.577053000	-1.101711000
H	1.095989000	2.109468000	0.950635000
H	0.534025000	0.112447000	2.343748000

Ag^{+}(toluene) Isomer 2

B3LYP/Def2TZVP

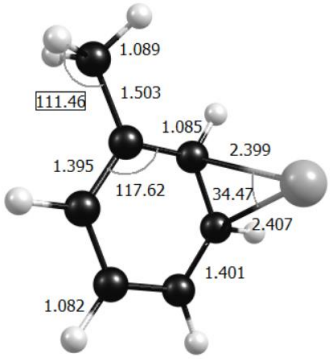

Coordinates:

Ag	1.472048000	-0.695612000	0.040941000
H	-0.596032000	-1.000617000	1.879445000
C	-2.498000000	-1.570334000	-0.009275000
H	-2.068453000	-2.432933000	0.499013000
H	-2.701130000	-1.842249000	-1.045126000
H	-3.460825000	-1.357605000	0.463017000
C	-1.606505000	-0.363982000	0.077777000
C	-1.763255000	0.717394000	-0.789871000
C	-0.990158000	1.871898000	-0.672703000
C	-0.026583000	1.986209000	0.320613000
C	0.149819000	0.930939000	1.225024000
C	-0.635821000	-0.250185000	1.096656000
H	-2.517897000	0.664399000	-1.565125000
H	-1.153441000	2.693418000	-1.358068000
H	0.552633000	2.893340000	0.427718000
H	0.783281000	1.059083000	2.095787000

B3LYP/Def2QZVP

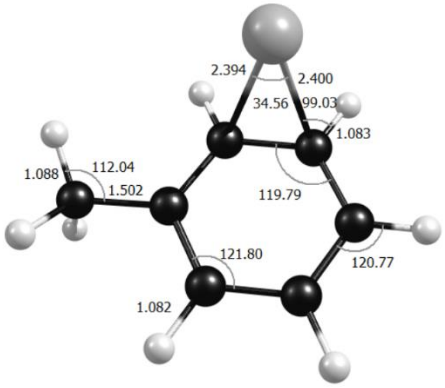

Coordinates:

Ag	1.467355000	-0.688632000	0.044993000
H	-0.599926000	-0.998373000	1.880074000
C	-2.497870000	-1.569843000	-0.009087000
H	-2.059769000	-2.437330000	0.479877000
H	-2.718820000	-1.828448000	-1.042864000
H	-3.450827000	-1.364526000	0.482432000
C	-1.606127000	-0.363750000	0.077472000
C	-1.760660000	0.715762000	-0.791816000
C	-0.987728000	1.869871000	-0.674516000
C	-0.026929000	1.985239000	0.320462000
C	0.148071000	0.931040000	1.226059000
C	-0.637220000	-0.249737000	1.097493000
H	-2.511953000	0.661499000	-1.568039000
H	-1.148547000	2.689119000	-1.360744000
H	0.552585000	2.890436000	0.426764000
H	0.778049000	1.060835000	2.097262000

M06L/Def2TZVP

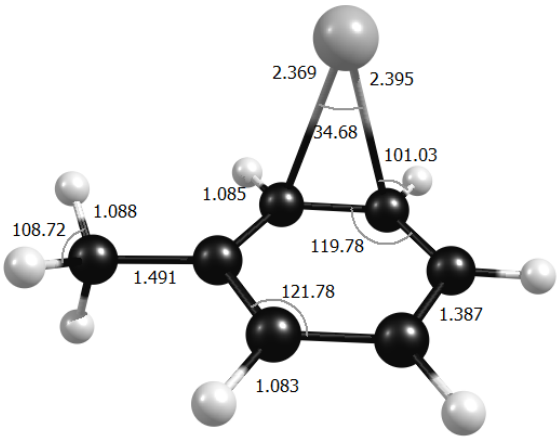

Coordinates:

Ag	-1.038505000	-1.241570000	0.425747000
H	0.034473000	0.694357000	2.119505000
C	-0.107527000	2.605781000	0.176964000
H	-0.925735000	2.618655000	0.893422000
H	-0.487967000	2.918276000	-0.793052000
H	0.606401000	3.367903000	0.494282000
C	0.561598000	1.275302000	0.106928000
C	1.323785000	0.902629000	-0.999311000
C	2.005639000	-0.306449000	-1.044022000
C	1.948150000	-1.194796000	0.019259000
C	1.209648000	-0.853397000	1.154528000
C	0.507654000	0.380620000	1.194528000
H	1.395393000	1.584484000	-1.837862000
H	2.596926000	-0.553257000	-1.915888000
H	2.497683000	-2.125754000	-0.007640000
H	1.249589000	-1.473249000	2.042980000

M06L/Def2QZVP

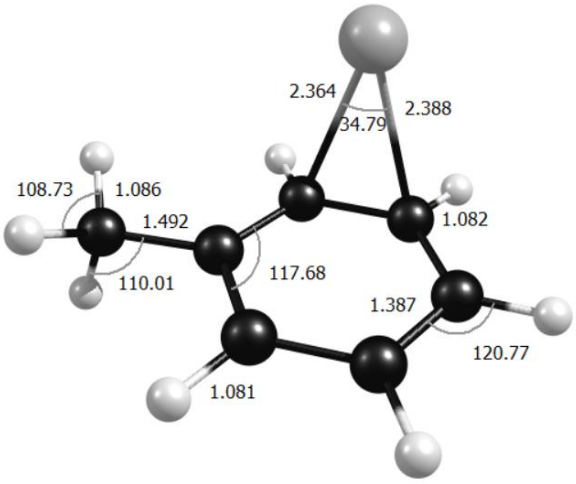

Coordinates:

Ag	1.380090000	-0.660308000	-0.023861000
H	-0.606220000	-0.997652000	1.889939000
C	-2.484370000	-1.563666000	-0.006519000
H	-2.047349000	-2.431810000	0.477706000
H	-2.711773000	-1.817192000	-1.037758000
H	-3.435854000	-1.367168000	0.486525000
C	-1.604101000	-0.362445000	0.085377000
C	-1.746854000	0.710011000	-0.793630000
C	-0.977151000	1.860577000	-0.674343000
C	-0.029119000	1.980385000	0.330734000
C	0.134711000	0.935001000	1.242966000
C	-0.649201000	-0.242685000	1.114578000
H	-2.487392000	0.646494000	-1.578456000
H	-1.126055000	2.674728000	-1.367747000
H	0.553726000	2.882518000	0.435069000
H	0.776595000	1.056373000	2.105242000

Ag^{+}(furan) Isomer 1

B3LYP/Def2TZVP

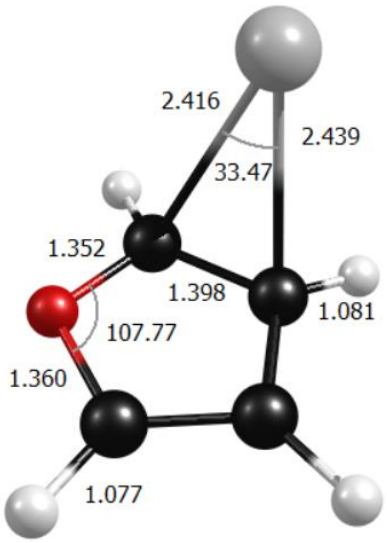

Coordinates:

C	-0.969431000	0.794739000	0.802513000
C	-1.916583000	1.066326000	-0.235114000
C	-2.351405000	-0.142504000	-0.670107000
O	-1.733987000	-1.152923000	-0.001858000
C	-0.889745000	-0.598207000	0.896253000
H	-0.559487000	1.498834000	1.512438000
H	-2.243162000	2.032362000	-0.580725000
H	-3.058589000	-0.443600000	-1.424576000
H	-0.511625000	-1.252445000	1.667078000
Ag	1.179804000	0.112986000	-0.127643000

B3LYP/Def2QZVP

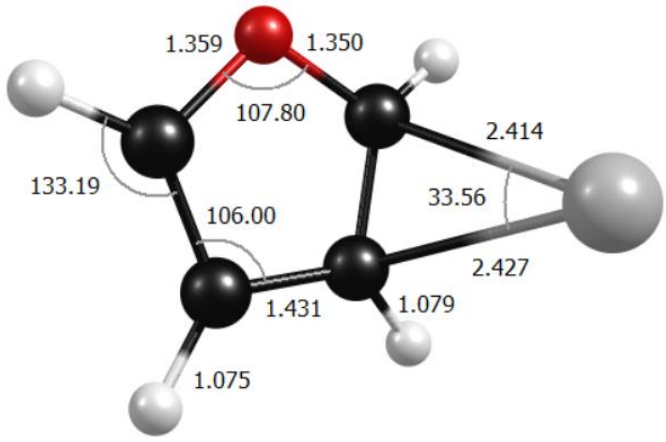

Coordinates:

C	-0.966728000	0.793150000	0.802016000
C	-1.914045000	1.065279000	-0.235962000
C	-2.350523000	-0.142349000	-0.669482000
O	-1.735569000	-1.152742000	0.000492000
C	-0.891113000	-0.599386000	0.897435000
H	-0.559983000	1.496187000	1.512738000
H	-2.237565000	2.030260000	-0.582756000
H	-3.056890000	-0.442638000	-1.422826000
H	-0.513084000	-1.253358000	1.666429000
Ag	1.171291000	0.121167000	-0.129826000

M06L/Def2TZVP

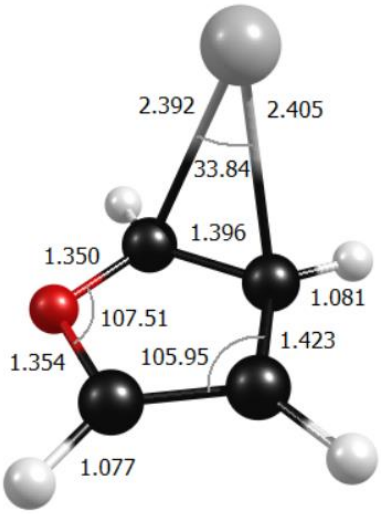

Coordinates:

C	-0.972468000	0.793214000	0.807330000
C	-1.906825000	1.064541000	-0.231616000
C	-2.340179000	-0.142753000	-0.667331000
O	-1.734755000	-1.152610000	0.002201000
C	-0.893509000	-0.597671000	0.899899000
H	-0.552935000	1.495483000	1.513412000
H	-2.228600000	2.029665000	-0.582288000
H	-3.041490000	-0.445387000	-1.426719000
H	-0.516427000	-1.255570000	1.668421000
Ag	1.132976000	0.126657000	-0.145049000

M06L/Def2QZVP

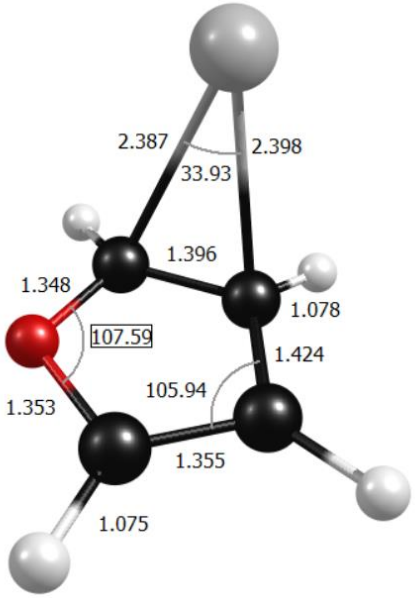

Coordinates:

C	-0.970820000	0.793232000	0.807268000
C	-1.906504000	1.064589000	-0.231466000
C	-2.339607000	-0.142934000	-0.666864000
O	-1.734385000	-1.151303000	0.003041000
C	-0.893803000	-0.597677000	0.900297000
H	-0.553930000	1.495160000	1.511804000
H	-2.226187000	2.027959000	-0.582142000
H	-3.038739000	-0.445323000	-1.424842000
H	-0.516926000	-1.255577000	1.665362000
Ag	1.126692000	0.127443000	-0.144199000

Ag^{+}(furan) Isomer 2

B3LYP/Def2TZVP

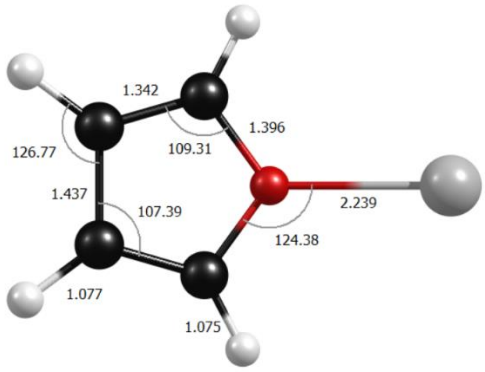

Coordinates:

C	-2.867233000	0.719004000	0.049581000
C	-2.867689000	-0.718145000	0.049387000
C	-1.593746000	-1.119671000	-0.084823000
O	-0.764013000	-0.000209000	-0.177200000
C	-1.593035000	1.119757000	-0.084522000
H	-3.726545000	1.364098000	0.125714000
H	-3.727412000	-1.362713000	0.125344000
H	-1.108017000	-2.076196000	-0.160209000
H	-1.106699000	2.075992000	-0.159651000
Ag	1.419496000	-0.000917000	0.316309000

B3LYP/Def2QZVP

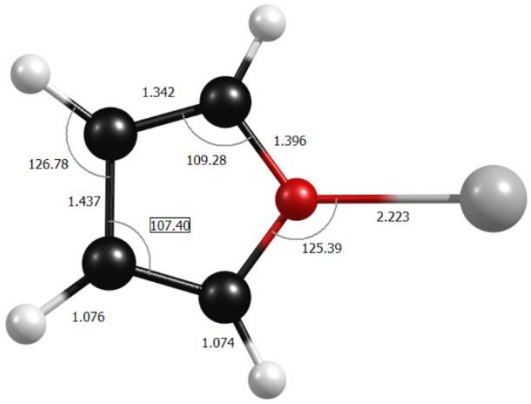

Coordinates:

C	-2.870176000	0.718872000	0.036980000
C	-2.870611000	-0.718032000	0.036746000
C	-1.594467000	-1.119666000	-0.063082000
O	-0.762738000	-0.000191000	-0.131909000
C	-1.593789000	1.119765000	-0.062718000
H	-3.729727000	1.363157000	0.093867000
H	-3.730553000	-1.361815000	0.093424000
H	-1.107143000	-2.074968000	-0.119023000
H	-1.105886000	2.074789000	-0.118350000
Ag	1.430195000	-0.000909000	0.233992000

M06L/Def2TZVP

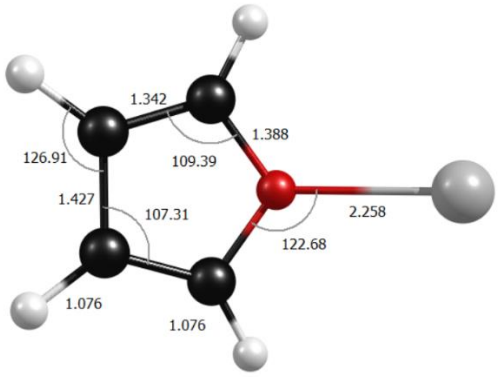

Coordinates:

C	-2.862238000	0.713992000	0.064370000
C	-2.862694000	-0.713139000	0.064177000
C	-1.593398000	-1.112920000	-0.112435000
O	-0.772632000	-0.000203000	-0.236148000
C	-1.592687000	1.113006000	-0.112135000
H	-3.716624000	1.360658000	0.167037000
H	-3.717494000	-1.359287000	0.166665000
H	-1.103395000	-2.065669000	-0.209767000
H	-1.102075000	2.065468000	-0.209214000
Ag	1.388344000	-0.000906000	0.417378000

M06L/Def2QZVP

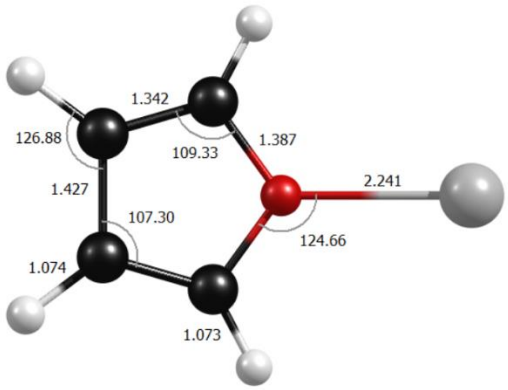

Coordinates:

C	-2.870277000	0.714135000	0.044831000
C	-2.870730000	-0.713272000	0.044640000
C	-1.595028000	-1.112965000	-0.078126000
O	-0.771632000	-0.000208000	-0.163972000
C	-1.594321000	1.113048000	-0.077829000
H	-3.726462000	1.359132000	0.115446000
H	-3.727325000	-1.357744000	0.115080000
H	-1.101689000	-2.063929000	-0.144877000
H	-1.100378000	2.063717000	-0.144326000
Ag	1.422949000	-0.000915000	0.289063000

Table A1: Relative energies (kcal/mol; absolute energies in Hartrees in parentheses) from our computations for Ag^+(benzene), Ag^+(toluene), and Ag^+(furan).

	B3LYP def2-TZVP	def2-QZVP	M06L def2-TZVP	def2-QZVP
Ag^+(benzene)	0.00 (-379.034941)	0.00 (-379.053755)	0.00 (-379.053974)	0.00 (-379.07729)
Ag^+(toluene)				
Isomer 1	0.00 (-418.343998)	0.00 (-418.366098)	0.00 (-418.356490)	0.00 (-418.383053)
Isomer 2	0.83 (-418.342670)	0.83 (-418.364773)	0.46 (-418.355751)	0.45 (-418.382333)
Ag^+(furan)				
Isomer 1	0.00 (-376.842146)	0.00 (-376.859753)	0.00 (-376.865716)	0.00 (-376.886603)
Isomer 2	12.26 (-376.822612)	11.86 (-376.840845)	13.04 (-376.844934)	12.61 (-376.866513)

Kinetic Energy Release and Angular Distribution Analysis

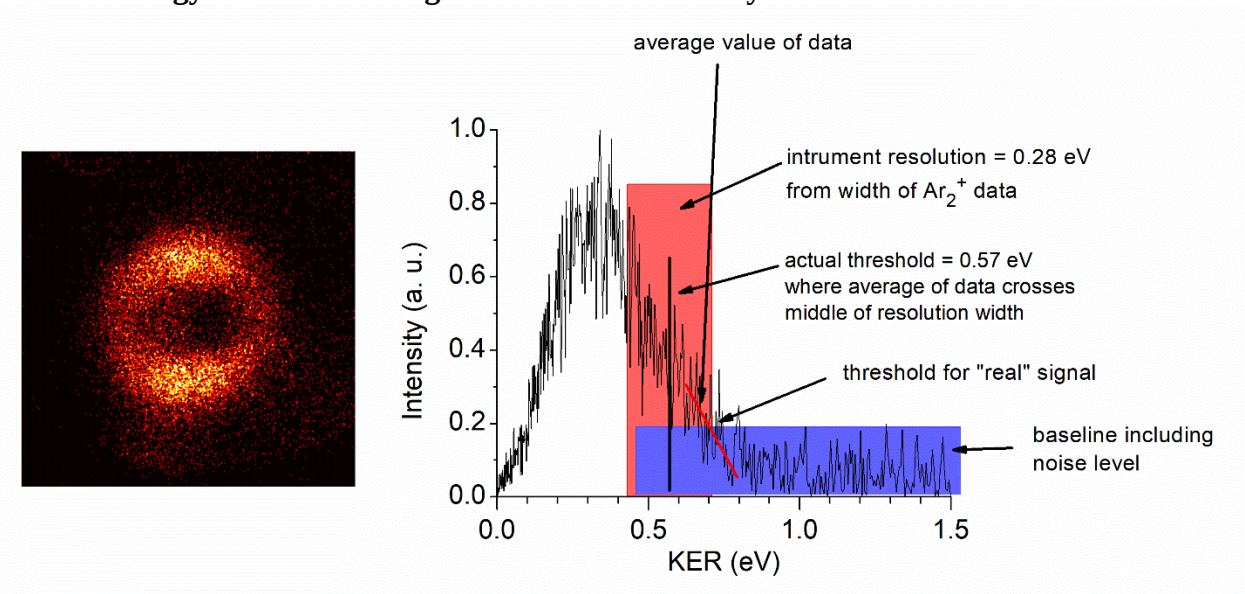

Figure A1: Kinetic energy release (KER) and image of benzene$^+$ from Ag^+(benzene) for photodissociation at 355 nm. The KER graph includes details of how the threshold for maximum kinetic energy release was determined. The blue box includes a section of baseline illustrating the noise level of the experiment outside the boundaries of the image. The red box shows the kinetic energy width of the Ar^+ signal measured from the photodissociation of Ar_2^+ at 355 nm under the same instrument settings. This is judged to be the instrument resolution. We position the high-energy edge of this resolution width box at the point where the signal rises above the baseline. We draw a line through the signal as it approaches the baseline, and select the point where this crosses the mid-point of the resolution width. This is defined as the high-energy outside edge of the image, and is used to define the maximum value of the KER for this image.

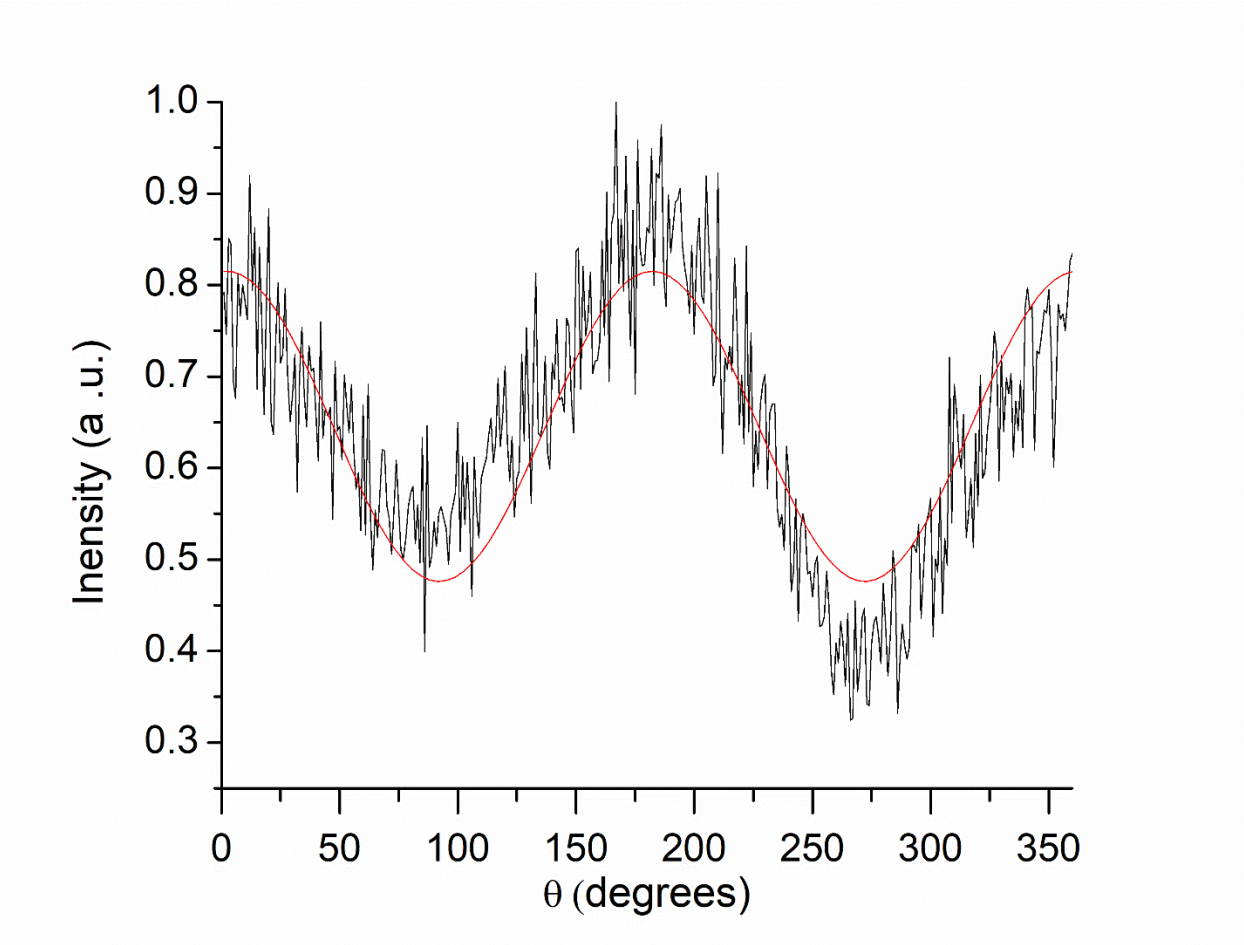

Figure A2: Angular distribution for the image of benzene cation from photodissociation of Ag^+(benzene) at 355 nm. The data was fitted with the below function with amplitude, A, phase shift, C, and β is the anisotropy parameter.

$$\boldsymbol{I(\theta) = \frac{A}{4\pi}[1 + \beta P_2(cos(\theta - C))]}$$

$$\boldsymbol{P_2(\cos(\theta - C)) = \frac{1}{2}[3cos^2(\theta - C) - 1]}$$

A = 7.40245

β = 0.38378

C = 0.03814

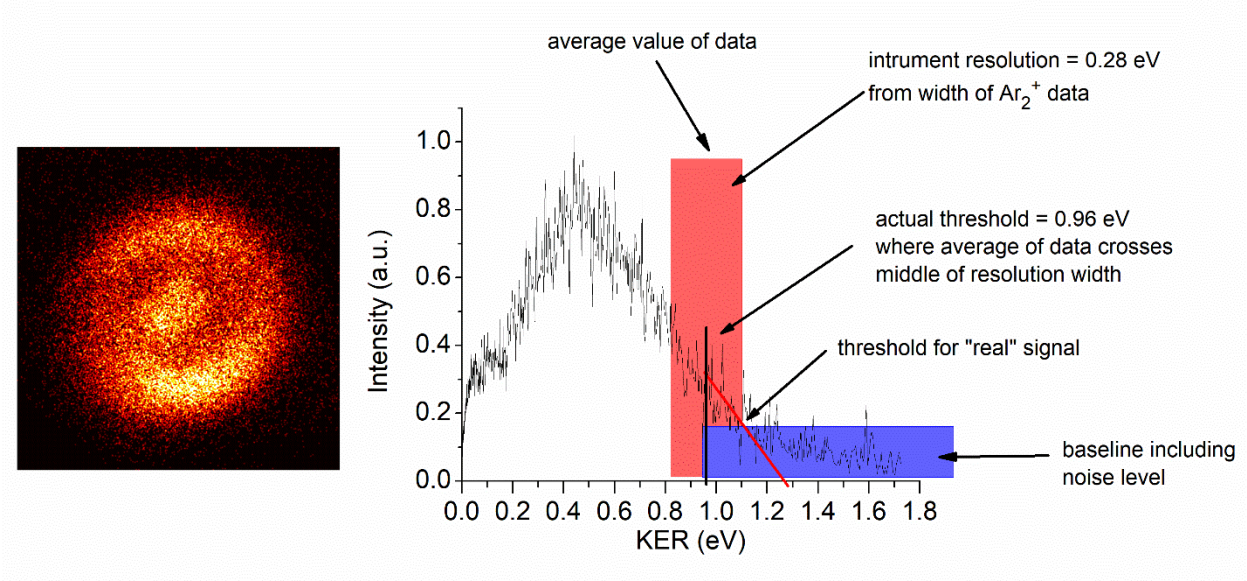

Figure A3: Kinetic energy release (KER) and image of benzene$^+$ from Ag^+(benzene) for photodissociation at 280 nm. The KER graph includes details of how the threshold for maximum kinetic energy release was determined.

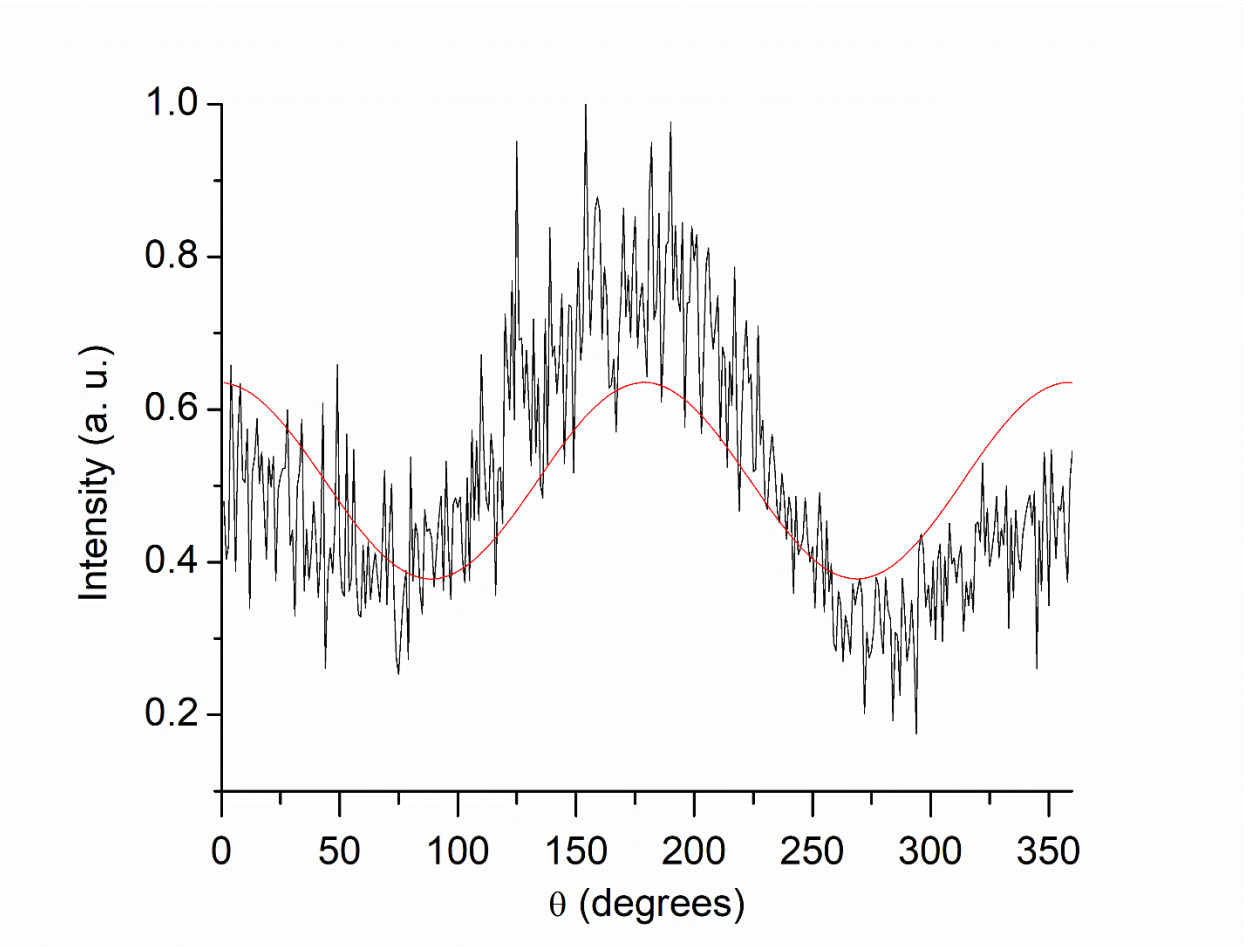

Figure A4: Angular distribution for the image of benzene cation from photodissociation of Ag^+(benzene) at 280 nm. The data was fitted with the below function with amplitude, A, phase shift, C, and β is the anisotropy parameter.

$$\boldsymbol{I(\theta) = \frac{A}{4\pi}[1 + \beta P_2(cos(\theta - C))]}$$

$$P_2(\cos(\boldsymbol{\theta - C})) = \boldsymbol{\frac{1}{2}[3cos^2(\theta - C) - 1]}$$

A = 5.82751

β = 0.37037

C = -0.02172

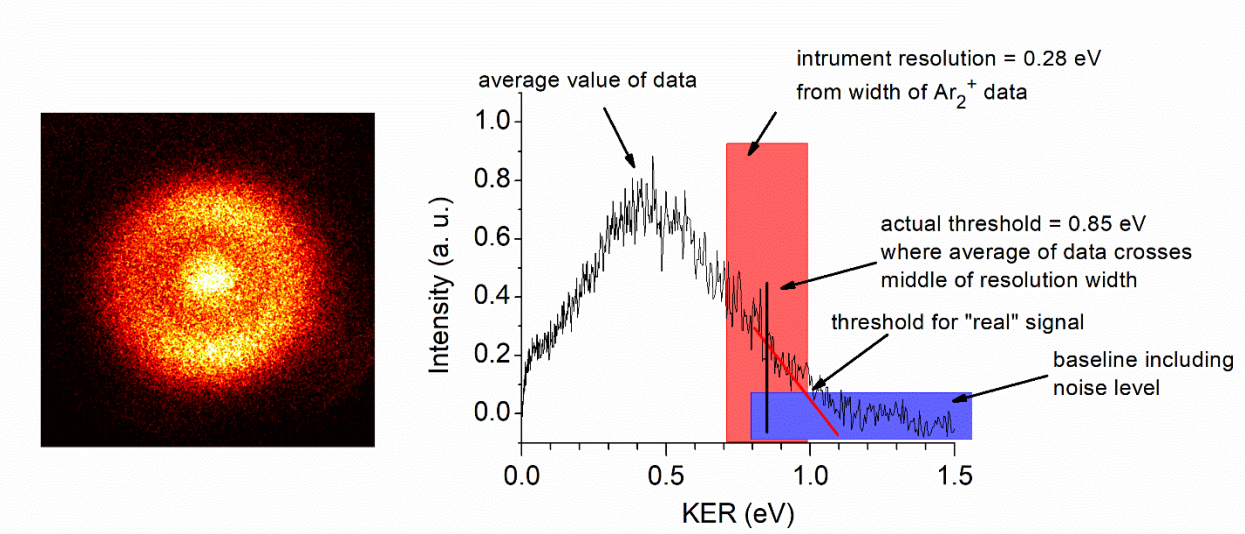

Figure A5: Kinetic energy release (KER) and image of benzene$^+$ from Ag^+(benzene) for photodissociation at 266 nm. The KER graph includes details of how the threshold for maximum kinetic energy release was determined.

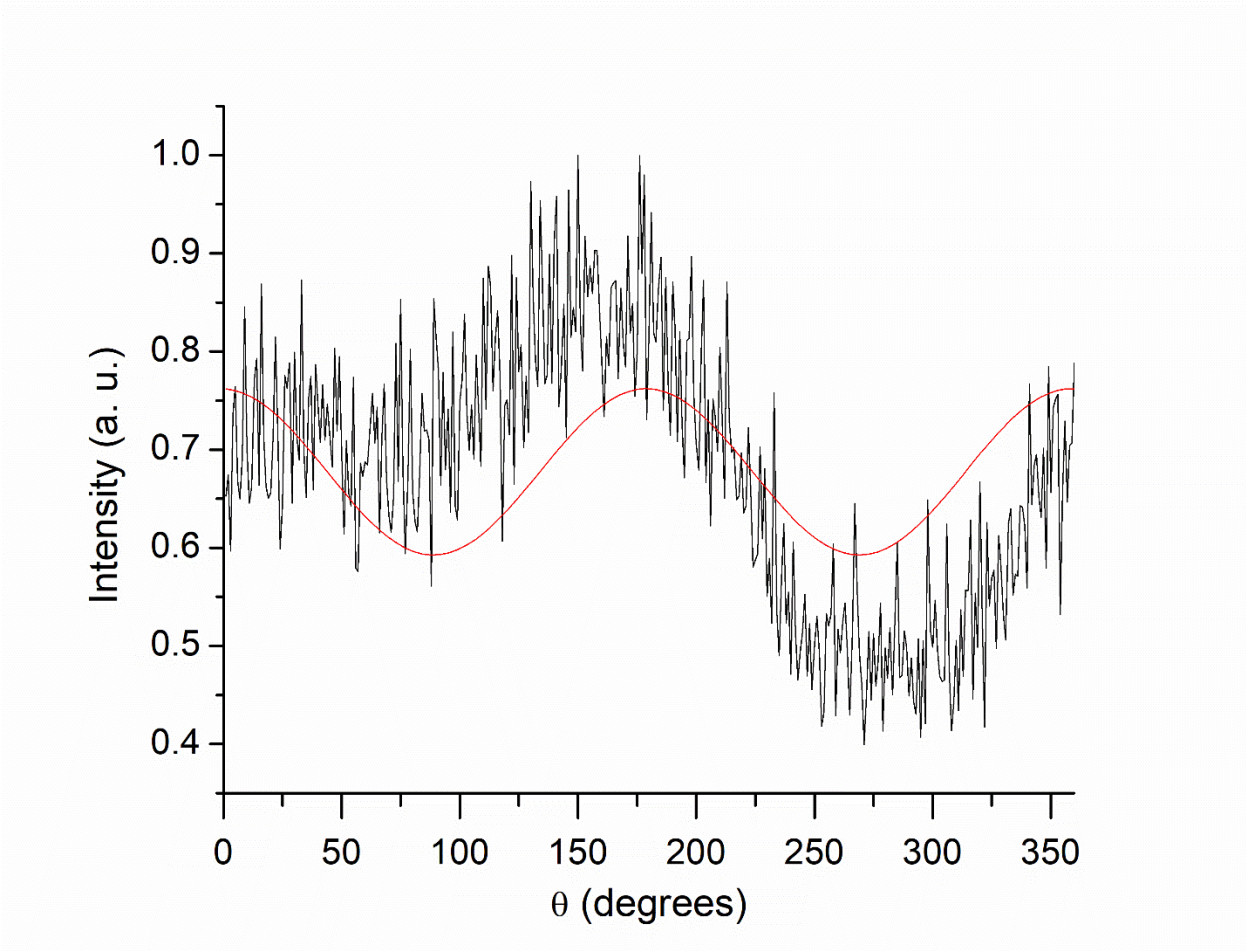

Figure A6: Angular distribution for the image of benzene cation from photodissociation of Ag^+(benzene) at 266 nm. The data was fitted with the below function with amplitude, A, phase shift, C, and β is the anisotropy parameter.

$$\boldsymbol{I(\theta) = \frac{A}{4\pi}[1 + \beta P_2(cos(\theta - C))]}$$

$$P_2(\cos(\boldsymbol{\theta - C})) = \boldsymbol{\frac{1}{2}[3cos^2(\theta - C) - 1]}$$

A = 8.1573

β = 0.17404

C = -0.01934

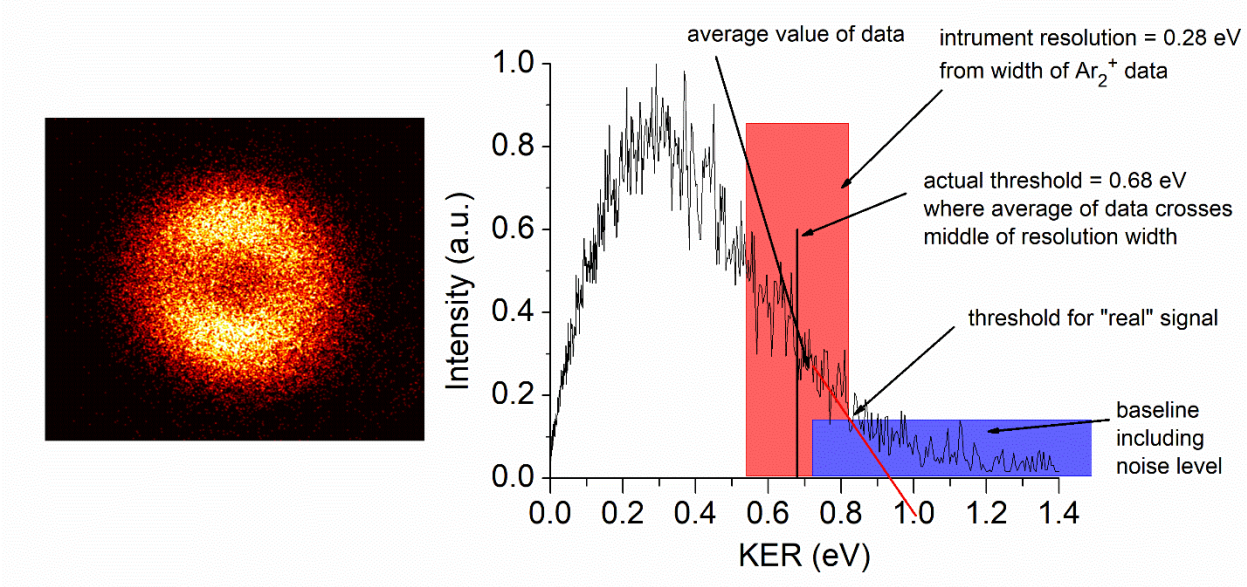

Figure A7: Kinetic energy release (KER) and image of toluene$^+$ from Ag$^+$(toluene) for photodissociation at 355 nm. The KER graph includes details of how the threshold for maximum kinetic energy release was determined.

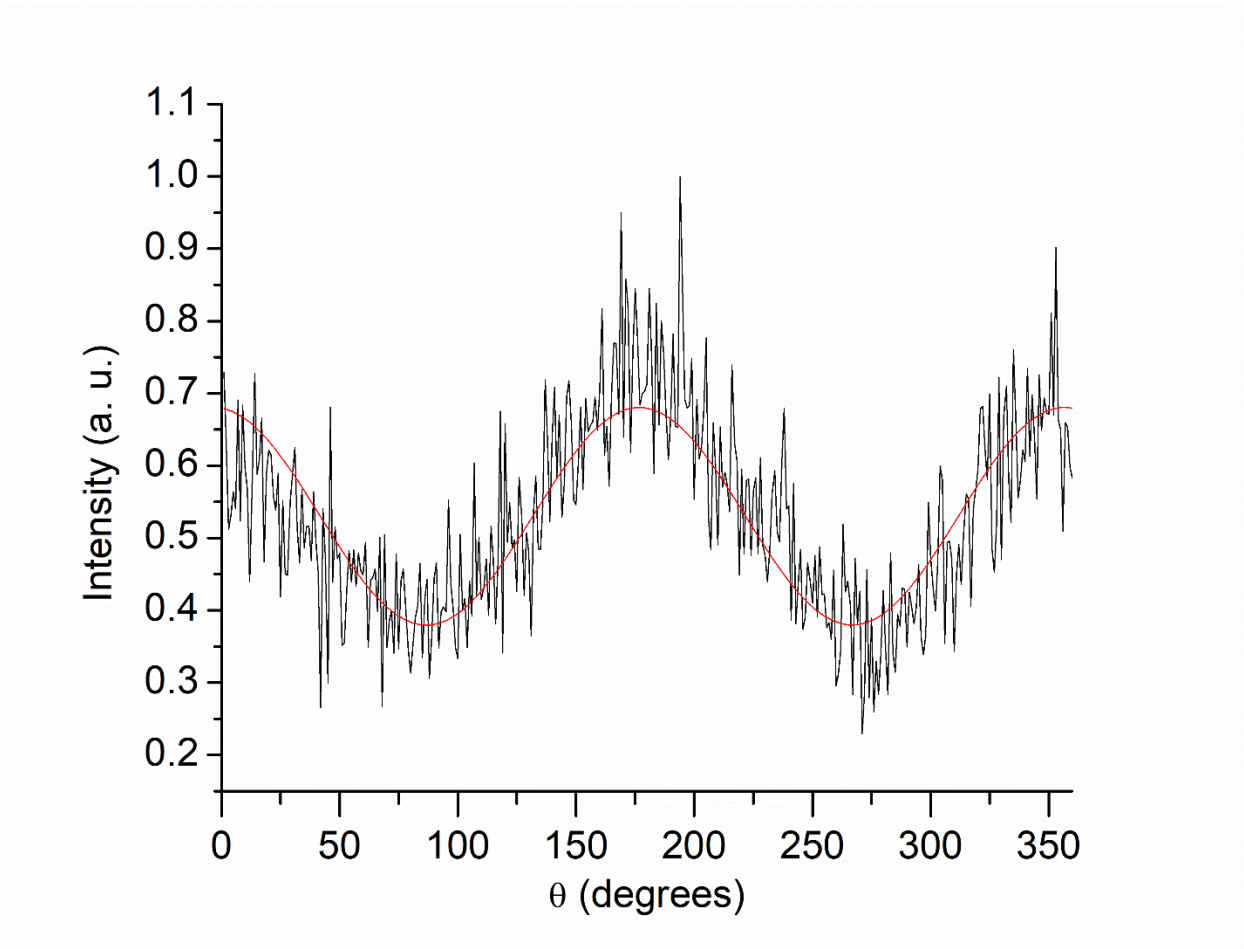

Figure A8: Angular distribution for the image of toluene cation from photodissociation of Ag^+(toluene) at 355 nm. The data was fitted with the below function with amplitude, A, phase shift, C, and β is the anisotropy parameter.

$$\boldsymbol{I(\theta) = \frac{A}{4\pi}[1 + \beta P_2(cos(\theta - C))]}$$

$$P_2(\cos(\boldsymbol{\theta - C})) = \boldsymbol{\frac{1}{2}[3cos^2(\theta - C) - 1]}$$

A = 6.03118

β = 0.41838

C = -0.05694

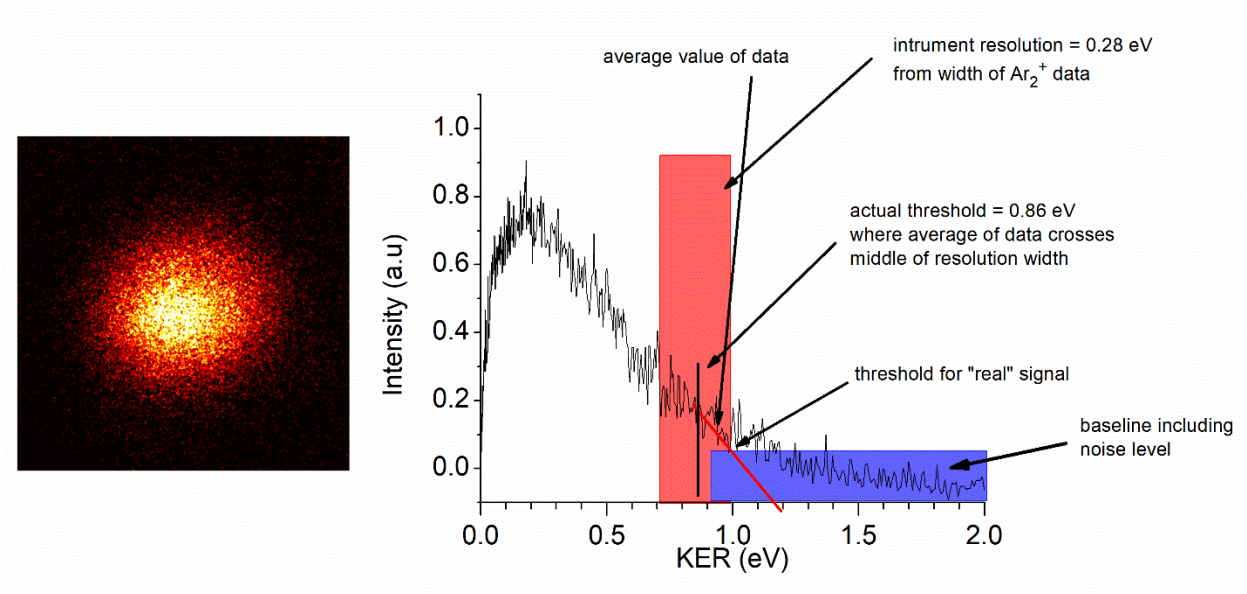

Figures A9**:** Kinetic energy release (KER) and image of toluene$^+$ from Ag^+(toluene) for photodissociation at 266 nm. The KER graph includes details of how the threshold for maximum kinetic energy release was determined.

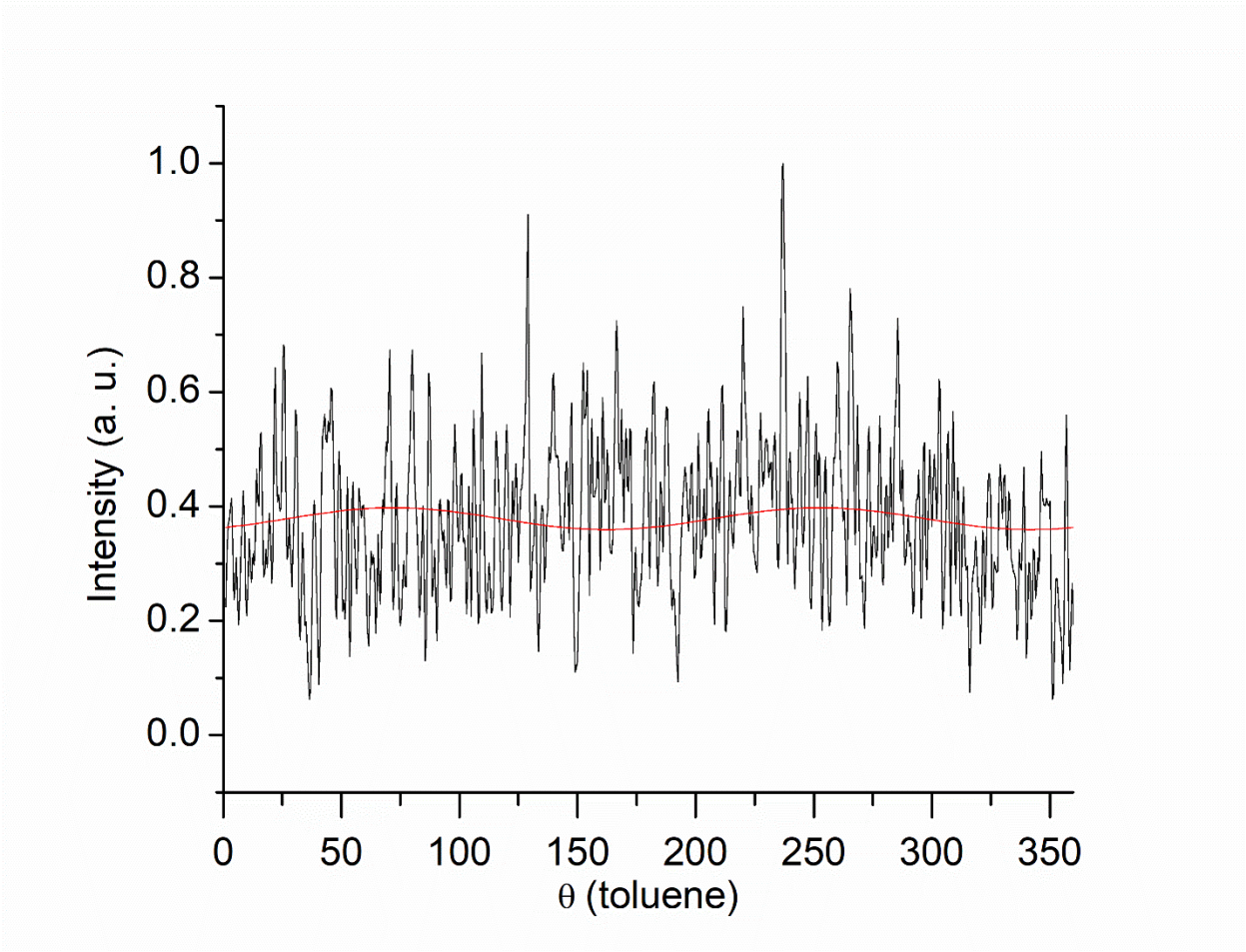

Figure A10: Angular distribution for the image of toluene cation from photodissociation of Ag^+(toluene) at 266 nm. The data was fitted with the below function with amplitude, A, phase shift, C, and β is the anisotropy parameter.

$$\boldsymbol{I(\theta) = \frac{A}{4\pi}[1 + \beta P_2(cos(\theta - C))]}$$

$$P_2(\cos(\boldsymbol{\theta - C})) = \boldsymbol{\frac{1}{2}[3cos^2(\theta - C) - 1]}$$

A = 4.67591

β = 0.06849

C = 1.26035

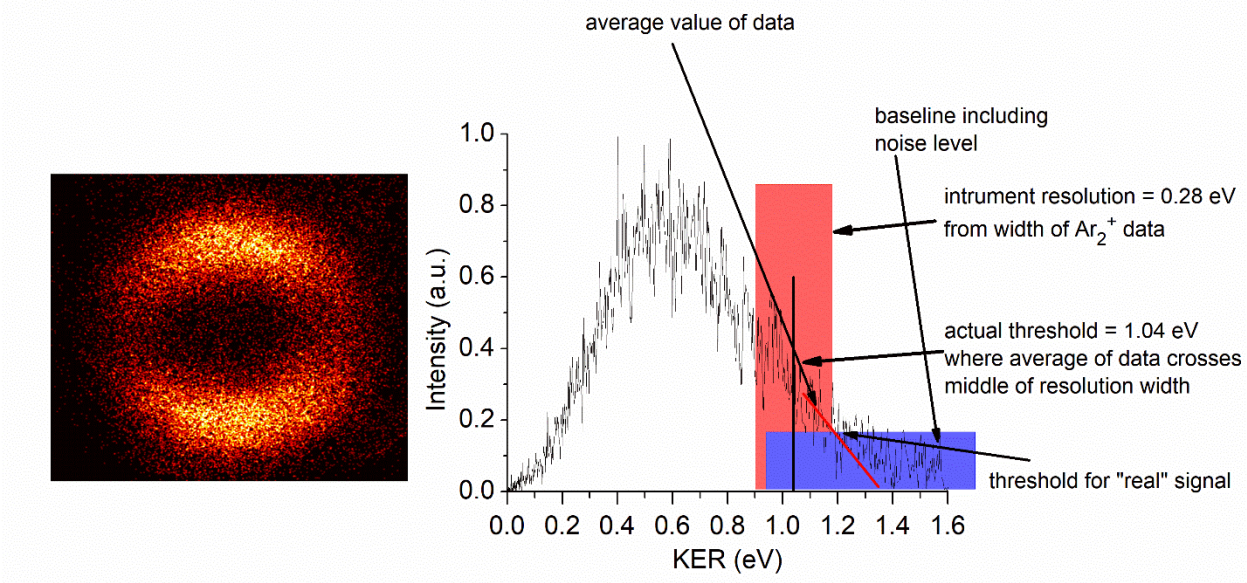

Figure A11: Kinetic energy release (KER) and image of furan$^+$ from Ag$^+$(furan) for photodissociation at 355 nm. The KER graph includes details of how the threshold for maximum kinetic energy release was determined.

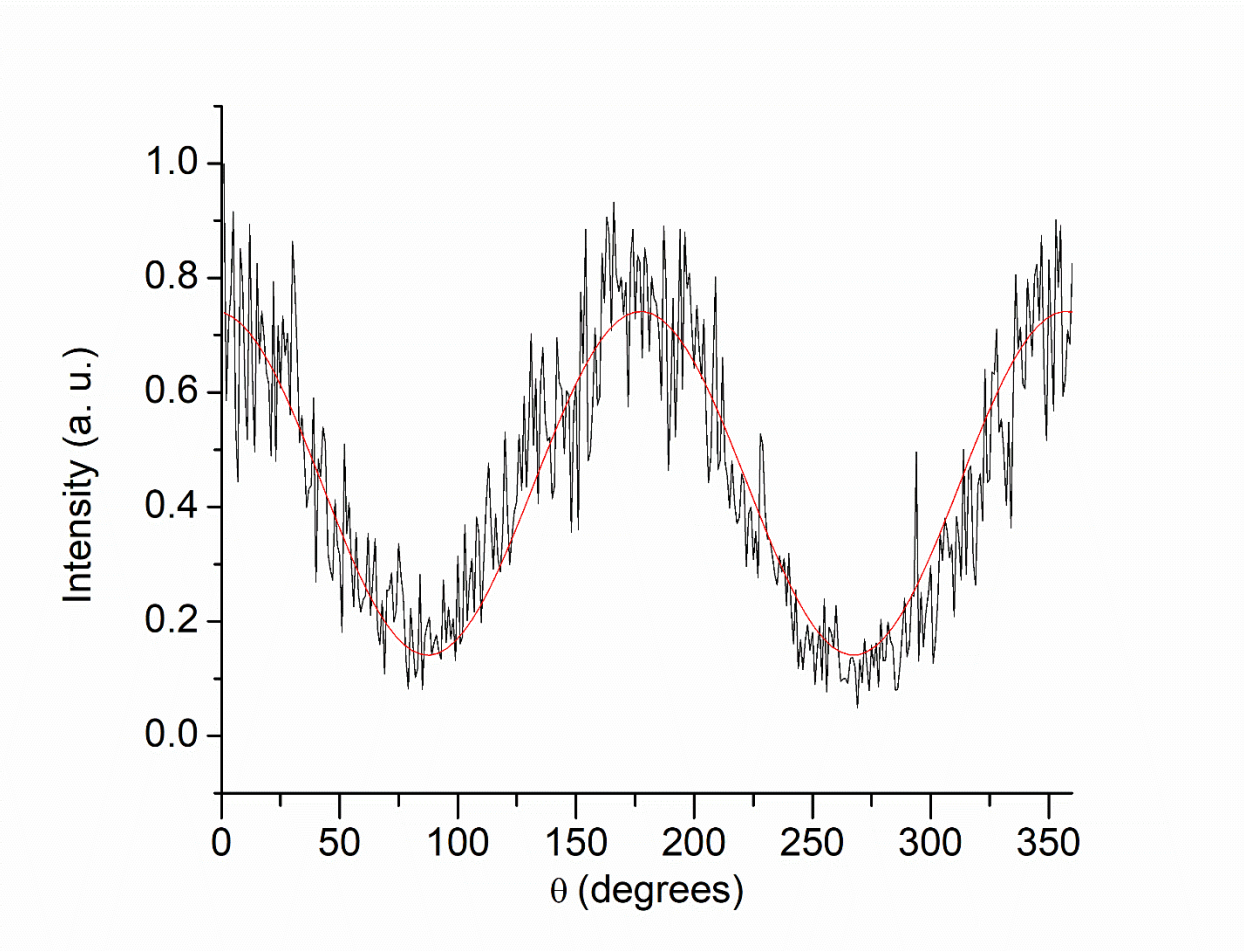

Figure A12: Angular distribution for the image of furan cation from photodissociation of Ag^+(furan) at 355 nm. The data was fitted with the below function with amplitude, A, phase shift, C, and β is the anisotropy parameter.

$$\boldsymbol{I(\theta) = \frac{A}{4\pi}[1 + \beta P_2(cos(\theta - C))]}$$

$$P_2(\cos(\boldsymbol{\theta - C})) = \boldsymbol{\frac{1}{2}[3cos^2(\theta - C) - 1]}$$

A = 4.28696

β = 1.17361

C = 3.09547

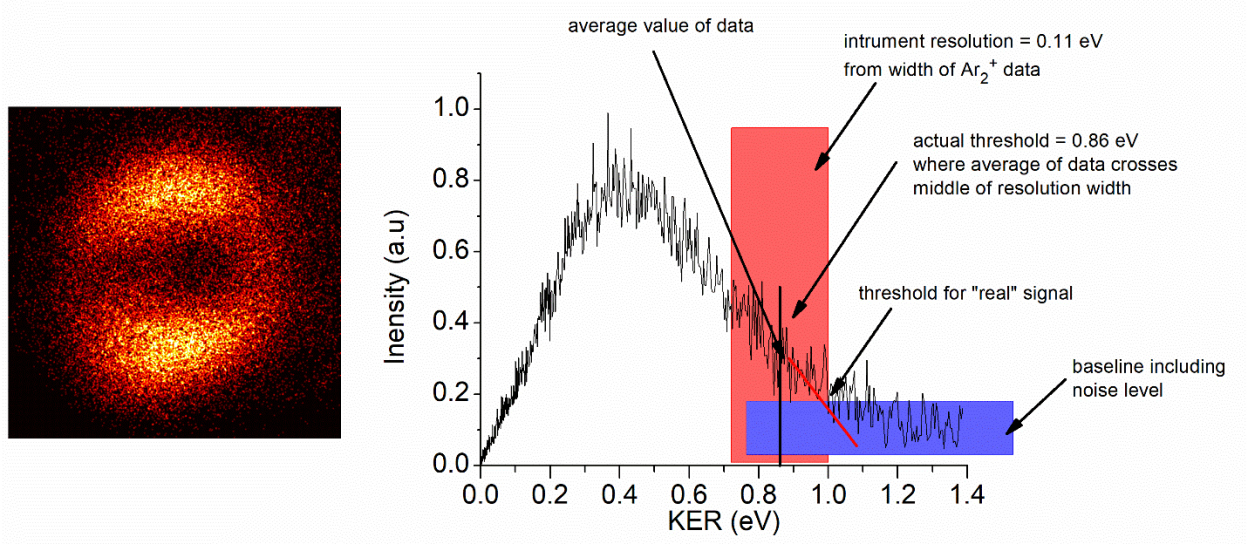

Figure A13: Kinetic energy release (KER) and image of furan$^+$ from Ag$^+$(furan) for photodissociation at 266 nm. The KER graph includes details of how the threshold for maximum kinetic energy release was determined.

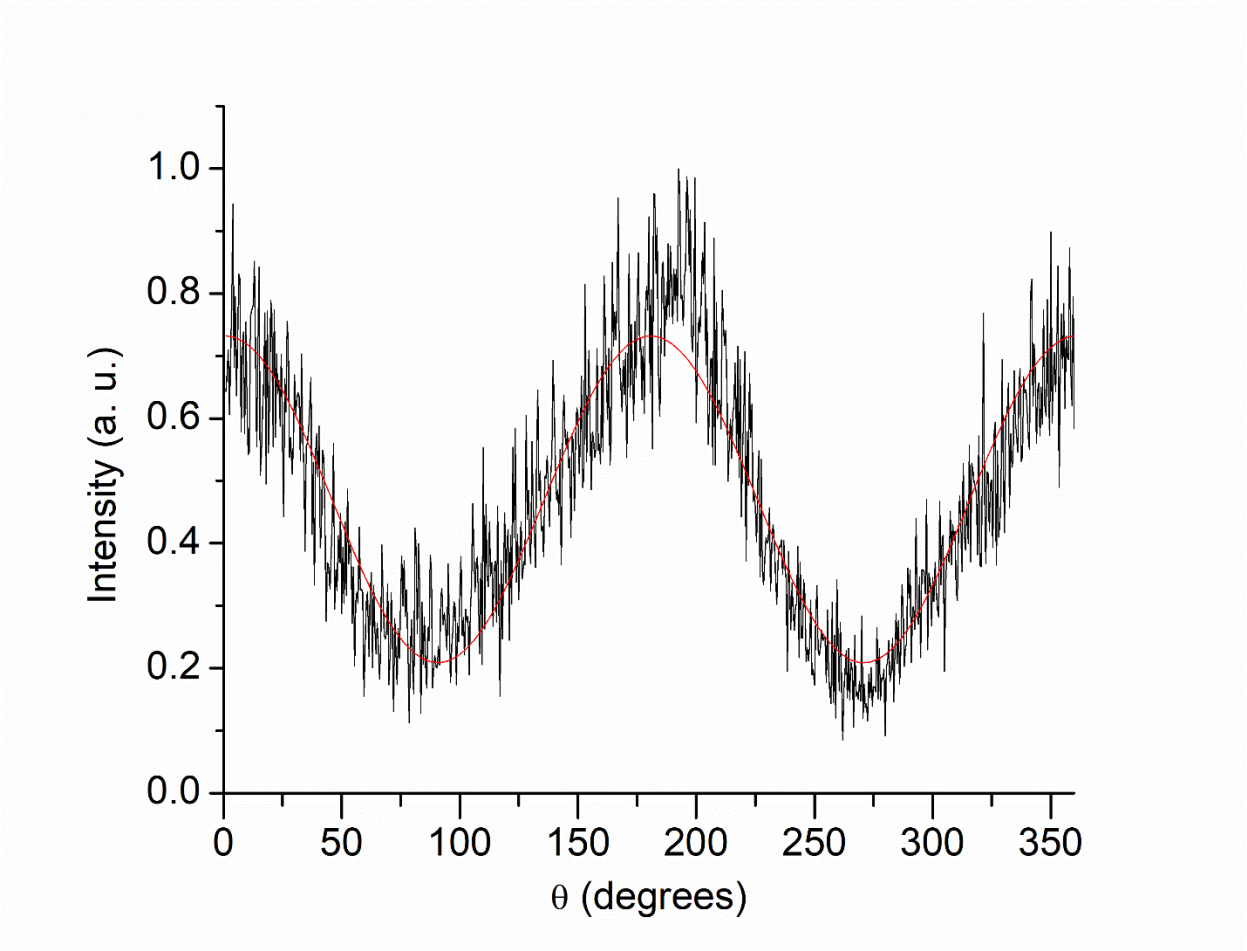

Figure A14: Angular distribution for the image of furan cation from photodissociation of Ag^+(furan) at 266 nm. The data was fitted with the below function with amplitude, A, phase shift, C, and β is the anisotropy parameter.

$$\boldsymbol{I(\theta) = \frac{A}{4\pi}[1 + \beta P_2(cos(\theta - C))]}$$

$$P_2(\cos(\boldsymbol{\theta - C})) = \boldsymbol{\frac{1}{2}[3cos^2(\theta - C) - 1]}$$

A = 4.81479

β = 0.91095

C = 0.01413

APPENDIX B

COMPUTATIONAL CHEMISTRY AND IMAGE ANALYSIS

OF THE $Zn^{+}(CH_3OH)$ COMPLEX

$Zn^{+}(CH_3OH)$ Optimized Geometries

B3LYP/Def2-TZVP

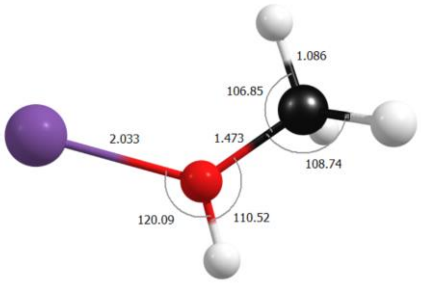

Coordinates:

C	2.327826000	-0.605042000	0.000000000
H	1.882595000	-1.595196000	0.000000000
H	2.919419000	-0.457479000	-0.899916000
H	2.919419000	-0.457479000	0.899916000
O	1.217051000	0.362570000	0.000000000
H	1.556732000	1.268988000	0.000000000
Zn	-0.787441000	0.025317000	0.000000000

B3LYP/Def2-QZVP

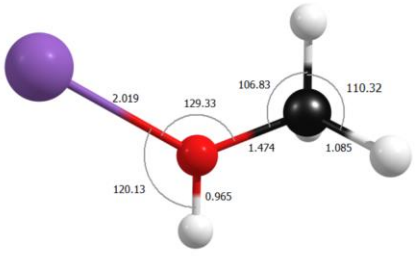

Coordinates:

C	2.326377000	-0.604933000	0.000000000
H	1.881644000	-1.593639000	0.000000000
H	2.917298000	-0.457455000	-0.898239000
H	2.917298000	-0.457455000	0.898239000
O	1.214952000	0.362782000	0.000000000
H	1.553258000	1.266933000	0.000000000
Zn	-0.775227000	0.025447000	0.000000000

M06-L/Def2-TZVP

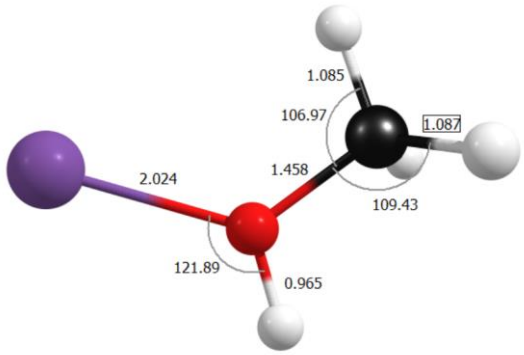

Coordinates:

C	2.314838000	-0.593922000	0.000000000
H	1.863801000	-1.580724000	0.000000000
H	2.913831000	-0.462945000	-0.897059000
H	2.913831000	-0.462945000	0.897059000
O	1.223151000	0.373080000	0.000000000
H	1.571455000	1.273103000	0.000000000
Zn	-0.765307000	-0.003968000	0.000000000

M06-L/Def2-QZVP

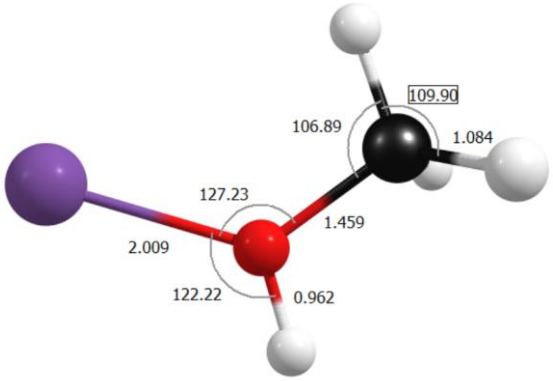

Coordinates:

C	2.312986000	-0.594050000	0.000000000
H	1.858553000	-1.577656000	0.000000000
H	2.909695000	-0.463251000	-0.895691000
H	2.909695000	-0.463251000	0.895691000
O	1.223199000	0.376462000	0.000000000
H	1.569862000	1.273352000	0.000000000
Zn	-0.748391000	-0.009926000	0.000000000

MN15-L/Def2-TZVP

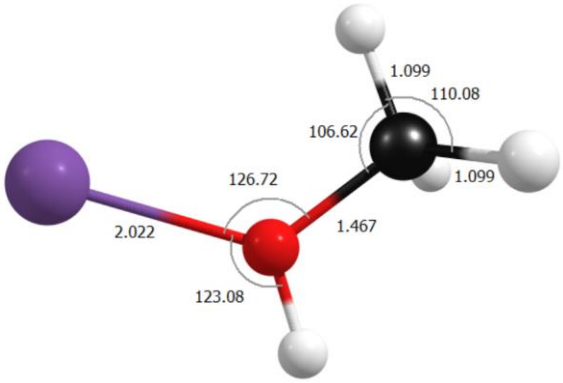

Coordinates:

C	2.314455000	-0.594895000	0.000000000
H	1.846891000	-1.588961000	0.000000000
H	2.917274000	-0.461467000	-0.909035000
H	2.917274000	-0.461467000	0.909035000
O	1.221270000	0.382846000	0.000000000
H	1.578651000	1.284884000	0.000000000
Zn	-0.760214000	-0.019260000	0.000000000

MN15-L/Def2-QZVP

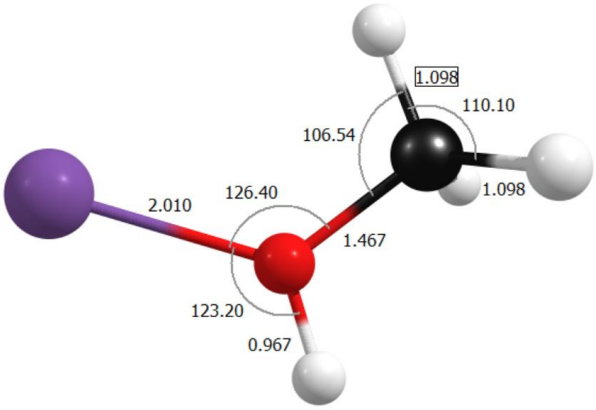

Coordinates:

C	2.313047000	-0.594454000	0.000000000
H	1.842832000	-1.586836000	0.000000000
H	2.915263000	-0.462251000	-0.908389000
H	2.915263000	-0.462251000	0.908389000
O	1.220894000	0.385157000	0.000000000
H	1.575210000	1.285039000	0.000000000
Zn	-0.746910000	-0.022724000	0.000000000

Optimized Geometries of $CH_3-Zn-OH^+$

B3LYP/Def2-TZVP

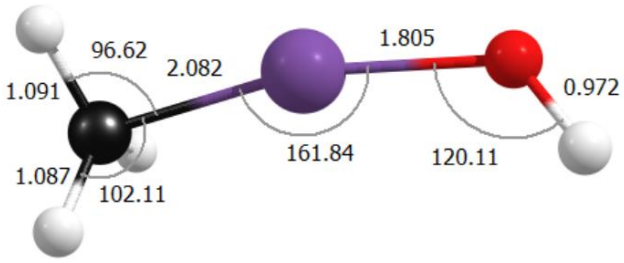

Coordinates:

Zn	-1.485774000	-1.027824000	0.542618000
C	-1.567314000	-0.313868000	-1.411104000
H	-1.447397000	-1.280506000	-1.903462000
H	-2.552763000	0.140698000	-1.458072000
H	-0.717314000	0.362627000	-1.442372000
O	-1.739704000	-1.186673000	2.322903000
H	-1.318063000	-0.559175000	2.933338000

B3LYP/Def2-QZVP

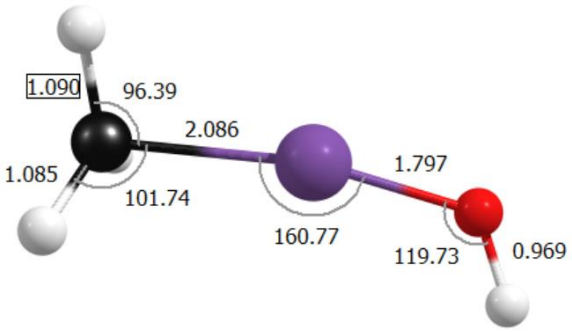

Coordinates:

Zn	-1.452922000	-1.036918000	0.544695000
C	-1.568688000	-0.312969000	-1.408687000
H	-1.461858000	-1.278714000	-1.902406000
H	-2.551290000	0.145317000	-1.435720000
H	-0.716243000	0.357823000	-1.446402000
O	-1.726122000	-1.197852000	2.313334000
H	-1.351206000	-0.541408000	2.919036000

M06-L/Def2-TZVP

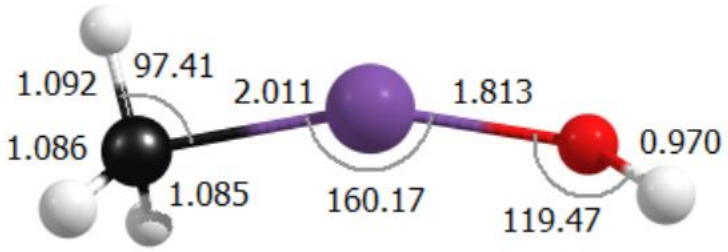

Coordinates:

Zn	-1.532591000	-1.015921000	0.518095000
C	-1.563035000	-0.324105000	-1.369957000
H	-1.386435000	-1.277481000	-1.872155000
H	-2.557038000	0.094864000	-1.491304000
H	-0.746556000	0.389867000	-1.414969000
O	-1.816955000	-1.105537000	2.306121000
H	-1.225718000	-0.626407000	2.908018000

M06-L/Def2-QZVP

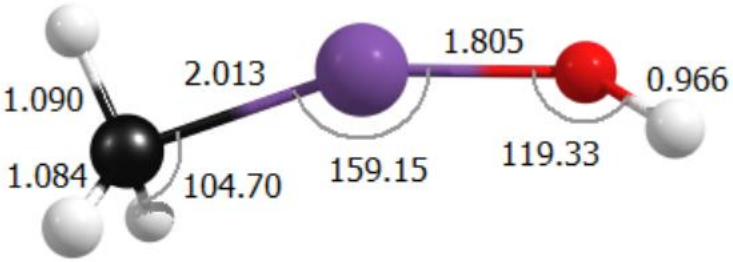

Coordinates:

Zn	-1.464776000	-1.023760000	0.517060000
C	-1.569056000	-0.325910000	-1.368361000
H	-1.360182000	-1.269394000	-1.871804000
H	-2.580493000	0.048265000	-1.467388000
H	-0.784836000	0.420590000	-1.412659000
O	-1.777378000	-1.144525000	2.290284000
H	-1.291607000	-0.569987000	2.896717000

MN15-L/Def2-TZVP

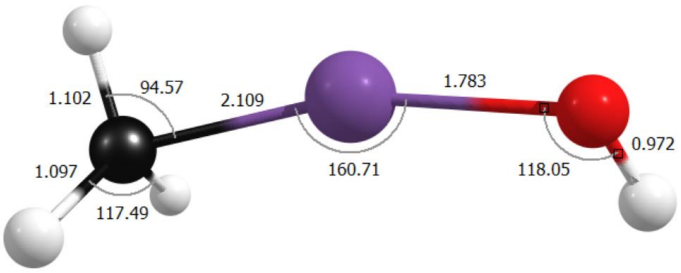

Coordinates:

Zn	-1.589357000	-1.039657000	0.558096000
C	-1.561417000	-0.311335000	-1.420984000
H	-1.583906000	-1.311841000	-1.883015000
H	-2.487549000	0.277448000	-1.434412000
H	-0.612263000	0.237545000	-1.445022000
O	-1.272129000	-1.170660000	2.307503000
H	-1.721708000	-0.546220000	2.901682000

MN15-L/Def2QZVP

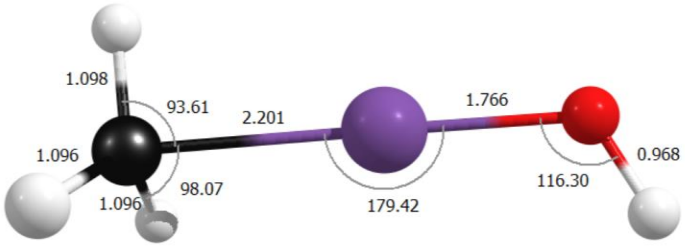

Coordinates:

Zn	-1.542366000	-0.865503000	0.630156000
C	-1.553549000	-0.302422000	-1.497547000
H	-1.551789000	-1.344069000	-1.844810000
H	-2.497824000	0.252991000	-1.504633000
H	-0.612852000	0.258888000	-1.512640000
O	-1.533082000	-1.300024000	2.342132000
H	-1.536867000	-0.564582000	2.971191000

Kinetic Energy Release Analysis

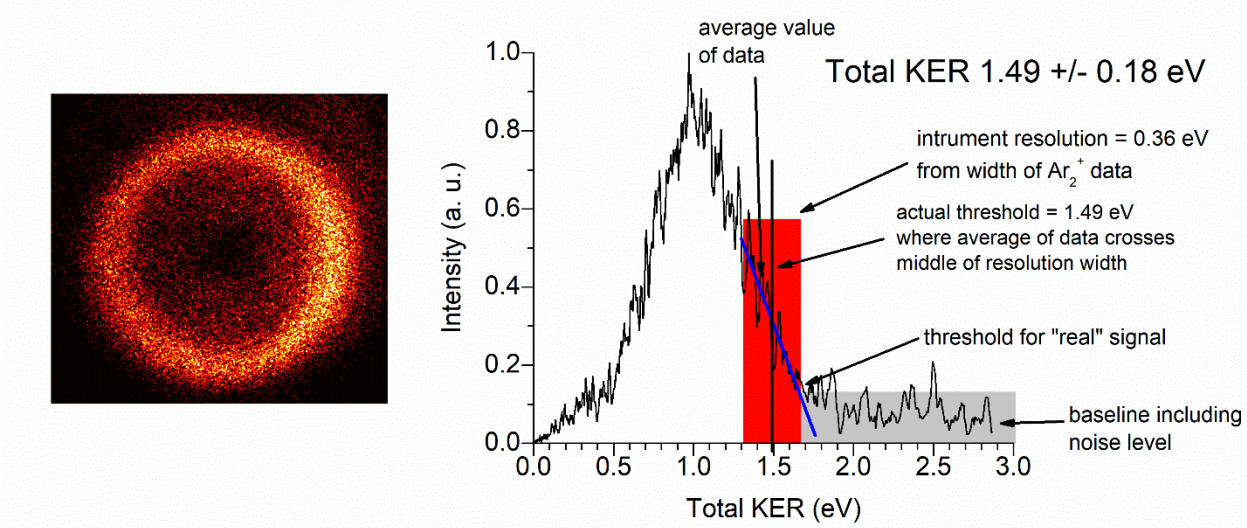

Figure B1: Raw image and kinetic energy release (KER) spectrum of CH_3OH^+ from dissociation of $Zn^+(CH_3OH)$ at 266 nm. The spectrum includes details on how the threshold for maximum kinetic energy release was determined. The gray box includes a section of baseline that illustrates the level of noise in our experiment outside the boundaries of the image. The red box indicates the width of the KER signal measured from dissociation of Ar_2^+ at 355 nm under the same experimental conditions. This is judged to be the instrument resolution. We set the high-energy edge of the resolution at the point where the signal rises above the baseline. We draw a line through the signal as it approaches the baseline, and select the point where this crosses the mid-point of the resolution width. This is defined as the high-energy edge of the image, and is used to define the maximum KER value in the image.

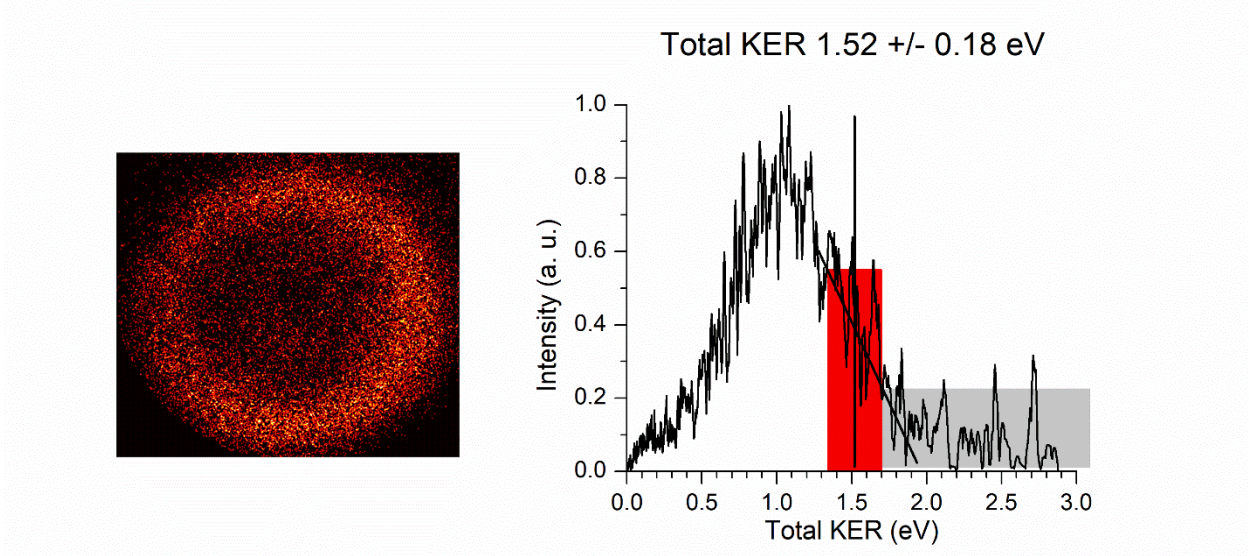

Figure B2: Raw image and kinetic energy release (KER) spectrum of CH_3OH^+ from dissociation of $Zn^+(CH_3OH)$ at 280 nm. KER spectrum includes the details of determining the maximum kinetic energy as described above.

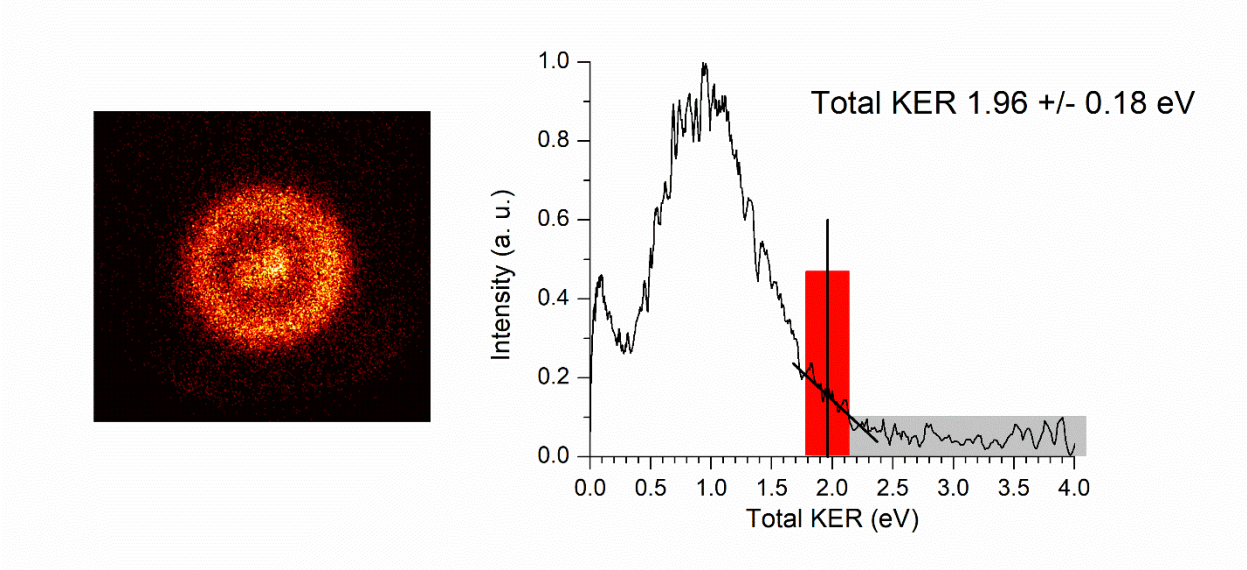

Figure B3: Raw image and kinetic energy release (KER) spectrum of Zn^+ from dissociation of $Zn^+(CH_3OH)$ at 266 nm. KER spectrum includes the details of determining the maximum kinetic energy as described above.

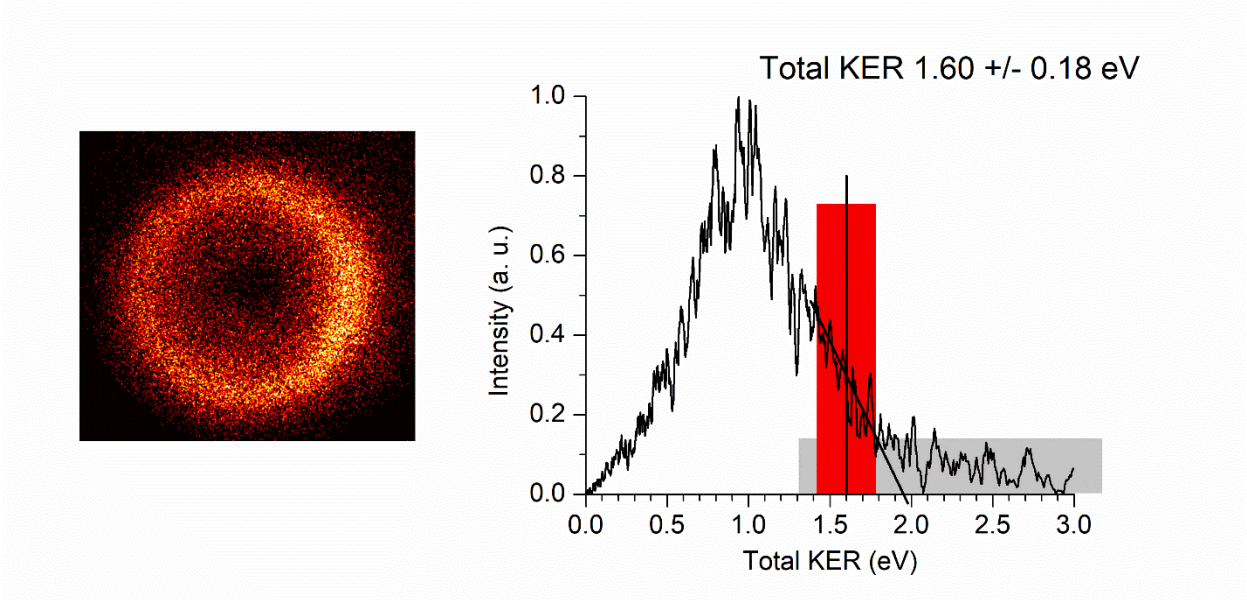

Figure B4: Raw image and kinetic energy release (KER) spectrum of CD_3OD^+ from dissociation of $Zn^+(CD_3OD)$ at 266 nm. KER spectrum includes the details of determining the maximum kinetic energy as described above.

APPENDIX C

RESULTS OF USING DIFFERENT EXPANSION GASES FOR THE COOLING OF CARBON CLUSTERS

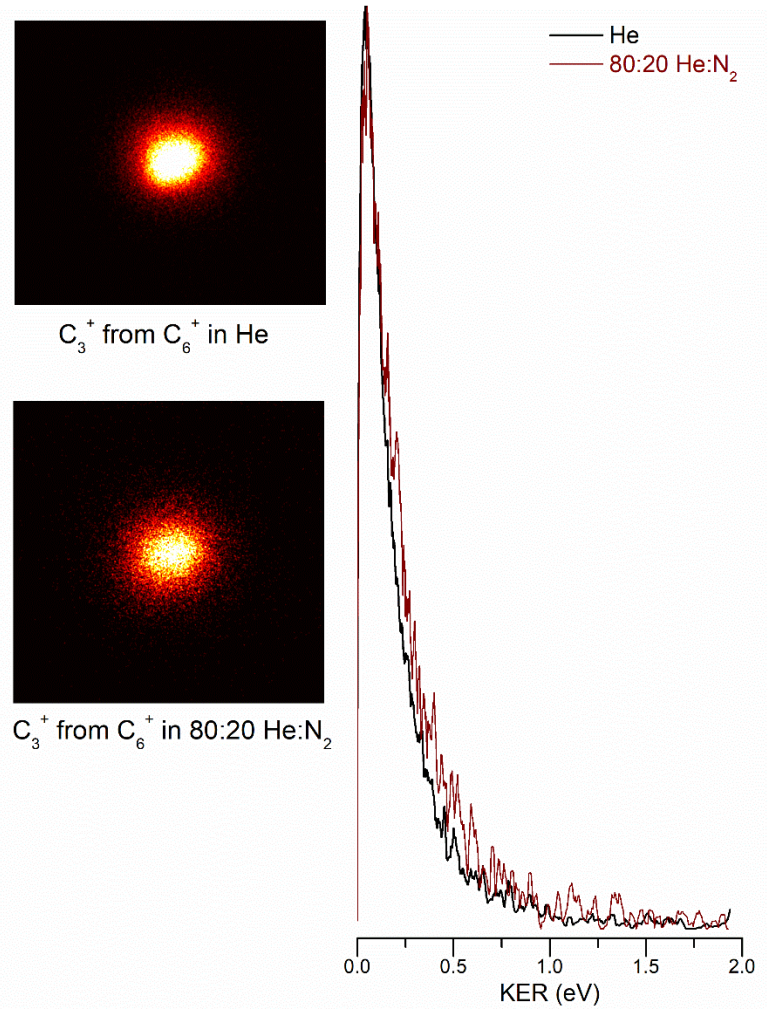

Figure C1. KER profiles for the dissociation of C_6^+ at 355 nm using different types of expansion gases.